Department of AERONAUTICS and ASTRONAUTICS
STANFORD UNIVERSITY

A. J. MULAC

EXPERIMENTAL AND THEORETICAL INVESTIGATION OF SHOCK–TUBE PRECURSORS

Supported by the
National Aeronautics and Space Administration
Grant NGR 05-020-245

SEPTEMBER
1968

SUDAAR
NO. 358

DEPARTMENT OF AERONAUTICS AND ASTRONAUTICS

STANFORD UNIVERSITY
STANFORD, CALIFORNIA

EXPERIMENTAL AND THEORETICAL INVESTIGATION OF SHOCK-TUBE PRECURSORS

by

A. J. Mulac

SUDAAR No. 358

September 1968

This research was sponsored by the National Aeronautics and Space Administration under Research Grant NGR 05-020-245

ABSTRACT

Electrical precursor phenomena under a broad spectrum of conditions have been studied with a potential probe suspended in a metal shock tube. These data were supplemented with qualitative biased probe measurements. Strong negative signals were observed with the potential probe from one to two shock-tube diameters ahead of argon shocks (M_s = 6.5 to 16, p_1 = 2.5 to 10 Torr) and nitrogen shocks (M_s = 10.5 to 15, p_1 = 5 Torr). Photoemitted electrons from the shock tube and probe surfaces were observed far ahead (meters) of both argon and nitrogen shock waves. Photoionization of the test gas and/or impurity gases was detected ahead of very strong ($M_s > 14$) shocks in argon. The shock heated test gas, as opposed to the combustion driver gases, was determined to be the radiation source for the above radiative phenomena. No precursors were observed in helium for $M_s \leq 9.2$ and p_1 = 5 Torr. A theoretical model was formulated to explain the low Mach number (6.5 to 9.0) argon experimental results. The model couples very small scale electron diffusion at the translational shock front with simple, but three dimensional, electrostatics. This model predicts the observed precursor-potential profile in terms of a dipole type structure at the translational shock front.

ACKNOWLEDGMENTS

The author wishes to express his appreciation to Professor Donald Baganoff for his guidance in this research.

The comments of Professors Daniel Bershader and I-Dee Chang who read the text are also appreciated.

Personal gratitude is extended to his wife Beth for patience and encouragement during this trying period. Thanks are also due for her typing of the rough drafts of this manuscript.

The author is indebted to the Ford Foundation for financial support provided through a Ford Foundation Plasma Fellowship. The work presented here was supported by the National Aeronautics and Space Administration under Research Grant NASA NGR 05-020-245.

TABLE OF CONTENTS

APPENDICES PAGE

LIST OF ILLUSTRATIONS

FIGURE PAGE

FIGURE		PAGE

NOMENCLATURE

a	effective shock tube radius
A	non-dimensional drag parameter
B	non-dimensional electrostatic parameter
D	drag per electron charge
e	magnitude of electron charge
h	Debye length
$h(\lvert x-\xi \rvert)$	disk potential solution
J_0, J_1	Bessel function of the first kind
k	Boltzmann's constant
$k(x,\xi)$	kernel function
ℓ	ionization relaxation length
M	Mach number
m	particle mass
n	particle number density
p	gas pressure
R	resistance
T	gas temperature
u	gas speed
V	voltage
x	axial distance
α	degree of ionization

δ	charge separation
ϵ_0	permittivity of vacuum
$\bar{\nu}$	average collision frequency
ξ	axial distance
σ	charge per area
φ	electrostatic potential
φ_0	dipole strength

SUBSCRIPTS

1	initial driven section condition
4L	combustion driver load
dp	dipole
e	electron
ℓ,m,n	indices of summation
s	shock wave

1. INTRODUCTION

Electrical effects which precede strong shock waves are called precursors, and are of particular interest here. We are concerned with shock-wave precursors in conventional shock tubes, i.e., we exclude phenomena associated with electro-magnetically driven and high-energy, solid-explosive-driven facilities. Electrical precursors have received much attention by both experimentalists and theoreticians since 1957. For those readers who are not familiar with shock-tube precursor phenomena, a comprehensive review of the experimental and theoretical work reported previously is given in Appendix A. The results of work presented to date are somewhat confusing. One reason for this state of affairs is the limited range of parameters considered and the qualitative nature of most of the experimental data. The second reason is the very complicated nature of precursors; this is evidenced by the fact that significant, but fragmentary experimental data has been reported that suggests more than one mechanism may play a role in shock-tube precursor phenomena. Results from argon and xenon experiments have been reported which suggest electron diffusion, photoemission from the shock tube surface, and photoionization of both test gas and impurity gases are all involved in the shock-tube precursor problem.

Besides the fact that precursor phenomena are intrinsically interesting to investigate, there are at least two very practical reasons to study precursors. The first deals with shock-tube instrumentation. Precursor effects usually manifest themselves as spurious noise signals from the instrumentation in use; examples include piezoelectric gauges,[22] thin-film heat gauges,[23] and capacitance element sensors.[24,25] A better understanding of the nature of precursors would be a valuable aid in designing shock tube instrumentation. The second reason for trying to learn about precursors is to evaluate their influence on other shock-tube experimental results. An example case would be the shock-tube investigation of ionization relaxation in pure gases. Indeed, a thorough understanding of precursor phenomena may be a direct aid to constructing kinetic models for such relaxation phenomena. Any of the above comments justifies further investigation of precursors.

Our experimental objective in the work presented here is to obtain a broader view of shock-tube precursor phenomena. Chapter 2 of this report discusses an extensive series of experiments which were performed with the above objective in mind. Parameters which were varied in these experiments include the test gas, initial pressure, Mach number, length of the shock tube, and the driver technique. Quantitative potential measurements were made with a wire-mesh electrode suspended in the shock tube. These measurements were supplemented with qualitative biased probe data taken during the same experiments. The latter data served to aid in the interpretation of the potential measurements.

Our experimental data varifies that electron diffusion, photoemission from the shock tube surfaces, and photoionization of the test gas or impurity gases all play some role in precursor phenomena in argon and nitrogen experiments. We observed no precursor phenomena in helium experiments for $p_1 = 5$ Torr and $M_s \leq 9.2$.

Our low Mach-number (6.5 to 9) argon experiments indicated that small scale electron diffusion is responsible for a charge double layer in the vicinity of the shock wave. In this Mach number range there is no plasma arising from photoionization ahead of the shock wave. Chapter 3 is devoted to a theoretical model of the charge double layer. This model is solved and compared with the experimental data. The experimental potential profile ahead of the shock wave is not sufficient to determine all the unknown quantities in the theoretical model. However, a physically reasonable range of parameters is shown to give good agreement between theory and experiment.

Chapter 4 of this report consists of concluding remarks. The low Mach-number precursor study is summarized in the first section. A section of observations and conjectures on higher Mach-number precursors is included. The final section presents the writer's perspective on the shock-tube precursor problem.

2. PRECURSOR EXPERIMENTS

A number of shock-tube precursor experiments have been carried out in the Stanford Aerophysics Laboratory. Appendix B contains a description of the shock tube and pertinent performance data obtained simultaneously with the experiments. Appendix B also discusses the measurements of initial driven-section pressure and incident-shock Mach number.

In the following paragraphs we present the experimental techniques employed and the information obtained about precursor phenomena in the shock tube.

2.1. Experimental Objectives and Technique.

As stated in the introductory chapter, earlier experiments on shock-tube precursor phenomena have been limited in scope and often qualitative in nature. Our experimental objective in the current work is to obtain a broader picture of the precursor phenomena. Clearly we must investigate a wide range of incident shock Mach numbers, a variation in the initial pressure of the test gas, and more than one test gas. Less obvious but perhaps important, the role of the driver and the length of the shock tube must be considered. The crucial aspect though is the type of measurements to be made. The diagnostics employed must be sensitive over the broad spectrum of test conditions suggested above, must yield quantitative information, and must be straightforward in use. The latter requirement is included in order to permit a large number of experiments to be carried out in a reasonable length of time.

The principal diagnostic device used for these experiments was a wire-mesh potential probe suspended inside the shock tube. See Appendix C for the mechanical and electronic details of this probe. It is not obvious that a potential probe should be employed. In our case it evolved as the most reasonable only through a series of preliminary experiments which demonstrated the existence of strong-potential variations over a distance of a shock tube diameter ahead of the shock wave. The shock tube used was a metal one; thus in principle, an external electrical measurement is not possible without modifying the electrical boundary conditions somewhere in the shock tube. The existence of strong-potential variations ahead of the shock compounds the usual problems encountered in the interpretation of biased Langmuir probes.

A major objection to the measurement of potential versus measurement of say electron or ion number density ahead of the shock is the natural difficulty involved with unfolding the potential variation into other meaningful quantities such as charge number densities. The question can be rephrased as to ask whether or not a physical model can be constructed to interpret the potential measurements. This problem is considered in Chapter 3; a physical model has been formulated based on the observed potential ahead of low-Mach-number argon shock waves.

A few pertinent facts on the potential probe should be mentioned here. A mesh electrode was used to minimize the possibility of compressing precursor charges between the probe and the translational shock. The mesh was suspended by four conducting wire struts, one of which was used to electrically connect the probe to the measuring instrumentation. The shock tube was set up with a dump tank to avoid the extreme environment associated with conditions behind the reflected shock wave. This installation allowed us to make the mesh electrode disposable, i.e., during each test the electrode was blown into the dump tank and replaced with a new one. The potential measured is that which the mesh electrode takes on with respect to the metal walls of the shock tube. The shock tube itself was carefully grounded to an outside driven ground for reference. In order to insure that the potential was being measured and to provide sufficient sensitivity over the whole range of experimental conditions, a high impedance device was needed. The potential was measured across 15 megohms provided by a cathode follower. It should be noted at this time that the mesh-electrode potential data can be considered in a quantitative manner only if there is no plasma ahead of the shock wave. We will demonstrate that this is true for our low Mach-number argon results.

Biased-probe data was collected simultaneously with the potential data. The probe, a 1/16 inch wide by 1/2 inch long silver strip, was mounted flush in the shock-tube wall (see Appendix C for further detail). The biased probe was located 16 inches downstream from the mesh electrode to eliminate interference with the potential measurement. It must be emphasized that the biased probe is a qualitative measurement employed only to help interpret the potential data. The probe was biased positive and negative during the test program and tells us whether electrons, ions, or both are present far ahead of the shock wave. No further interpretation of this data is made. Figure 1 shows a photograph of the shock-tube installation of the two probes surrounded by the associated instrumentation.

Figure 2 gives a sample of the data obtained on a single shot. We will discuss this sample case to establish some nomenclature and to identify some of the prominent features that appear in the data. The bulk of the experimental data will be discussed in segments in later paragraphs.

The two traces on the oscillogram in part (a) of Fig. 2 are labeled "local-potential data". We use the word "local" to denote in the immediate vicinity of the shock wave, i.e., one or two shock tube diameters. The upper and lower traces on this oscillogram are the same output of the mesh-electrode potential probe displayed at two sweep speeds. The "long-time data", part (b) of Fig. 2, is a record of the biased-electrode output (upper trace) and the mesh-electrode potential-probe output (middle trace), from the time the diaphragm opens to the time the shock goes into the dump tank. The third trace on the long-time oscillogram is a time mark which correlates the upper trace of the local data with the long-time data. The start of the blank space in the time mark corresponds in time to the start of the upper trace in the local-potential data. Full detail of the electronic setup used to obtain these traces is given in Appendix B.

It is important to establish the time of shock arrival at the mesh electrode in the local-data oscillograms. This time could be established by calculations which would depend on the shock speed,

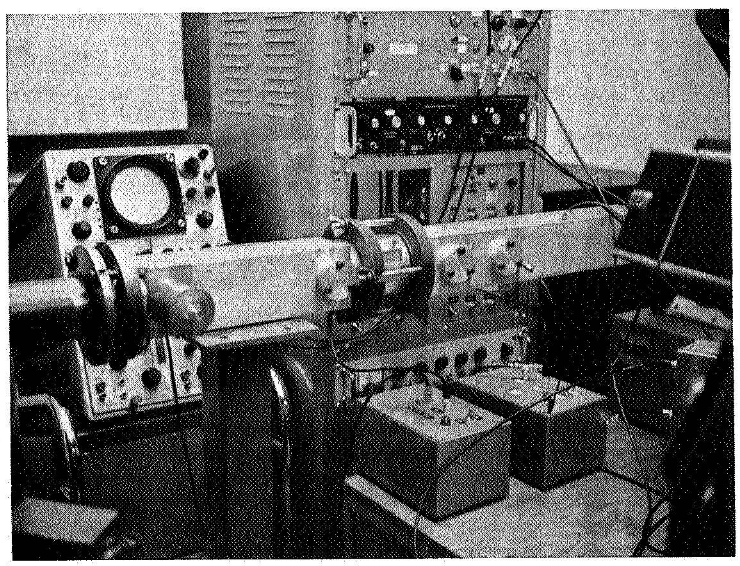

Fig. 1. Photograph of shock-tube installation of precursor instrumentation.

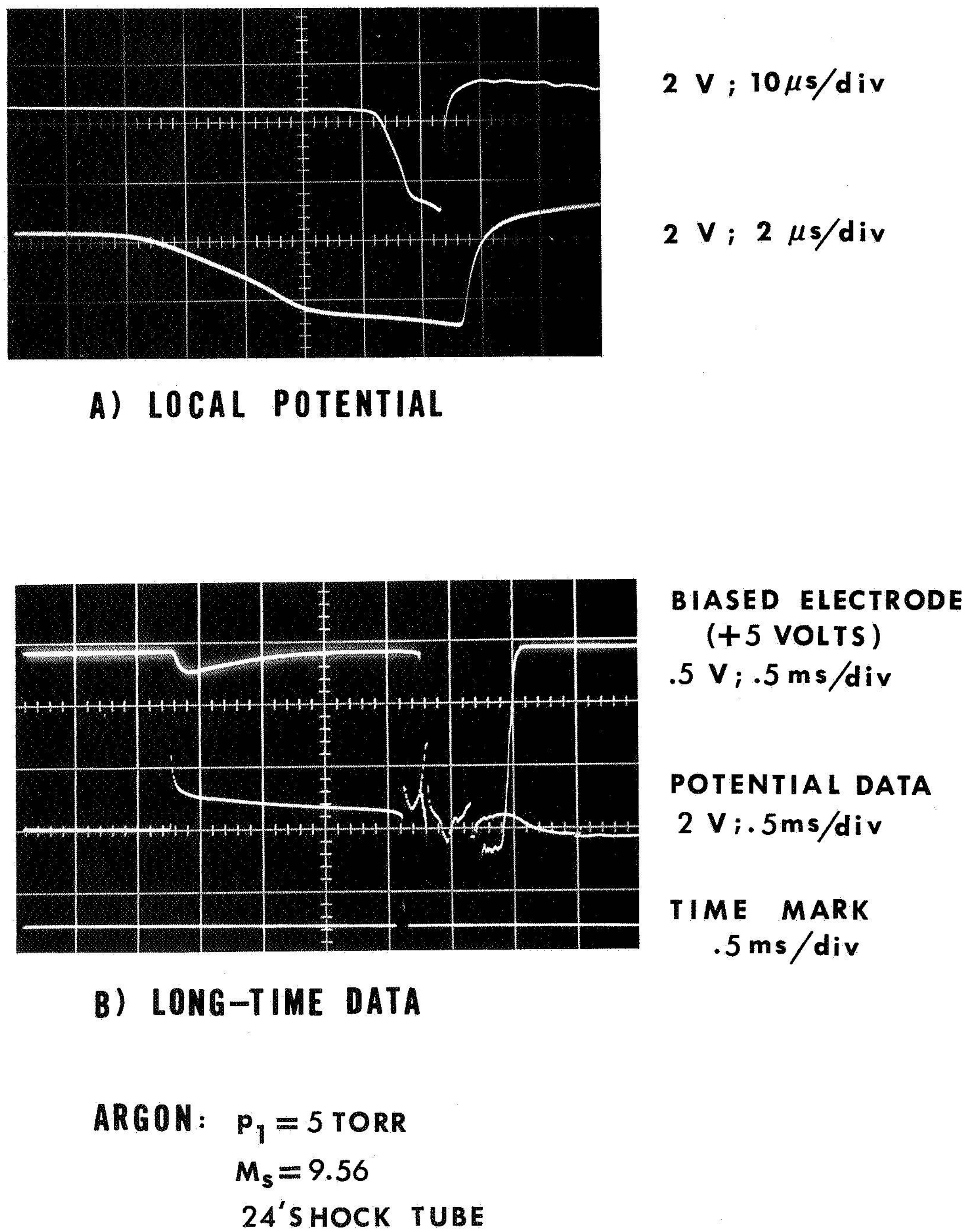

Fig. 2. Sample of data obtained in a single shot.

attenuation, trigger times, and electronic delay times. Rather than depend on calculations a direct experimental determination was made. This was accomplished by mounting an electrode in the center of a dielectric end wall on the shock tube along with a pressure sensor (see Appendix C for the details of this installation). The pressure gauge served to place a time mark on the data corresponding to reflection of the translational shock wave. Figure 3 shows an oscillogram of a potential-probe response and the output of the pressure gauge. This data establishes that the sharp positive rise in the potential data corresponds to the arrival of the shock wave at the probe electrode. From here on we take the sharp positive rise in the potential data as a reference point in time. It is difficulty to assign a precise uncertainty to this reference point, but we feel confident that our determination is accurate to within a microsecond. For data reduction purposes we measure time on the oscillogram from the maximum negative point on the trace; our reading accuracy is $\pm.5$ microsecond.

The very large difference in time scales between the long-time potential data and the local-potential data makes it plausible to assume that these signals are due to different phenomena. That is, we may view the local data as superimposed on the potential profile exhibited by the long-time data. This assumption is made in the data reduction. We take the constant potential level in the local data as a reference and assign the value zero volts to this level. Furthermore we interpret the local-potential profile as a continuous sample of a potential field moving with the shock wave.

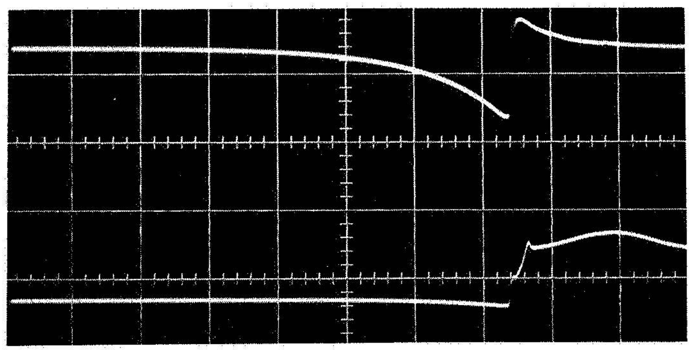

UPPER BEAM:
END WALL POTENTIAL PROBE
2 V, 5 μs/div

LOWER BEAM:
PRESSURE GAUGE
.2 V, 5 μs/div

ARGON
P_1 =10 TORR
M_s=8.1

Fig. 3. Oscillogram of end-wall potential-probe response and pressure-gauge response.

2.2. Local-Potential Measurements.

We now proceed to discuss the precursor data obtained in some detail. In order not to lose the significance of the individual measurements, we will discuss each measurement as a function of all the parameters considered.

Figure 4 shows three oscillograms of the local potential behavior in argon as a function of time before shock arrival (sharp positive rise in voltage corresponds approximately to shock arrival). These three sets of traces illustrate three types of local behavior of the precursor potential. The first one, labeled Type I, appears for all initial pressures when the tests are conducted at approximately Mach 7.0. The Type II signal develops rather abruptly as the shock Mach number is increased beyond a critical value. This critical Mach number increases with decreasing initial pressure. The third oscillogram shows another development in the potential as the shock Mach number is increased further. The Type III signal is characterized by a decreasing magnitude of the negative potential and increasing spatial extent.

A combustion driver was used to generate most of shock waves and their accompanying precursors in these experiments. However some of the low Mach-number shocks (with Type I precursor signal) could also be generated with a cold-helium pressure driver. We observed no dependence in the local-potential profile on the type of driver employed. The biased-electrode data indicates that when the Type III local-precursor signal is observed both electrons and ions can be detected several meters ahead of the shock wave. Further information obtained from the biased electrode will be discussed with the long-time data.

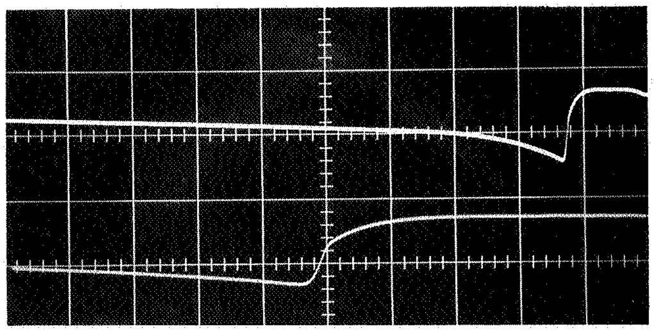

TYPE I

p_1 = 10 TORR M_s = 8.1

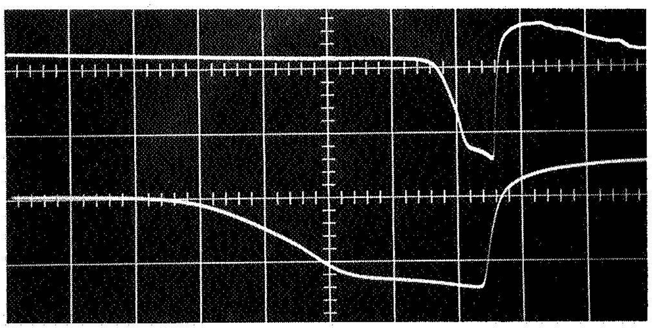

TYPE II

p_1 = 10 TORR M_s = 9.2

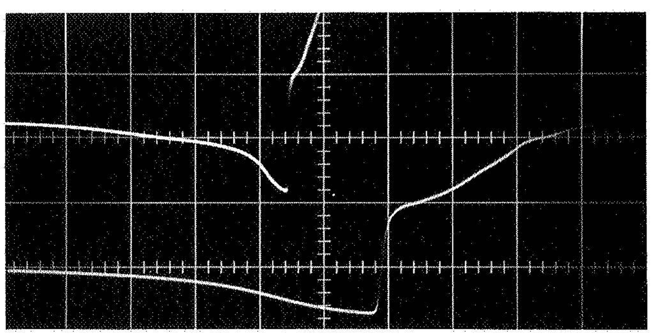

TYPE III

p_1 = 2.5 TORR M_s = 16.2

UPPER BEAMS: 2V, 10 μs/div
LOWER BEAMS: 2V, 2 μs/div

ARGON
24' SHOCK TUBE

Fig. 4. Local-potential data in argon.

Figures 5, 6, and 7 present a compilation of reduced local-precursor potential data for argon (P_1 = 2.5 Torr, 5 Torr, and 10 Torr). These data were obtained from oscillograms like those shown in Fig. 4. The conversion from time on the photograph to distance ahead of the shock wave was accomplished by multiplying the measured time by the measured local shock speed. Note that the data is read from the minimum point on the oscillogram.

These plots exhibit the dramatic change between the Type I and Type II precursor signals. Figure 6 demonstrates the development of the Type III precursor. Note that the 2.5 Torr data (Fig. 7) exhibits a different development of the Type II signal. At the two higher initial pressures the profile seems to steepen, come closer to the shock front, and increase in amplitude as the local Mach number increases. The 2.5 Torr data comes closer to the shock front but does not steepen and decreases in amplitude.

Figures 8, 9, and 10 show a similar compilation of data taken with the shock tube fourteen feet shorter than that used to obtain the previous data. The Mach number shown for these cases is the local value at the station where the data was taken. In the process of taking data with the shock tube at two lengths we observed a severe attenuation of the shock Mach number (see Appendix B). The Mach number attenuates approximately two per cent per foot, thus it is not clear how ten-foot tube data should be compared to twenty-four-foot tube results. Based on the local Mach number each set of data shows roughly the same behavior, that is potential profiles Type I, II, and III appear. Even though we have data for shock waves which have traveled nominally ten

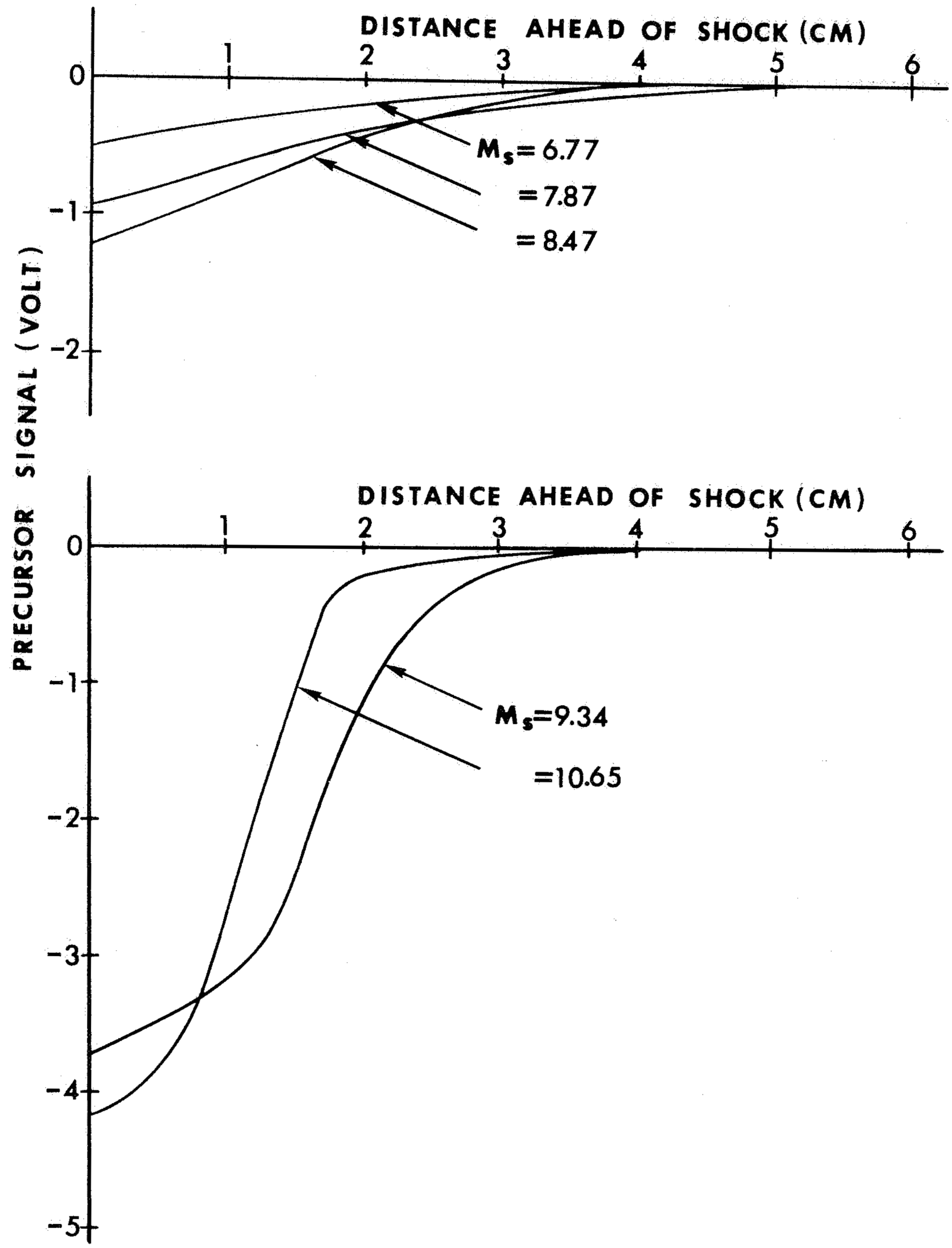

Fig. 5. Compilation of reduced local-potential data; argon, P_1 = 10 Torr, 24 foot shock tube.

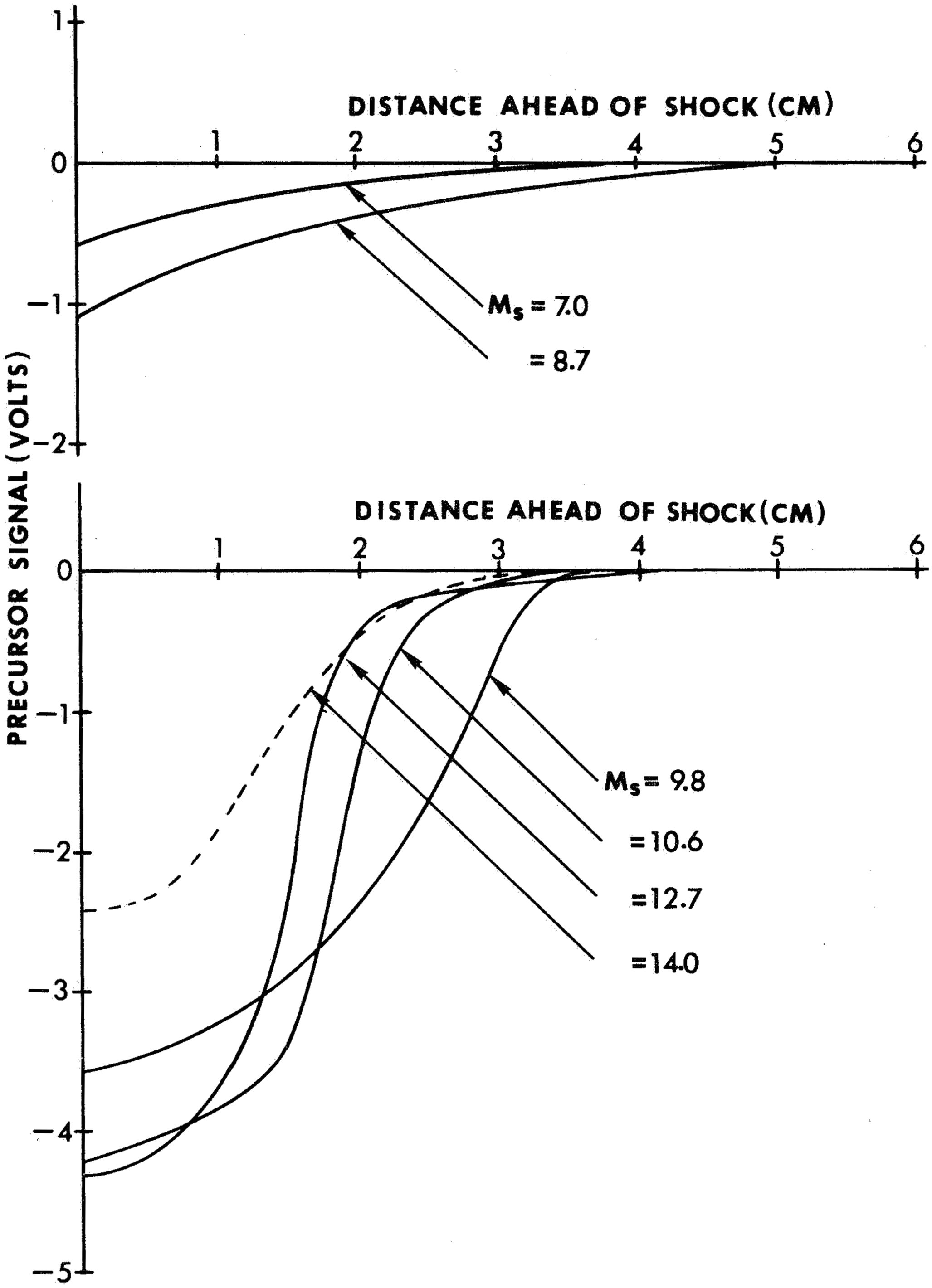

Fig. 6. Compilation of reduced local-potential data; argon, P_1 = 5 Torr, 24 foot shock tube.

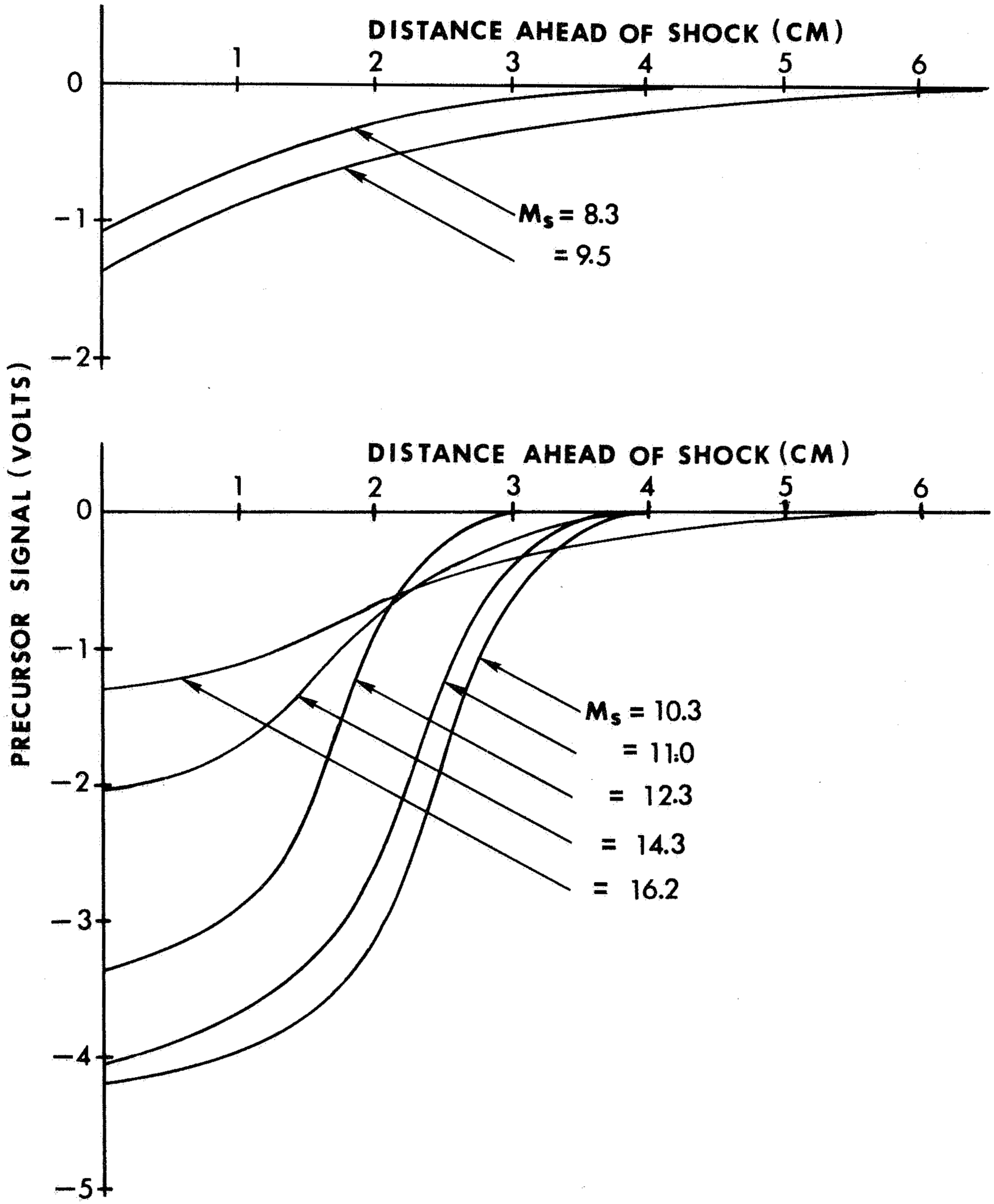

Fig. 7. Compilation of reduced local-potential data; argon, P_1 = 2.5 Torr, 24 foot shock tube.

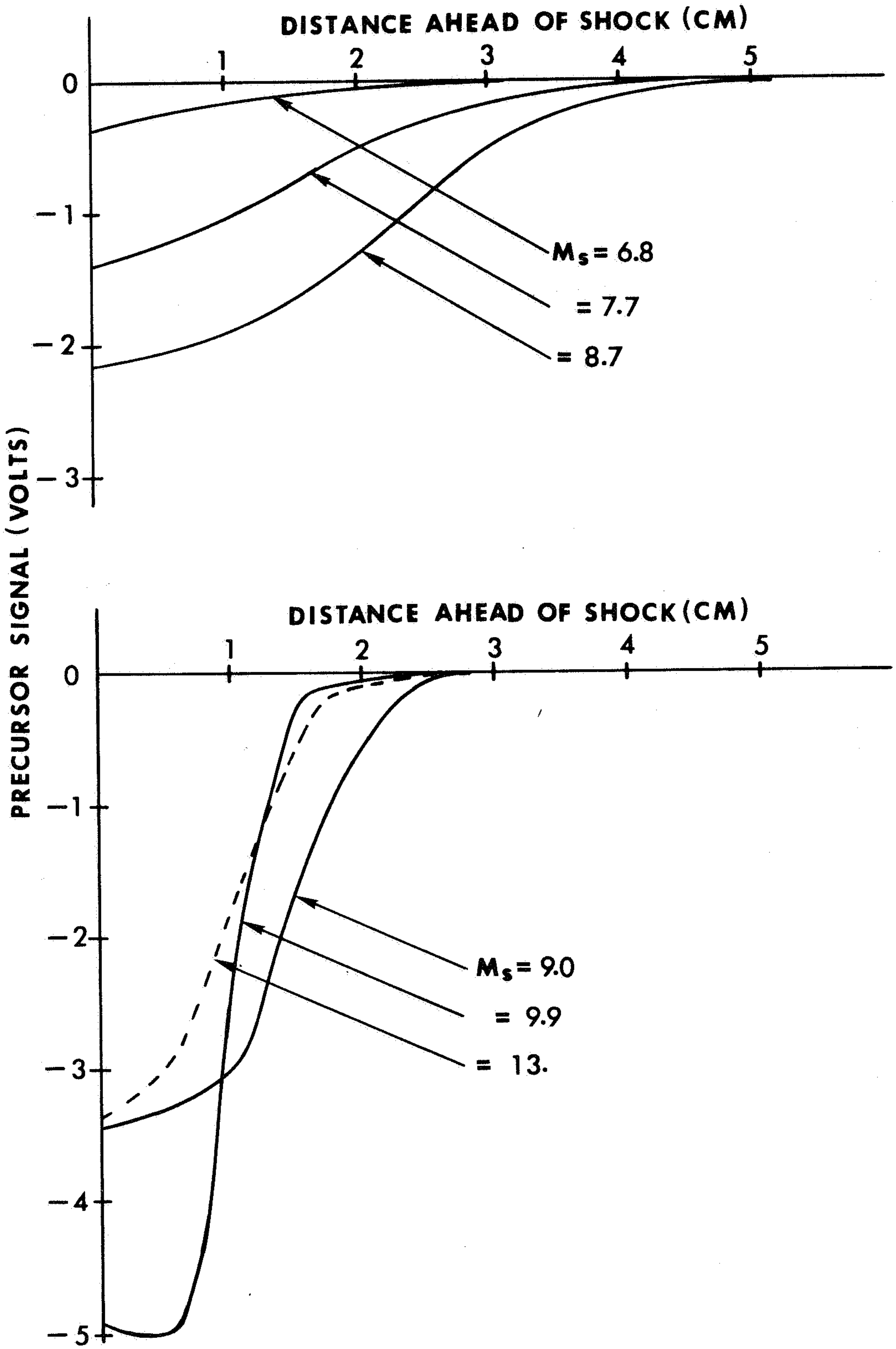

Fig. 8. Compilation of reduced local-potential data; argon, P_1 = 10 Torr, 10 foot shock tube.

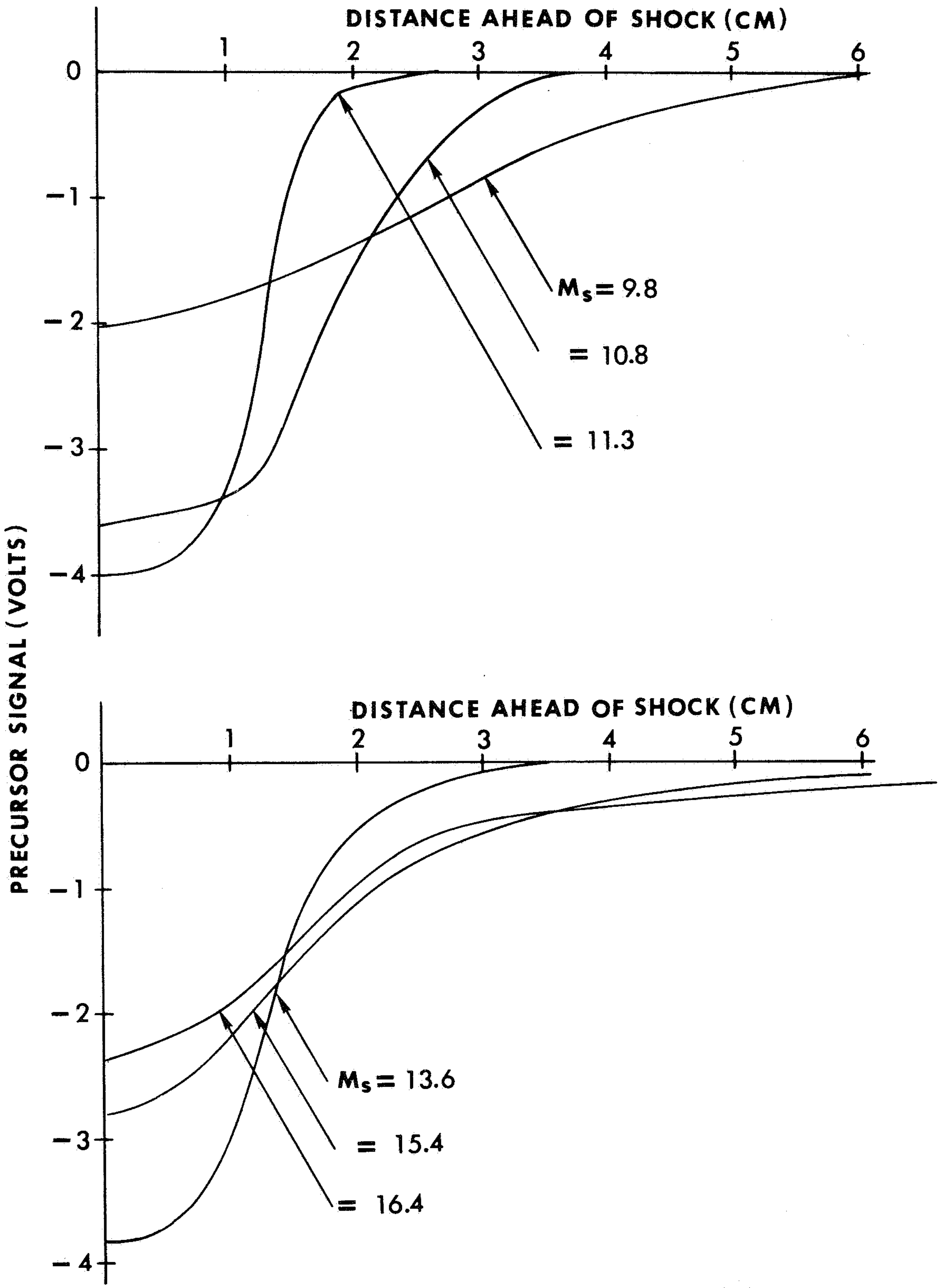

Fig. 9. Compilation of reduced local-potential data; argon, P_1 = 5 Torr, 10 foot shock tube.

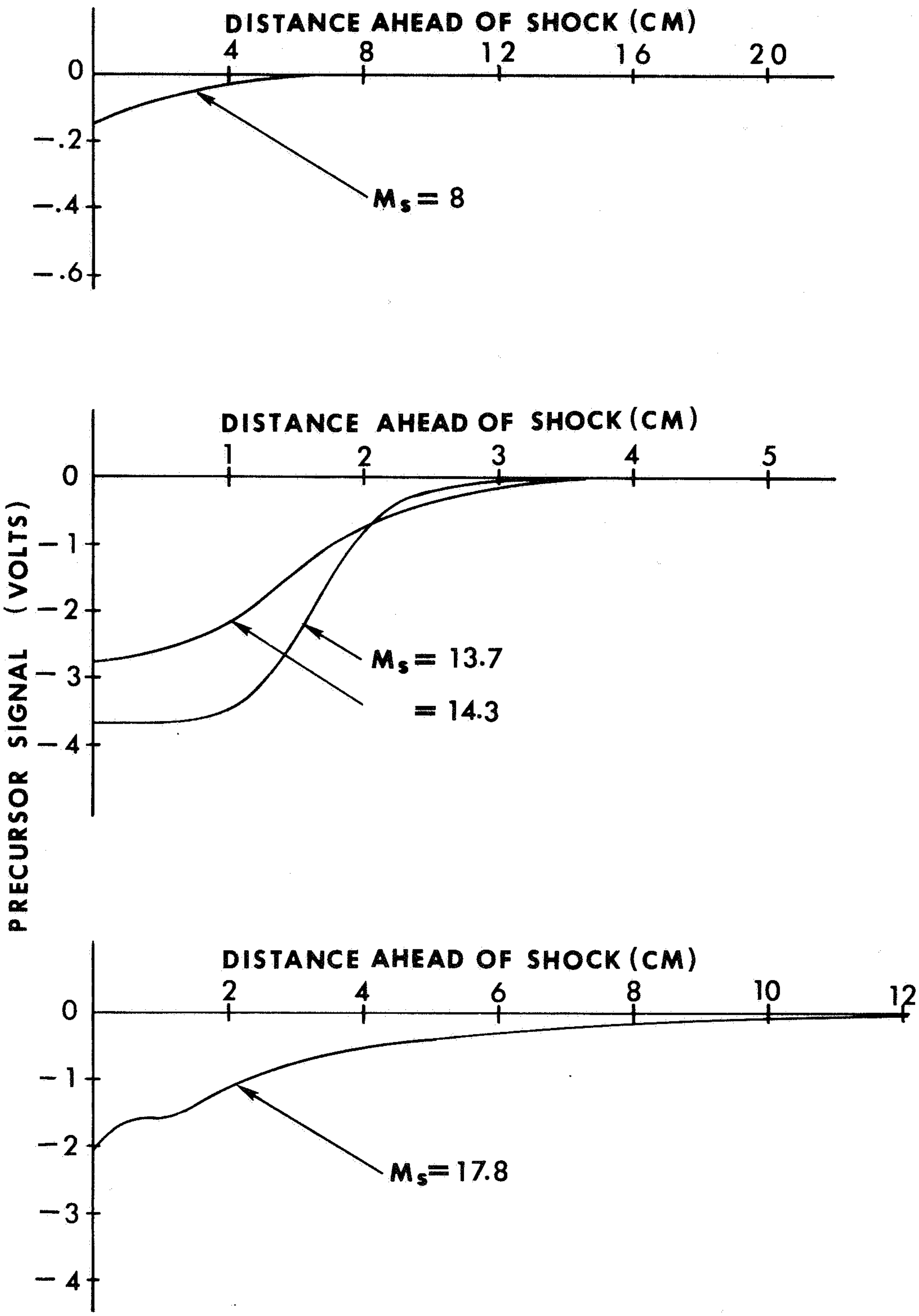

Fig. 10. Compilation of reduced local-potential data; argon, P_1 = 2.5 Torr, 10 foot shock tube.

and twenty-four feet down the shock tube, the severe attenuation problem restricts us from making any quantitative statements about the development of the precursor signal as a function of distance the shock wave travels. However, it is of interest to note that the local Mach number seems to determine the type of precursor present. For example consider a test where the local Mach number is 10 at the ten-foot station and attenuates to approximately 7 at the twenty-four-foot station. For such a case we observe a Type II precrusor at the ten-foot station and a Type I precursor at the twenty-four-foot station.

So far we have shown local-precursor data in argon for different initial pressures Mach numbers, and two lengths of shock tube. To complete this survey, experiments were performed in the twenty-four-foot shock tube in two additional gases; helium and nitrogen. No precursors were observed in 5 Torr helium at Mach numbers 4.9, 5.9, 7.8, and 9.2. The nitrogen experiments proved to be more interesting. A local precursor similar to the Type I result in argon was observed in 5 Torr nitrogen at Mach numbers 10.5, 13.0, and 14.4. The reduced data from these tests is shown in Fig. 11. No precursor was observed at Mach 8.8 with the same initial conditions.

2.3. Long-Time Potential Measurements.

Figure 12 shows two oscillograms of the long-time potential variations of the mesh electrode and the voltage output of the biased electrode. These are argon results in the twenty-four-foot shock tube. The biased-electrode (positive bias, 5 volts) data in Fig. 12a

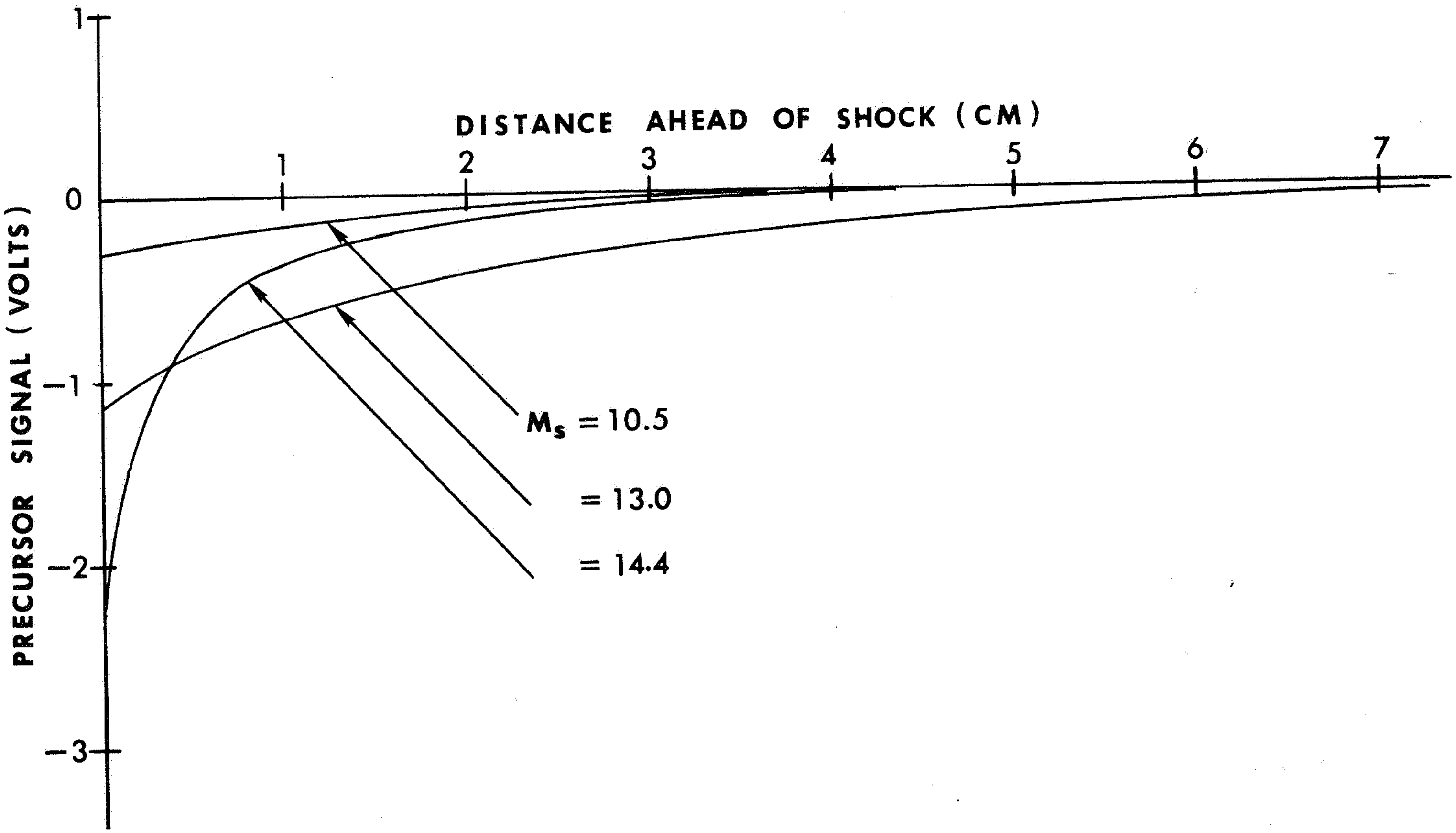

Fig. 11. Compilation of reduced local-potential data; nitrogen, p_1 = 5 Torr, 24 foot shock tube.

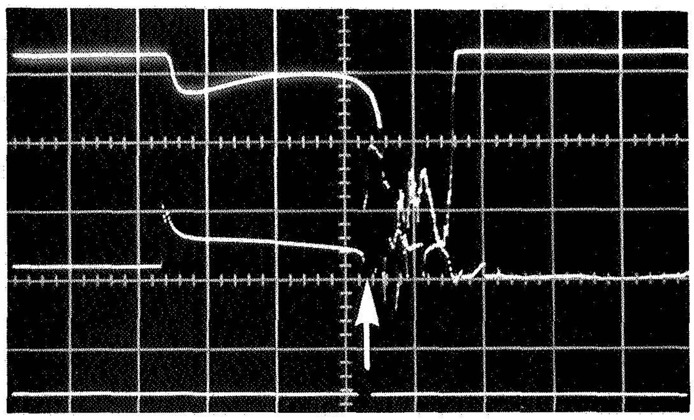

BIASED ELECTRODE
(+5 VOLT)
1 V, .5 ms/div

POTENTIAL DATA
2 V, .5 ms/div

a) p_1 = 5 TORR M_s = 11.7

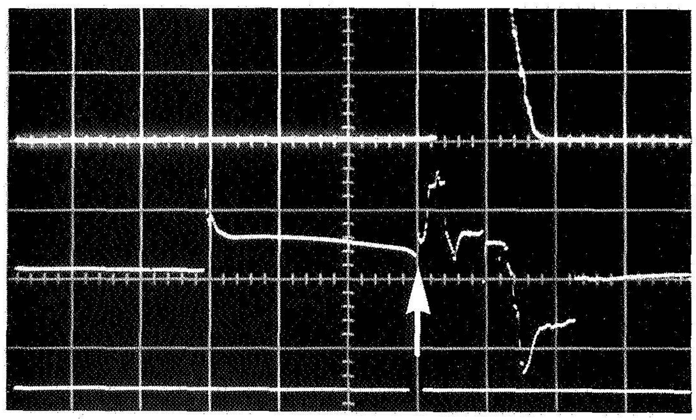

BIASED ELECTRODE
(−10 VOLT)
.5 V, .5 ms/div

POTENTIAL DATA
2 V, .5 ms/div

b) p_1 = 5 TORR M_s = 10.8

ARGON
24′ SHOCK TUBE

Fig. 12. Long-time precursor data in argon.

demonstrates the presence of electrons far ahead of the shock wave. After the diaphragm opens, the mesh electrode undergoes a sharp rise in voltage followed by a rapid decay to a constant positive potential until the shock wave approaches. The arrival of the shock wave is indicated on the potential-data traces by an arrow. Figure 12b shows a similar mesh-electrode signal, but in this case the biased electrode was at negative ten volts. Zero response from the negatively biased electrode, during the time interval where the mesh-electrode potential varies, indicates that few or no positive ions were present far ahead of the shock. The positive potential of the mesh electrode coupled with the fact that only electrons were detected suggests a photoemission effect. That is the electrons detected are photemitted from the surface of shock tube and the surface of the mesh electrode. The positive signal from the mesh electrode results from the fact that a fifteen megohm resistance was used between the electrode and ground, i.e., the source of replacement charges. For the alternate possibility of large scale electron diffusion, one would expect the same biased-electrode results; however the mesh electrode would develop a negative signal due to the buildup of electron charge as on a floating plasma probe. The source of radiation for this photoemission phenomena remains to be determined; the heated combustion-driver components and the shock-heated test gas are two possible sources.

We can investigate these possibilities by changing the driver and changing the test gas. Using the combustion driver and helium test gas, which is transparent to radiation down to 530 Å (23.5 ev),[26] the tests produced no short or long-time potential signals ahead of the shock wave. This is strong evidence that the combustion driver does not act as a radiation source for photemitted electrons.

Further experiments were run with orifices (1/2 and 3/4 inch diameter) placed between the driver gas and argon test gas. Such an orifice, besides reducing the strength of the shock wave produced (see Appendix B), acts as a radiation stop to the driver. Comparing the results with shocks of the same strength produced with lower combustion loading pressures (and no orifice) showed no essential differences. Again, this result indicates that the driver is not responsible.

Finally, given the measured time between the positive spike and the arrival of the shock wave at the potential probe, the local shock Mach number at the probe, and assuming the measured attenuation rate is constant over the length of the shock tube, we can estimate the location of the shock wave when the spike appears. This location turns out to be approximately 1.5 meters from the diaphragm location. This is further evidence that the driver is not the source of radiation producing the photoemission and indicates that the shock-heated test gas is the source.

Figure 13 introduces a further subtlety to this problem. This figure compares two experiments with nearly the same local Mach number in 2.5 Torr argon. As noted on the figure, one result is with a combustion driver and the other a cold-helium pressure driver. Notice the very different long-time potential variations (the local-potential data was practically identical). This at first leads us to suspect the combustion process as the radiation source, but in view of all the evidence presented above an alternate explanation was sought. A reasonable

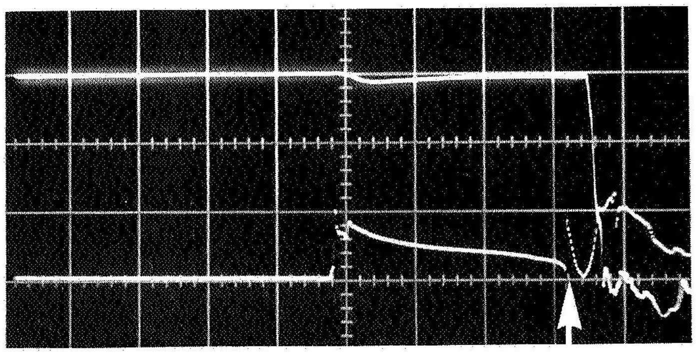

BIASED ELECTRODE
(+5 VOLT)
1 V, .5 ms/div

POTENTIAL DATA
2V, .5 ms /div

a) COMBUSTION DRIVE
p_1 = 2.5 TORR M_s= 8.3

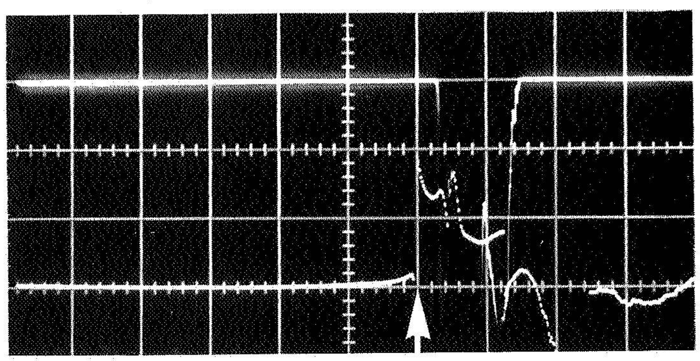

BIASED ELECTRODE
(+5 VOLT)
.5V, .5 ms/div

POTENTIAL DATA
1 V, .5 ms /div

b) HELIUM PRESSURE DRIVE
p_1 =2.5 TORR M_s=8.2

ARGON
24' SHOCK TUBE

Fig. 13. Comparison of long-time data for combustion and cold-helium-driven shock waves in argon.

explanation lies in the fact that the combustion driver causes about fifty percent attenuation in the shock Mach number over the twenty-four-foot length of the shock tube, and this must be compared to an attenuation of two or three percent for the pressure drive case. We propose that the gas heated by a much stronger shock wave gives rise to the radiation which produces the positive spike for the combustion shot, whereas the local data reflects the local Mach number and compares well with the local data obtained with the pressure drive experiment. It is interesting to note that the positive signal just before shock arrival (and just before the negative local-precursor signal) is about the same for both cases.

Figure 14a shows a long-time potential anomaly in a high Mach-number argon shot. This data shows two positive peaks separated by almost 500 microseconds; the biased-probe data indicates the presence of positive ions. We observed this in only one test. The local potential signal (not shown here) was Type III. The two spikes may indicate that the shock wave forms, decelerates somewhat, and then speeds up. This type phenomenon has been observed in combustion-driven facilities previously.[27]

Figure 14b shows another feature observed in a few argon experiments. This data shows a sharp front approximately three hundred microseconds ahead of the shock wave. The amplitude of the voltage step was independent of initial pressure but definitely decreases as the local shock Mach number was increased. The time between the step and the shock arrival also decreased with increasing Mach number.

Figure 14c is an example of the long-time potential variation with nitrogen as the test gas. We note that it is quite different from

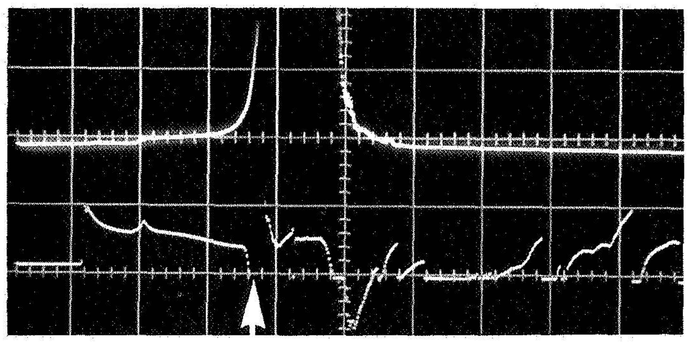

BIASED ELECTRODE
(−20 VOLT)
.1 V, .5 ms/div

POTENTIAL DATA
2 V, .5 ms/div

a) p_1 = 2.5 TORR M_s = 16.2
ARGON

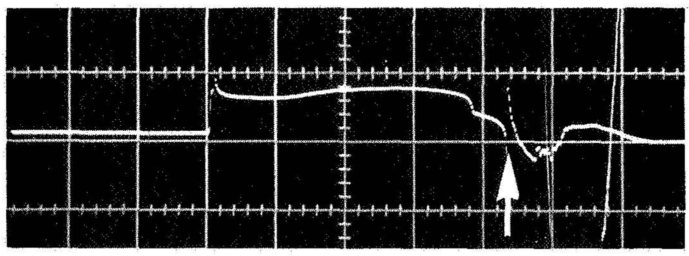

POTENTIAL DATA
2 V, .5 ms/div

b) p_1 = 10 TORR M_s = 7.8
ARGON

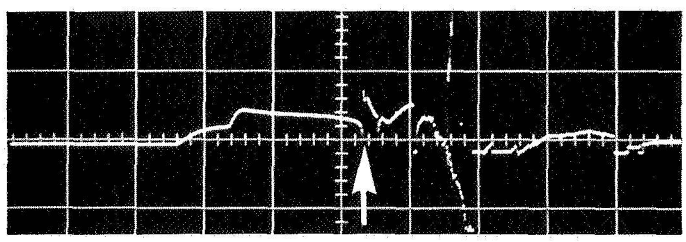

POTENTIAL DATA
2 V, .5 ms/div

c) p_1 = 5 TORR M_s = 14.4
NITROGEN

Fig. 14. Several long-time precursor results in the 24 foot shock tube.

the argon results. No electrons were found in the nitrogen experiments with the same biased-electrode probe and sensitivity used with similar argon cases.

Figure 15 shows two long-time potential measurements taken ahead of argon shock waves in the ten-foot shock tube. These traces demonstrate two interesting features observed in the ten-foot tube. Figure 15a shows the expected signal; however, it seems to be nearly flat before the arrival of the shock wave, more so than the data obtained with the shock tube twenty-four-feet long. The level of this signal was a consistent 1 volt in ninety percent of the seventeen shots where similar data was taken. Figure 15b shows a strange negative dip before the positive rise, this phenomenon occurred in four shots with no apparent correlation to initial pressure or shock Mach number.

The long-time data could be presented in a more quantitative manner at this point; however, its quantitative worth is obscure at this time. The problem of photoemission relates not only to the source of the radiation, which we will pursue further in Section 2.4, but also to the nature of the emitting surfaces. The probable complexity of this latter aspect becomes apparent by examining the amplitude of the positive spike in the long-time potential signal. We found this spike in the argon results varied from 1.6 to 2.8 volts with no correlation to the shock tube parameters, Mach number and initial pressure. The time at which this spike developed seems to be independent of the argon initial pressure but does decrease with increasing Mach number. A rather large scatter was exhibited in this data.

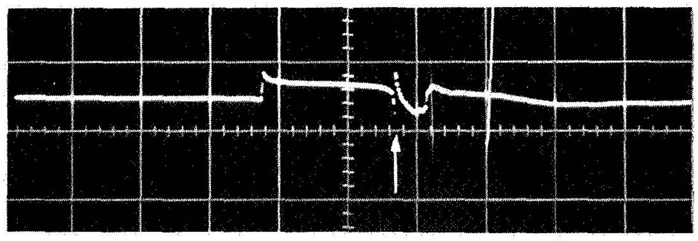

a) 10 TORR ARGON $M_s = 7.7$
5V,.5ms/div

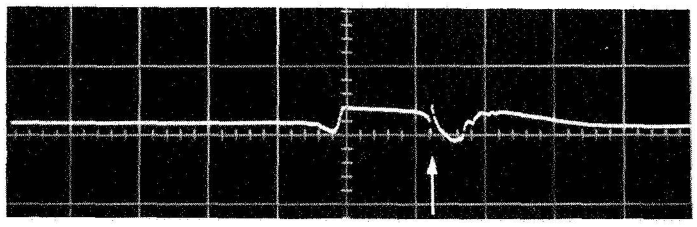

b) 10 TORR ARGON $M_s = 7.5$
5V,.5ms/div

Fig. 15. Long-time potential in 10 foot shock tube.

2.4. Further Qualitative Experiments.

Two radiative phenomena have been observed in this experimental work and have been discussed in the above sections. It has been fairly well established that shock-heated argon can produce significant photoemission from the interior surface of the shock tube. At high Mach numbers some photoionization of impurity gases or the test gas does exist. In this section we present the results of a qualitative experiment aimed at investigating the wave length of the radiation responsible for the above phenomena.

The shock tube was modified slightly to separate the biased electrode from the mesh electrode by a diaphragm. Figure 16 shows a picture of the by-pass piping which allowed us to evacuate both sides of the diaphragm and to fill both sections with the same test gas at the same pressure. The diaphragm was located as shown on the photograph.

The basic notion of this experiment is to isolate a part of the shock tube with a window (diaphragm) of known transmission. The first test was made with an aluminum diaphragm to check the zero transmission limit. The usual mesh electrode signal was obtained and the biased electrode detected no electrons. Corning 0211 Microsheet Glass* (0.020 inch thickness) was used as the next window. The transmission characteristics[28] of this glass are reproduced in Fig. 17. The null result was again obtained. This indicates the radiation is below 3600 Å (3.44 ev), i.e., in the ultraviolet. The experiment was carried one step further to a 0.0005 inch Mylar window, which also gave the null

*We acknowledge the generosity of Corning Glass Works for supplying a sufficient sample of this glass to conduct our experiments.

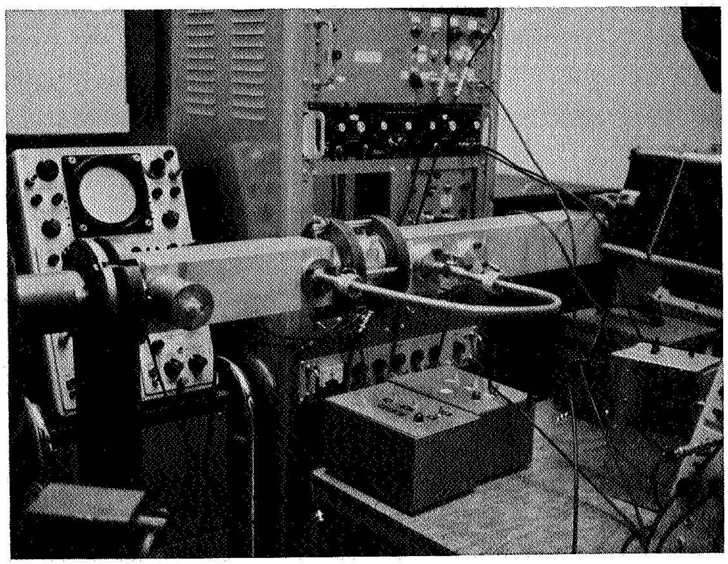

Fig. 16. Photograph of shock-tube installation of the precursor instrumentation and by-pass piping for qualitative radiation experiment.

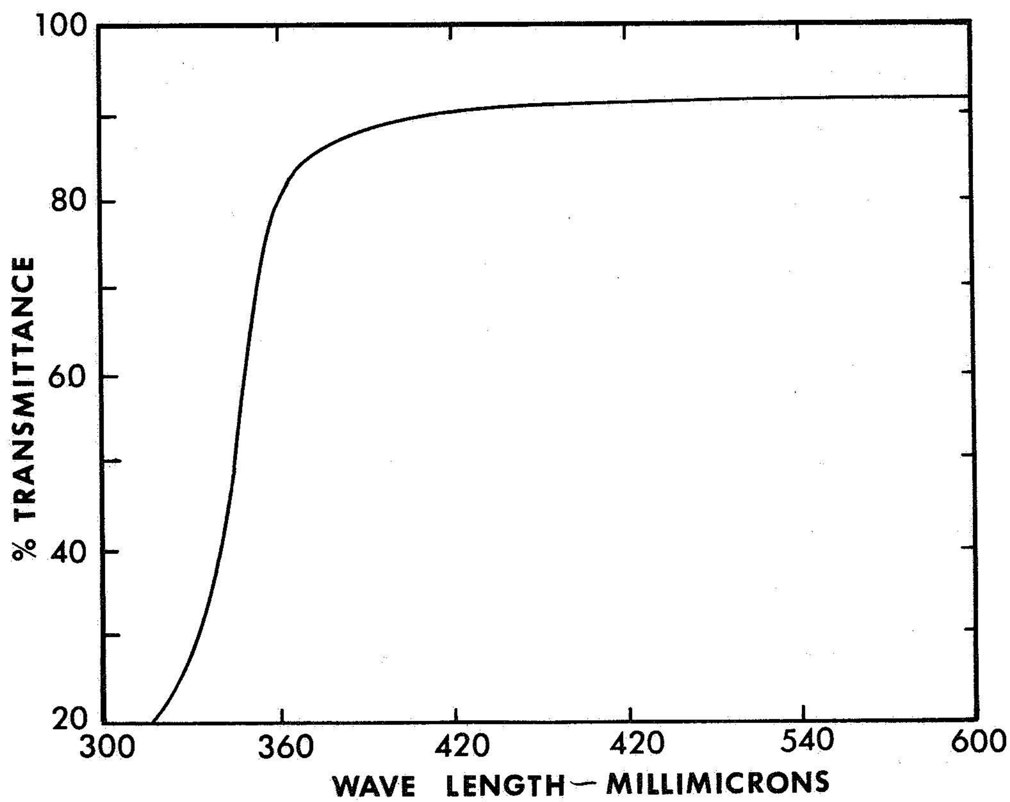

Fig. 17. Transmission characteristics of Corning 0211 Microsheet Glass.[28]

result. To guard against the possibility of not seeing a reduced result, the biased electrode sensitivity was increased by a factor of ten compared to the earlier experiments.

This type of experiment could be carried to more conclusive results by going to micron thick windows[29] (films). However, this was not pursued in the current experimental work.

2.5. Summary of Experimental Results and Qualitative Conclusions.

An over-all view of shock-tube precursor phenomena has been obtained. We considered three test gases: argon, helium, and nitrogen. Potential precursors were found ahead of argon and nitrogen shock waves. With the potential probe we have identified three types of precursors ahead of argon shock waves. The low Mach-number-range (6.5 to 9) potential profiles ahead of argon shock waves are smooth, starting negative at the shock wave and increasing uniformly toward zero as a function of distance ahead of the shock wave. The negative amplitude and the spatial extent increase as the Mach number increases. These results are considered extensively in the next chapter. The next development in the argon potential profile occurs at Mach numbers and initial pressures where significant real gas effects start to appear in the final equilibrium state. The potential results at these and greater Mach numbers change drastically in magnitude and shape. Finally as the Mach number is increased beyond a higher limit (which also depends on initial pressure) a marked decrease in amplitude of the potential and an increase in spatial extent was observed. This last development has been linked with photoionization of the test gas and/or impurity gases. Figure 18 presents a map in Mach number and initial-pressure space for the argon findings.

The potential ahead of nitrogen shock waves behaves initially like the low Mach-number argon results, with the significant fact that this behavior persisted to a much higher Mach number ($M_s = 13.0$). Beyond this Mach number a drastic change occurs both in amplitude and shape. The new shape was not like the argon shape at intermediate Mach numbers.

Photoemission from the potential-probe electrode and shock-tube-interior surface was observed at large distances (meters) ahead of argon shock waves and to a lesser extent ahead of nitrogen shock waves. Our experiments indicate that the shock heated test gas is the radiation source. Because of large shock attenuation effects due to the combustion driver these photoemission effects should not be associated with the measured local Mach numbers. The wave length of the radiation responsible for photoemission and/or photoionization was determined to be shorter than 3600 Å.

Experiments were performed with the shock tube ten-feet and twenty-four-feet long. The severe attenuation problem restricts the value of these results. Therefore, these experiments have not indicated whether the precursor-potential profiles are steady or unsteady in the shock-wave coordinates.

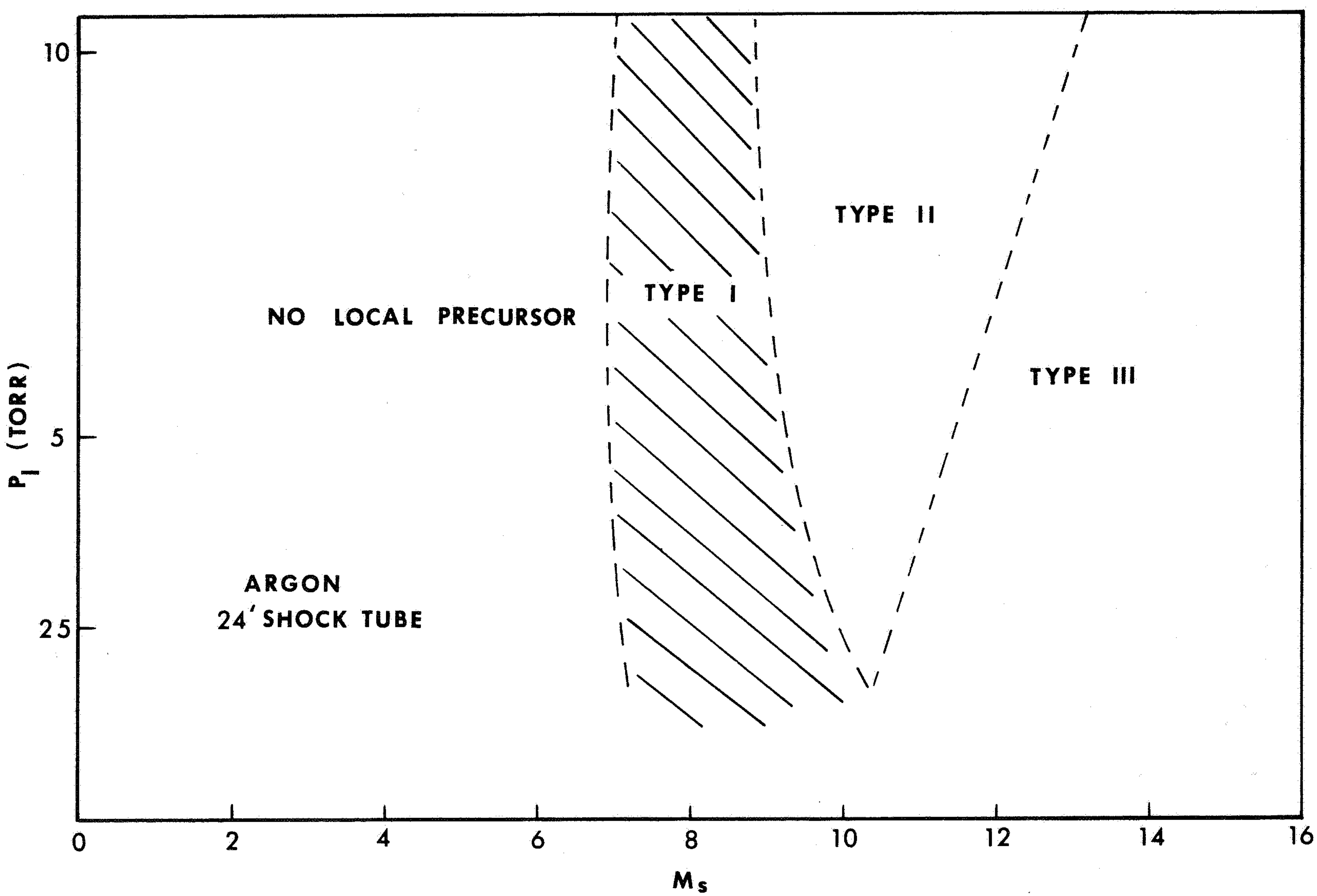

Fig. 18. Map in p_1 vs. M_S space for argon local-potential precursor results.

3. LOW MACH-NUMBER ARGON-PRECURSOR ANALYSIS

It was noted in Section 2.2 that the measured local-potential profiles ahead of the shock wave change character as the Mach number is increased. This section is devoted to the low Mach number (6.5 to 9), Type I results where the potential profiles are smooth, starting negative at the shock wave and increasing uniformly toward zero as a function of distance ahead of the shock. The potential rises sharply to a positive value during shock passage. The general shape of this curve suggests a charge double layer or dipole structure at the translational shock front. Such a structure would result from a slight separation of ions and electrons due to electron diffusion at the shock front.

3.1. Electrostatic Model.

To test the above hypothesis we can employ some simple electrostatic ideas. Consider first the potential on the axis of symmetry of a dipole disk of radius a. For charge separation δ much less than x (see Fig. 19) the potential is

$$\varphi_{dp}(\tilde{x}) = \varphi_0 \left(1 - \frac{\tilde{x}}{\sqrt{\tilde{x}^2 + 1}} \right)$$

where

$$\varphi_0 = \frac{-\sigma\delta}{2\epsilon_0}$$

$$\tilde{x} = \frac{x}{a}$$

σ = charge per unit area

ϵ_0 = permittivity of vacuum,

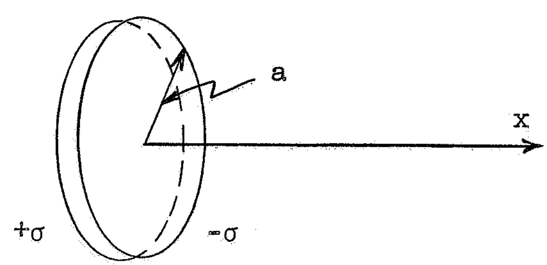

Fig. 19. Sketch of dipole disk.

This dipole solution is shown in Fig. 20. A typical experimental-potential profile has been normalized and matched at the potential minimum point with the dipole solution. Note that the dipole strength parameter is negative by definition in these considerations so that

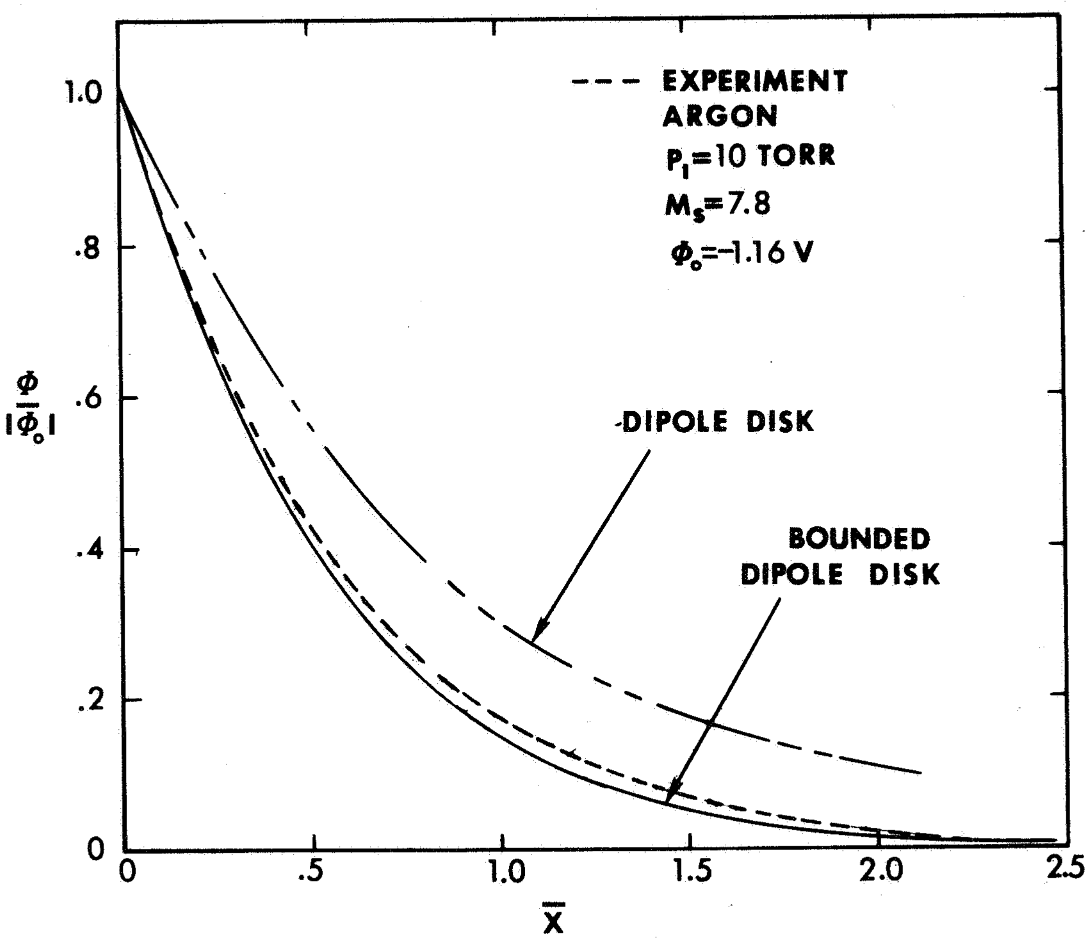

Fig. 20. Comparison between simple electrostatic model and experiment.

$\varphi/|\varphi_0|$ is a positive function. The comparison between the experiment and the dipole disk solution shows that the measured potential falls more rapidly than the dipole-disk solution. This is presumably due to the grounded side walls of the shock tube. We can show this by surrounding the dipole disk with a grounded cylinder. The solution for the potential distribution along the axis of the cylinder is

$$\varphi(\tilde{x}) = \varphi_0 \sum_{\ell=1}^{\infty} \frac{\exp(-k_\ell a\tilde{x})}{k_\ell a\, J_1(k_\ell a)}$$

where the k_ℓ's are defined by

$$J_0(k_\ell a) = 0 .$$

This solution is also shown in Fig. 20. As expected, the grounded boundary pulls the potential down more rapidly. The experimental result now compares very favorably to this simple analysis. Note at this time that $\tilde{x} = x/a$ scales the problem. Many improvements can be made to this analysis, such as accounting for the presence of the probe electrode, the square geometry of the shock tube, etc. Rather than pursue this analysis further, we take the above results as a guideline to examine the gasdynamic situation at and ahead of the shock wave to gain insight into the behavior of the charged particles that leads to a dipole structure.

Before proceeding, it is worthwhile to examine the order of magnitude of the quantities involved in the dipole strength parameter. For the experiment shown in Fig. 20, the maximum negative voltage was 1.16

volts. This would correspond to the dipole strength:

$$\varphi_0 = -1.16 = \frac{-\sigma\delta}{2\epsilon_0} \; .$$

Assuming the charge separation is of the order of the translational shock thickness, say 0.1 mm, we find the total number of electrons on a dipole disk with an area equal to the shock tube cross-sectional area is of the order of 10^{11}. In order to estimate the degree of ionization needed to explain this phenomenon we assume that the 10^{11} electrons occupy a volume equal to the volume of the translational shock wave. This volume is approximately 0.25 cm^3. Thus we take the following as an estimated electron number density

$$n_e \approx 4 \times \frac{10^{11}}{cm^3} \; .$$

For the shock tube conditions of interest the heavy particle number density behind the translational shock wave is the order of $10^{17}/cm^3$. Thus the degree of ionization is given by

$$\alpha \cong \frac{10^{11}}{10^{17}} \approx 10^{-6} \; .$$

These rough calculations indicate that significant electrostatic effects are possible with electron number densities very small compared to those observable by common techniques such as the Mach Zehnder interferometer.

3.2. Equilibrium Model and Preliminary Analysis.

Consider a shock wave propagating down the shock tube into quiescent test gas at initial pressure P_1 and temperature T_1 (room temperature). A shock wave propagating into a real gas compresses and heats the gas. The gas initially behaves like a perfect gas since the translational degrees of freedom are excited within a couple collision times. This part of the structure we refer to as the translational shock and conditions behind it as the "frozen" conditions. Excitation of internal degrees of freedom, dissociation, and ionization take many more collisions; hence relaxation to equilibrium among all degrees of freedom is typdified by finite relaxation times. Electron production in the rare gases proceeds initially by atom-atom collisions and "impurity produced electron" - atom collisions until sufficient electrons exist for electron-atom collisions to be the dominant ionization mechanism. Electron-atom collisions are so efficient for ionization, that the approach to equilibrium ionization takes on the character of a front. The approach to equilibrium ionization in rare gases has received much attention.[2,25,30] For the low Mach numbers in argon being considered now, the equilibrium degree of ionization is small and is far back from the translational shock front (e.g., $M_s = 8.5$, $p_1 = 1$ Torr, $\alpha = .002$, $\ell \geq 10$ cm). Hence for the present work, we are interested in the relatively few electrons and ions at the translational shock front.

To construct a model for the equilibrium distribution of electrons immediately ahead of the translational shock we assume the following:

a) The ion diffusion is negligible compared to the electron diffusion.

b) The electron diffusion does not alter the macroscopic structure of the heavy particle translational shock.

c) The electrons ahead of the shock are thermalized among themselves at temperature T_e.

d) In addition to electrostatic and pressure forces the electrons ahead of the shock experience a drag force due to collisions with the neutral gas.

It is unreasonable to assume the electric field set up in a shock tube by electron diffusion is one-dimensional. This is especially true in the case of a metal shock tube with grounded walls. However, it is realistic to assume a high degree of symmetry about the centerline of the shock tube. For this reason we consider a centerline analysis.

We now formulate an axial electron force balance for a centerline analysis of the equilibrium distribution of electrons. We take our coordinate system as fixed to the translational shock wave with positive x ahead of the shock. Figure 21 illustrates the model we are considering. We consider three forces in the axial direction: 1) a positive electron pressure gradient, 2) the electrons ahead of the shock experience an electrostatic force due to charge separation, and 3) a negative friction or drag force due to collisions with the test gas atoms flowing into the shock wave. The axial force balance may be written

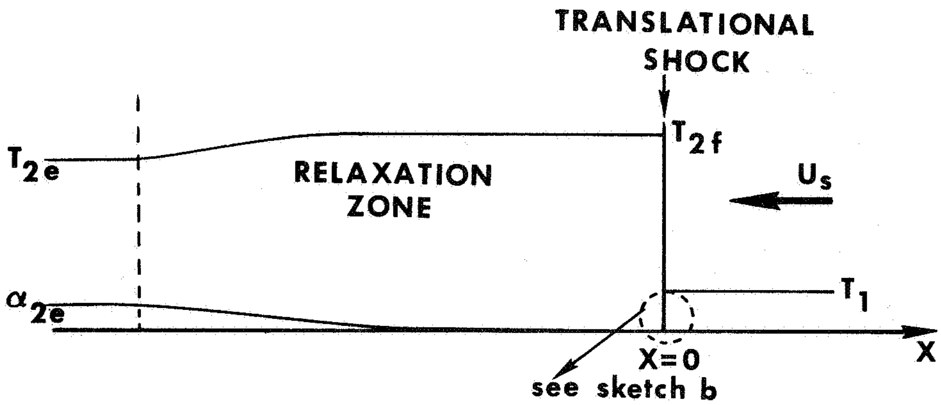

a) Noble gas ionization relaxation.

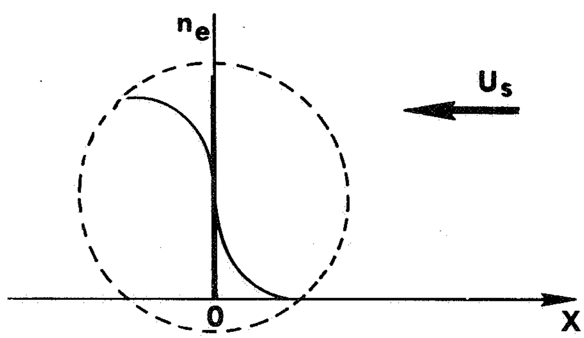

b) Postulated electron distribution at the translational shock front.

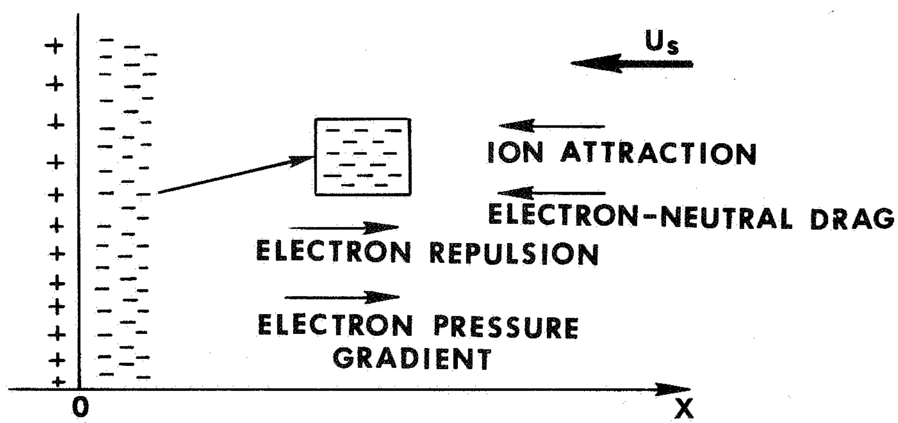

c) Schematic of forces acting on an electron fluid element ahead of the shock front.

Fig. 21. Illustration of the equilibrium model.

$$kT_e \frac{dn_e}{dx} = en_e \frac{d\varphi}{dx} - en_e D \tag{1}$$

where

k = Boltzmann constant

T_e = electron temperature

n_e = electron number density

φ = electrostatic potential

e = magnitude of electron charge

D = drag force/electron charge

We have assumed the drag term is functionally dependent on the axial coordinate only through the electron number density. This dependence has been expressed explicitly in equation (1) for mathematical convenience. The collision model and the dependence of D on the electron temperature, shock speed, and test gas will be discussed below. The quantity D is always positive.

It should be noted at this point that this model deals only with electrons which were behind the translational shock and have diffused forward. This does not preclude the existence of a neutral plasma cloud ahead of the shock. If a neutral plasma cloud does exist, the electrons considered here should be viewed as an excess number over those existing in the cloud. Also this model should not be confused with the models of Weymann and Groenig discussed in Appendix A. These models dealt with diffusion from the equilibrium electron front as opposed to the translational shock front considered here.

There are several physical consequences of equation (1) which we can explore with our experimental knowledge. A typical local-potential profile is sketched in Fig. 22. Since n_e is always a positive function,

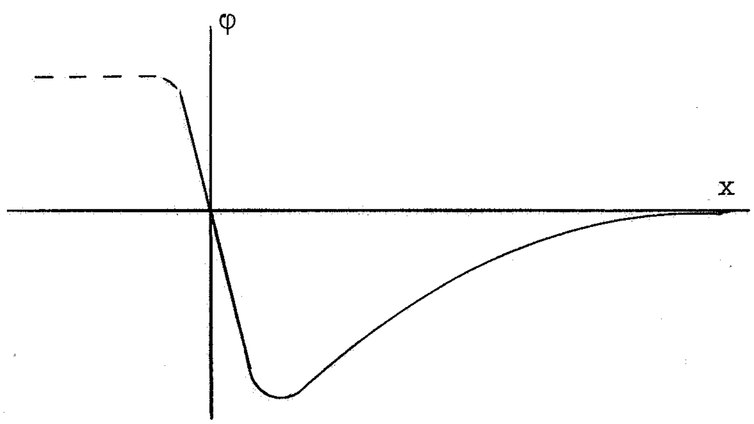

Fig. 22. Sketch of low Mach-number argon-precursor potential.

we note the following results:

$$\frac{d\varphi}{dx} = 0$$

$$\frac{dn_e}{dx} = - \frac{en_e D}{kT_e} \qquad \text{ahead of the shock} \tag{2}$$

The derivative of equation (1) with respect to x is,

$$kT_e \frac{d^2 n_e}{dx^2} = en_e \frac{d^2\varphi}{dx^2} + e \frac{dn_e}{dx} \frac{d\varphi}{dx} - eD \frac{dn_e}{dx}$$

or

$$kT_e \frac{d^2 n_e}{dx^2} = en_e \frac{d^2\varphi}{dx^2} + \frac{e^2 n_e}{kT_e} + \frac{e^2 n_e}{kT_e} \left(\frac{d\varphi}{dx} - D\right)^2$$

Now we can investigate the inflection point in the potential profile; i.e., the point of zero curvature; we find the following result:

$$\frac{d^2\varphi}{dx^2} = 0$$

$$\frac{d^2 n_e}{dx^2} = \frac{e^2 n_e}{kT_e} \left(\frac{d\varphi}{dx} - D\right) > 0 \quad \text{ahead of the shock} \tag{3}$$

Lastly we can integrate equation (1) assuming the approximate boundary conditions $\varphi = 0$ at $x = 0$ and $n_e = n_e^*$ at $x = 0$,

$$n_e = n_e^* \exp\left[\frac{e}{kT_e} (\varphi - Dx)\right] \quad \text{ahead of the shock} \tag{4}$$

The first observation to be made from the above results is that the only way n_e can become zero is for the potential to go to negative infinity. However, we know from our experiments that the potential is bounded. This means that specifying $n_e = 0$ at $x = \infty$ is an incorrect boundary condition and would produce erroneous results.

Results (2) and (3) show that at the potential minimum the slope of the n_e profile is negative and at the inflection point in the potential the curvature of the n_e profile is positive. The positive curvature depends on the magnitude of the drag, D. For large drag the curvature is very large which corresponds to a rapid decay of the n_e profile. As the drag and hence the curvature decrease, the n_e profile spreads out. The artificial limit of zero drag causes the number density to increase asymptotically to n_e^*. Figure 23 shows a sketch of these different cases.

Considering the simplified sketch in Figure 24 of the experimental-potential curve we can estimate the number density of electrons at the potential minimum (n_e'). From equation (4) we have

$$n_e' = n_e^* \exp[\frac{e}{kT_e} (-\varphi^\infty - D\delta)]$$

and assuming that the drag is zero behind the shock, the number density behind the shock (n_e^∞) is given by,

$$n_e^\infty = n_e^* \exp[\frac{e}{kT_e} \varphi^\infty]$$

thus,

$$\frac{n_e'}{n_e^\infty} = \exp[- \frac{e}{kT_e} (2\varphi^\infty - D\delta)]$$

We would expect $D\delta \ll 2\varphi^\infty$, therefore we have

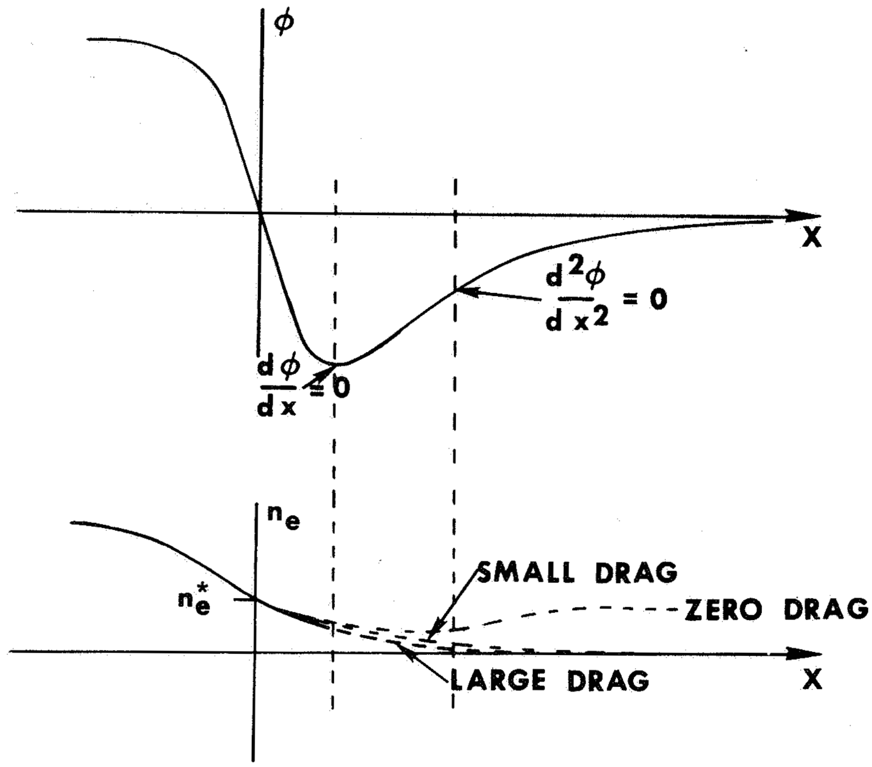

Fig. 23. Results of preliminary analysis of equilibrium model.

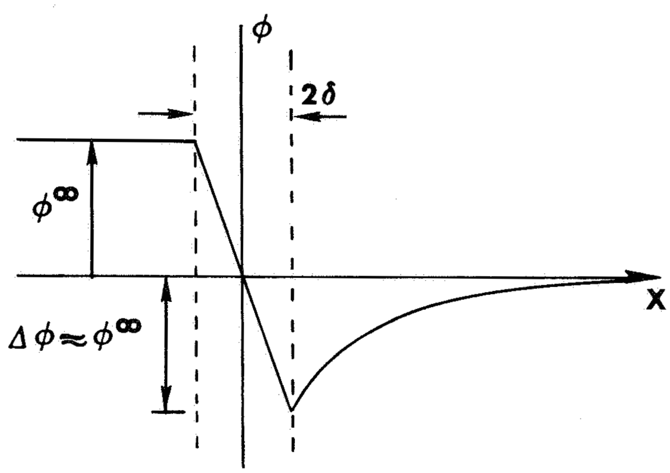

Fig. 24. Simplified low Mach-number potential profile.

$$\frac{n_e'}{n_e^\infty} \approx \exp\left(\frac{-2e\varphi^\infty}{kT_e}\right)$$

For a typical value of φ^∞, say 1 volt, the above ratio is approximately 10^{-2} for $T_e = 5000°$ K and 10^{-1} for $T_e = 10000°$ K.

It should be noted that the drag or friction on the electrons ahead of the shock may cause significant heating of the electron precursor cloud. This possibility will be explored in a later section.

In the above preliminary considerations we have leaned heavily on the experimental potential curves ahead of the shock. The task now is to solve the equilibrium equation simultaneously with Poisson's equation to find both the electron density and the potential in a consistent manner.

3.3. Approximate Solution to the Equilibrium Model.

In the last section of this chapter we formulated a model for the steady-state equilibrium distribution of electrons ahead of the shock wave. The governing equation for the electron distribution on the centerline of the shock tube is the axial force balance,

$$kT_e \frac{dn_e}{dx} = en_e \frac{d\varphi}{dx} - en_e D \quad . \tag{5}$$

The integral of this equation is

$$n_e = n_e^* \exp\left(\frac{e\varphi}{kT_e} - \frac{eDx}{kT_e}\right) \tag{6}$$

where n_e^* is the electron number density at the x location where

$$\frac{e\varphi(x)}{kT_e} = \frac{eDx}{kT_e}$$

Since both $n_e(x)$ and $\varphi(x)$ are unknown we must add another equation to the formulation. Recall from our discussion of the pure electrostatic model that one-dimensional electrostatics are not appropriate for this problem. Thus in order to complete this formulation the three-dimensional Poisson's equation

$$\nabla^2\varphi = -\frac{en_e}{\epsilon_0}$$

plus electrostatic boundary conditions must be included. Note that $\varphi(x)$ must be a solution, specialized to the centerline, of the above equation. The exact solution to Poisson's equation coupled with equation (6) is a difficult if not impossible problem.

Rather than attempting to solve this difficult problem we will seek an approximate solution. We need a solution which is valid on the centerline of the shock tube and which takes into account the three-dimensional nature of the electrostatic field. For electrostatic considerations we will use cylindrical coordinates with radial symmetry. The effective radius of the shock tube will be taken such that the cross-sectional area of the cylindrical tube equals the cross-sectional area of the square shock tube.

We consider a thin disk of the electron gas in the vicinity of the shock wave and assume that such a disk may be considered a conductor and hence an equal potential surface. Charge placed on a conducting disk will distribute itself radially so that the disk is at a uniform potential. We are interested in the potential field along the axis of symmetry of the charged disk. The potential field of the conducting disk depends on the radial distribution of charge and hence the electrostatic boundary conditions at the edge of the conducting disk. To construct the potential due to the electron distribution ahead of the shock wave we add up the contributions of many charged disks. The amount of the charge on each disk depends on its axial location. We take the limit of an infinite number of disks, infinitely thin, to represent the axial distribution of electrons. The potential field due to the axial distribution of charge is a superposition of the disk fields. This superposition is an integral over the charge distribution weighted by the potential due to each conducting disk.

Since we assume that the positive ion diffusion in the axial direction is neglibible compared to the electron diffusion, we must consider the positive charge left behind by the diffusing electrons. We assume that these positive charges are distributed on a single conducting disk. At the outset we assume this disk of positive charge is located at the translational shock front; after we have solved the problem, we will examine this assumption by moving the disk back from the shock slightly. We need to know the number of positive charges at the origin in order to complete this model. We assume there is no electron current to the shock tube walls, hence there are no electrons lost ahead of the shock. With this assumption overall charge neutrality is preserved, thus the number of excess ions at the shock front is equal to the number of electrons ahead of the shock.

We now proceed to put the above model into mathematical form. Again considering the axis of symmetry, we let $h(|x-\xi|)$ represent the electrostatic potential at the point x due to a unit positive charge placed on an infinitely thin conducting disk located at point ξ. Then the potential due to the electron distribution along the center-line of the shock tube is given by

$$\varphi^{(-)}(x) = - \int_0^\infty n_e(\xi)\ h(|x-\xi|)\ \pi a^2\ d\xi$$

The positive charge contribution is given by

$$\varphi^{(+)}(x) = \int_0^\infty n_e(\xi)\ h(x)\ \pi a^2\ d\xi$$

Combining the positive and negative charge contributions, the electrostatic potential, in terms of the unknown electron number density distribution, is

$$\varphi(x) = h(x) \int_0^\infty n_e(\xi)\ \pi a^2\ d\xi - \int_0^\infty n_e(\xi)\ h(|x-\xi|)\ \pi a^2\ d\xi \quad (7)$$

Before discussing the choice of $h(|x-\xi|)$ let us complete the formulation of the model by substituting the above expression for φ in equation (6). This yields the following non-linear integral equation

$$\ln \frac{n_e}{n_e^*} = \frac{e}{kT_e}\left[h(x)\int_0^\infty n_e(\xi)\,\pi a^2\,d\xi - \int_0^\infty n_e(\xi)\,h(|x-\xi|)\,\pi a^2\,d\xi\right] - \frac{eDx}{kT_e}$$

Combining the integrals and non-dimensionalizing the variables yields the following compact form of the governing equation

$$\ln \tilde{n}_e = B\int_0^\infty \tilde{n}_e(\tilde{\xi})\,k(\tilde{x},\tilde{\xi})\,d\tilde{\xi} - A\tilde{x} \qquad (8)$$

where

$$\tilde{n}_e = \frac{n_e}{n_e^*}$$

$$\tilde{x} = \frac{x}{a}$$

$$\tilde{\xi} = \frac{\xi}{a}$$

$$A = \frac{eaD}{kT_e}$$

$$B = \frac{cen_e^*\,\pi a^2}{kT_e}$$

$$k(x,\xi) = h(\tilde{x}) - h(|\tilde{x} - \tilde{\xi}|) .$$

The dimensional constant c is associated with the choice of the kernel, $k(\tilde{x},\tilde{\xi})$. A and B are the non-dimensional parameters of the problem. We will discuss the physical significance of A and B after we have developed a solution to the non-dimensional problem.

To proceed with the analysis we must choose a kernel. For the present we ignore the grounded walls of the shock tube and consider a charged conducting disk surrounded by free space. This is a classical problem of electrostatics[31] which involves mixed boundary conditions. The potential at point $\tilde{x}$ on the axis of symmetry of a conducting disk (radius, a) located at point $\tilde{\xi}$ with a unit positive charge is

$$h(|\tilde{x} - \tilde{\xi}|) = \frac{e}{4\pi\, a\epsilon_0} \tan^{-1}\left(\frac{1}{|\tilde{x}-\tilde{\xi}|}\right)$$

For this case

$$k(\tilde{x},\tilde{\xi}) = \tan^{-1}\left(\frac{1}{\tilde{x}}\right) - \tan^{-1}\left(\frac{1}{|\tilde{x}-\tilde{\xi}|}\right) \qquad (9)$$

and

$$B = \frac{e^2\, n_e^*\, a^2}{4\epsilon_0\, kT_e}$$

The precursor number density profile is now determined by

$$\ln \tilde{n}_e = B \int_0^\infty \tilde{n}_e(\tilde{\xi}) \left[\tan^{-1}\left(\frac{1}{\tilde{x}}\right) - \tan^{-1}\left(\frac{1}{|\tilde{x}-\tilde{\xi}|}\right)\right] d\tilde{\xi} - A\tilde{x} \qquad (10)$$

We can sketch the solution of equation (10) by inspection. First consider the kernel (bracketed terms under the integral). The first term represents the ion contribution and the second term represents the electron contribution to the potential. Note that at $x = 0$ and small x that the ion term is greater than the electron term. But for large x the electron term dominates the ion term. The number density must always be positive and we expect it to be a decaying function of distance away from the origin. Thus for small values of x the integral will be positive, and negative for large values of x. Since the magnitude of both the kernel and the number density decay away from the origin, we expect that for very large x the integral term in equation (10) will be negligible compared to the other term in the equation. Hence, we expect an asymptotic solution for large x, i.e., $\ln \tilde{n}_e = -A\tilde{x}$. Figure 25 shows a sketch of the expected solution drawn in the $\ln \tilde{n}_e/A$ vs. $\tilde{x}$ plane.

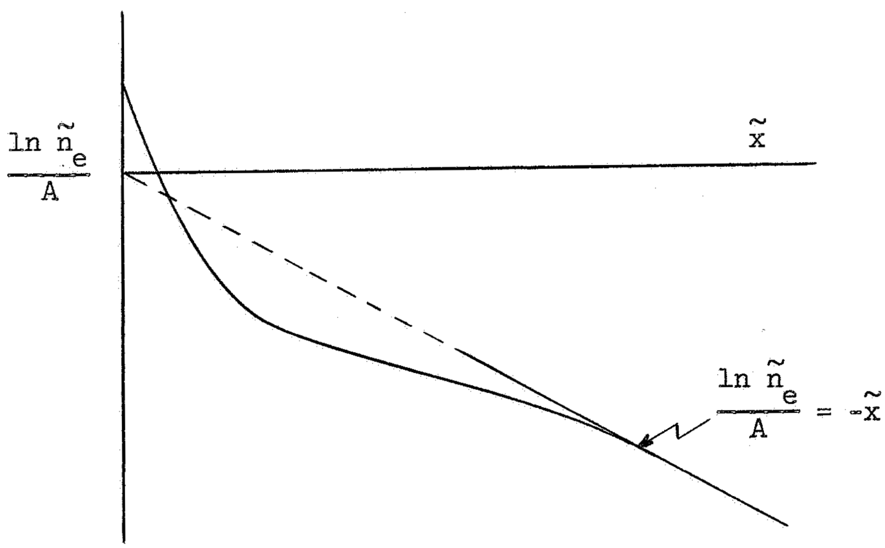

Fig. 25. Sketch of expected solution to eq. (10).

A numerical solution of equation (10) has been obtained for a range of parameters A and B. See Appendix D for a discussion of the numerical analysis of non-linear integral equations of the form shown in equation (8). Figures 26 and 27 show several results of the numerical calculation.

We note from these results that the solutions that yield a dipole like structure correspond to large values of A. Since the $\ln \tilde{n}_e/A$ vs. $\tilde{x}$ curves collapse very rapidly to the solution $\ln \tilde{n}_e/A = -\tilde{x}$ we can seek an analytic asymptotic solution.

By expanding the kernel

$$k(\tilde{x},\tilde{\xi}) = \tan^{-1}\left(\frac{1}{\tilde{x}}\right) - \tan^{-1}\left(\frac{1}{|\tilde{x}-\tilde{\xi}|}\right)$$

around $\tilde{x} = 0$ we can express the potential in terms of successive moments of the electron number density distribution ahead of the shock,

$$\frac{e\varphi}{kT_e} = \frac{B}{1+x^2}\int_0^\infty \tilde{\xi}\,\tilde{n}_e(\tilde{\xi})\,d\tilde{\xi} + \frac{Bx}{(1+\tilde{x}^2)}\int_0^\infty \tilde{\xi}^2\,\tilde{n}_e(\tilde{\xi})\,d\tilde{\xi} + \cdots$$

Now it is straightforward to obtain the potential for successive approximations of the distribution function. The first approximation is

$$\tilde{n}_e^{(1)} = \exp(-A\tilde{x})$$

$$\frac{e\varphi^{(1)}}{kT_e} = -\frac{B}{A^2}\left\{\frac{1}{1+\tilde{x}^2} + \frac{2\tilde{x}}{(1+\tilde{x}^2)^2} + \cdots\right\}$$

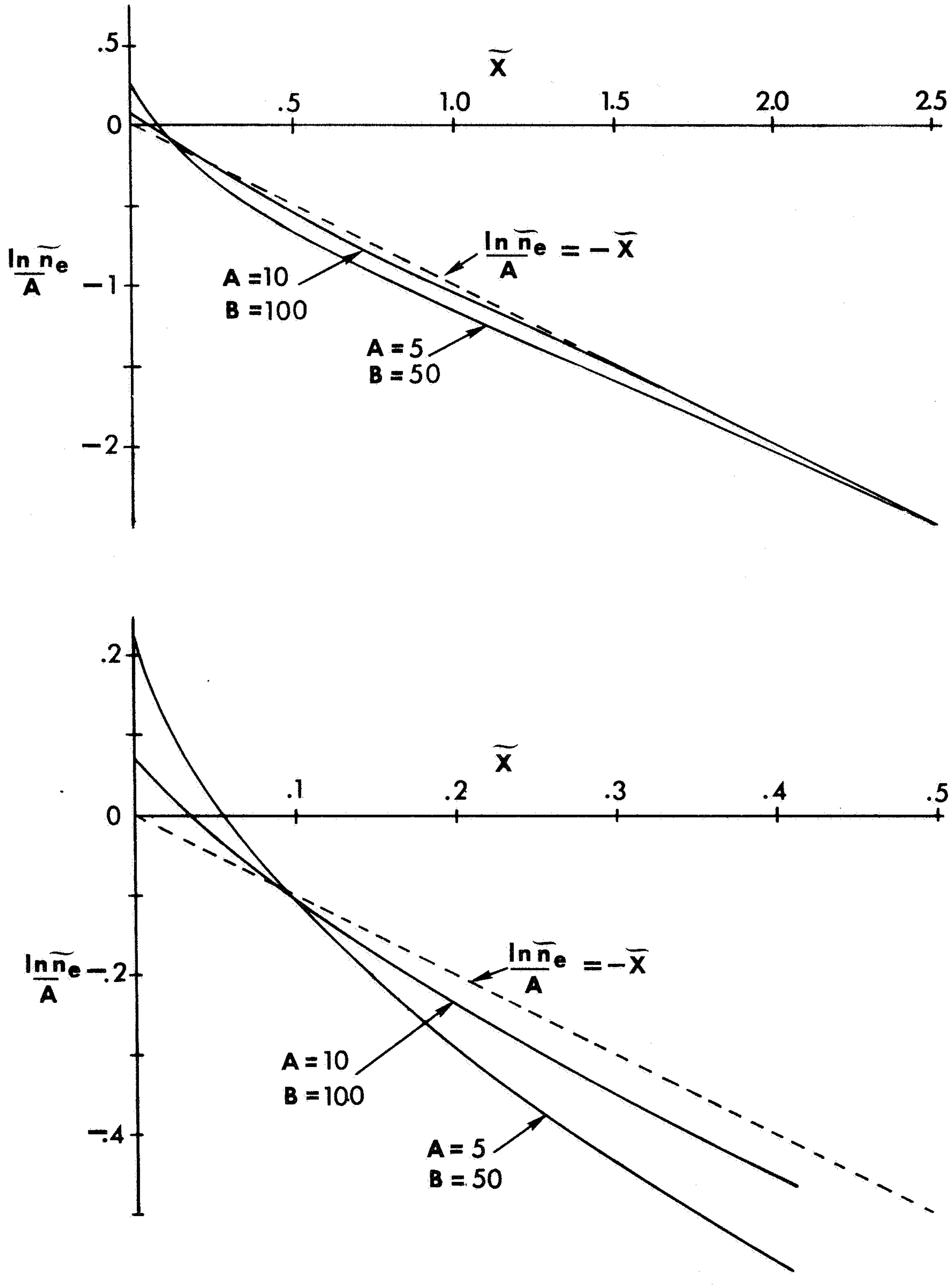

Fig. 26. Results from the numerical solution of equation (10).

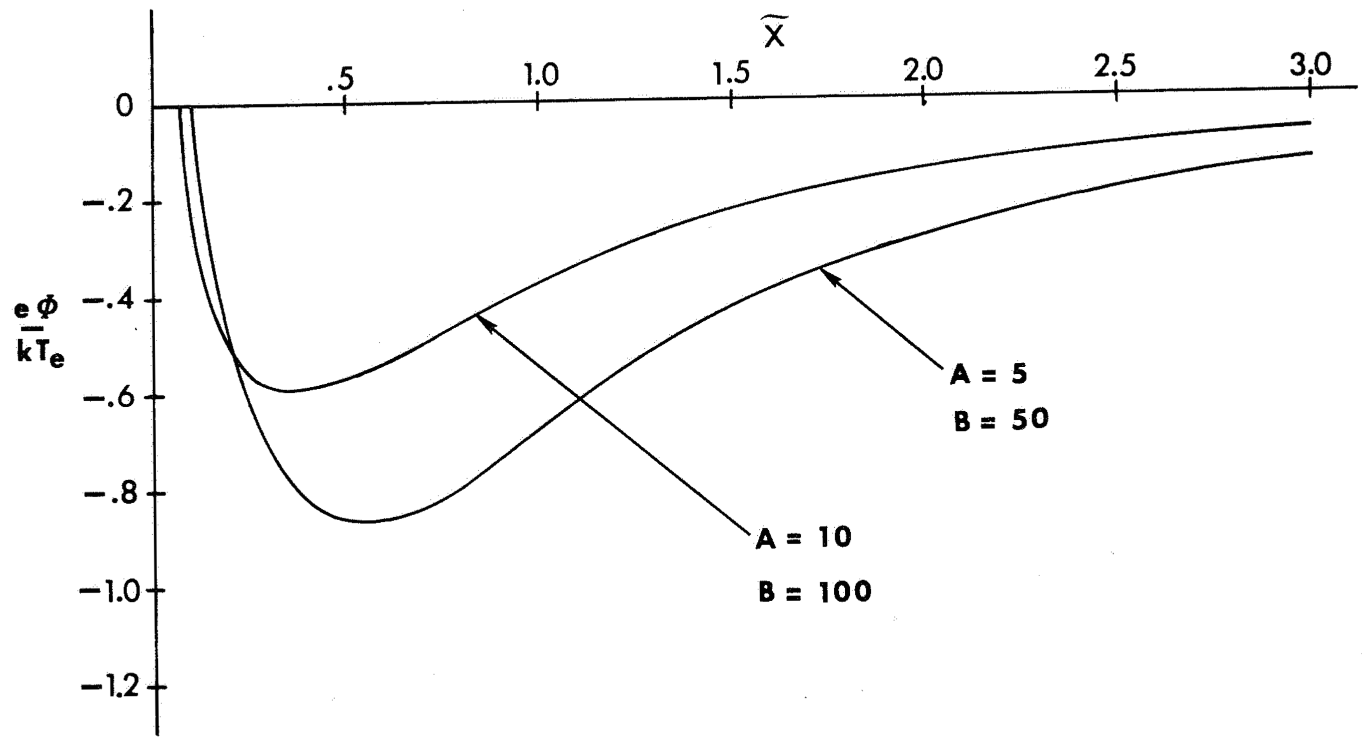

Fig. 27. Potential profiles corresponding to solutions shown in Fig. 26.

The next approximation is

$$\tilde{n}_e^{(2)} = \exp\left[-A\tilde{x} - \frac{B}{A} \left(\frac{1}{1+\tilde{x}^2} + \cdots \right) \right]$$

$$\frac{e\varphi^{(2)}}{kT_e} = -\frac{B}{A}\left(1 - \frac{B}{A}\right)\left(\frac{1}{1+\tilde{x}^2}\right)\left(1 + \frac{2\tilde{x}/A}{1+\tilde{x}^2}\right)$$

With this analytic asymptotic solution we can apply the computer to the detailed structure close to the shock. The two solutions can then be patched together. An example potential profile obtained in this fashion is shown in Fig. 28.

The solution shown in Fig. 28 presents several difficulties of interpretation. First the potential profile does not scale the same as the experimental profiles, it does not decay rapidly enough. This is presumably due to neglecting the grounded walls of the shock tube. Note from Fig. 28 that the value of $e\varphi/kT_e$ for this choice of parameters is approximately -.1. We know from the experimental data that φ is on the order of -1 volt. This means to match this theoretical potential profile to an experimental profile that the electron temperature has to be approximately 10 electron volts. This is an unreasonably high electron temperature. We also expect that the drag on the electrons ahead of the shock should not be too large. The value $A = 100$ suggests that the electron temperature should be very low if the drag is small.

We must view the analysis up to this point as preliminary and perhaps applicable to a glass shock tube. In the next section we will consider a kernel more applicable to the grounded metal-wall shock tube.

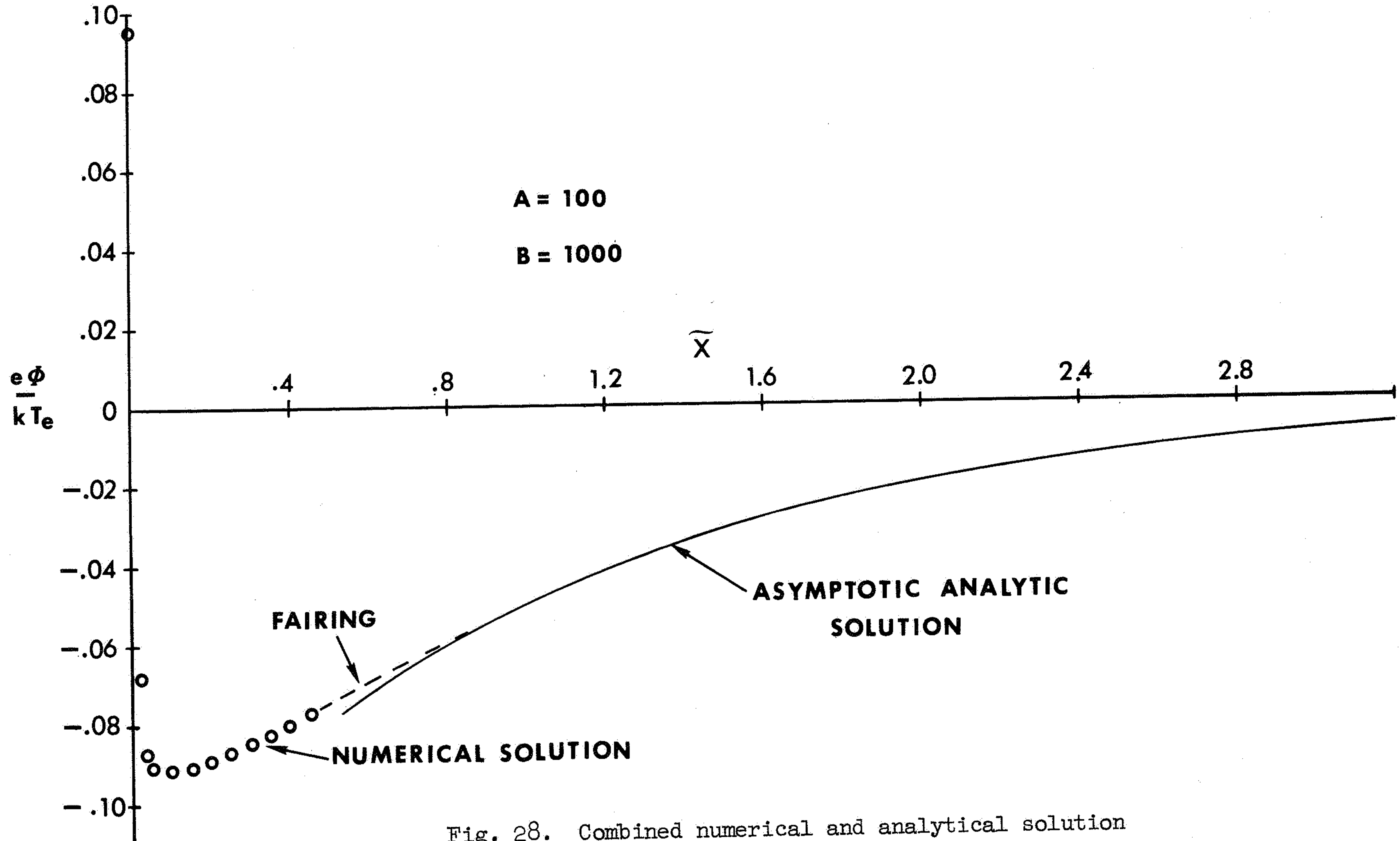

Fig. 28. Combined numerical and analytical solution to equation (10).

We will attempt to resolve the interpretation of the parameters by comparing the theory to our experimental results.

3.4. Equilibrium Centerline Precursor in a Grounded Shock Tube.

In order to improve the analysis developed in the above section we must use a kernel in equation (8) which reflects the presence of the grounded shock tube wall. Thus we must surround the conducting disk with a grounded cylinder. The potential along the axis of symmetry of a grounded cylinder of radius a due to a conducting disk located at $\tilde{x} = \tilde{\xi}$ with a unit positive charge is

$$h(|\tilde{x}-\tilde{\xi}|) = \sum_{n=1}^{\infty} \frac{e \exp(-k_n a |\tilde{x}-\tilde{\xi}|)}{2\pi \epsilon_0 a(\sum\limits_{m=1}^{\infty} \frac{1}{k_m a}) k_n a J_1(k_n a)}$$

where k_n's are defined by

$$J_0(k_n a) = 0$$

The analysis leading to this result is presented in Appendix E. Thus the kernel for the grounded shock tube case is

$$k(\tilde{x},\tilde{\xi}) = \sum_{n=1}^{\infty} \frac{\exp(-k_n a \tilde{x})}{k_n a J_1(k_n a)} - \sum_{n=1}^{\infty} \frac{\exp(-k_n a |\tilde{x}-\tilde{\xi}|)}{k_n a J_1(k_n a)} \tag{11}$$

and the parameter B becomes

$$B = \frac{e^2\, n_e^*\, a^2}{2\epsilon_0\, kT_e \sum\limits_{m=1}^{\infty} \frac{1}{k_m a}}$$

Substituting into equation (8) the governing equation for the precursor number density profile is

$$\ln \tilde{n}_e = B \int_0^{\infty} \tilde{n}_e(\tilde{\xi}) \sum_{n=1}^{\infty} \left[\frac{\exp(-k_n a\, \tilde{x}) - \exp(-k_n a\, |\tilde{x}-\tilde{\xi}|)}{k_n a\, J_1(k_n a)} \right] d\tilde{\xi} - A\tilde{x} \qquad (12)$$

Figures 29, 30, and 31 show several numerical solutions of equation (12). These solutions were obtained by the method described in Appendix D.

Figure 29 illustrates the role of parameter A in the solution. Parameter A affects both the amplitude and shape of the potential curve. For comparison to the experiment the influence on the shape of the potential is most important. Figure 30 examines the solution at A = 10 for several values of B. We see that at a particular value of the parameter A, parameter B affects the amplitude with very little influence on the shape of the potential. Figure 31 displays the electron number density profiles corresponding to the potential profiles in Fig. 30.

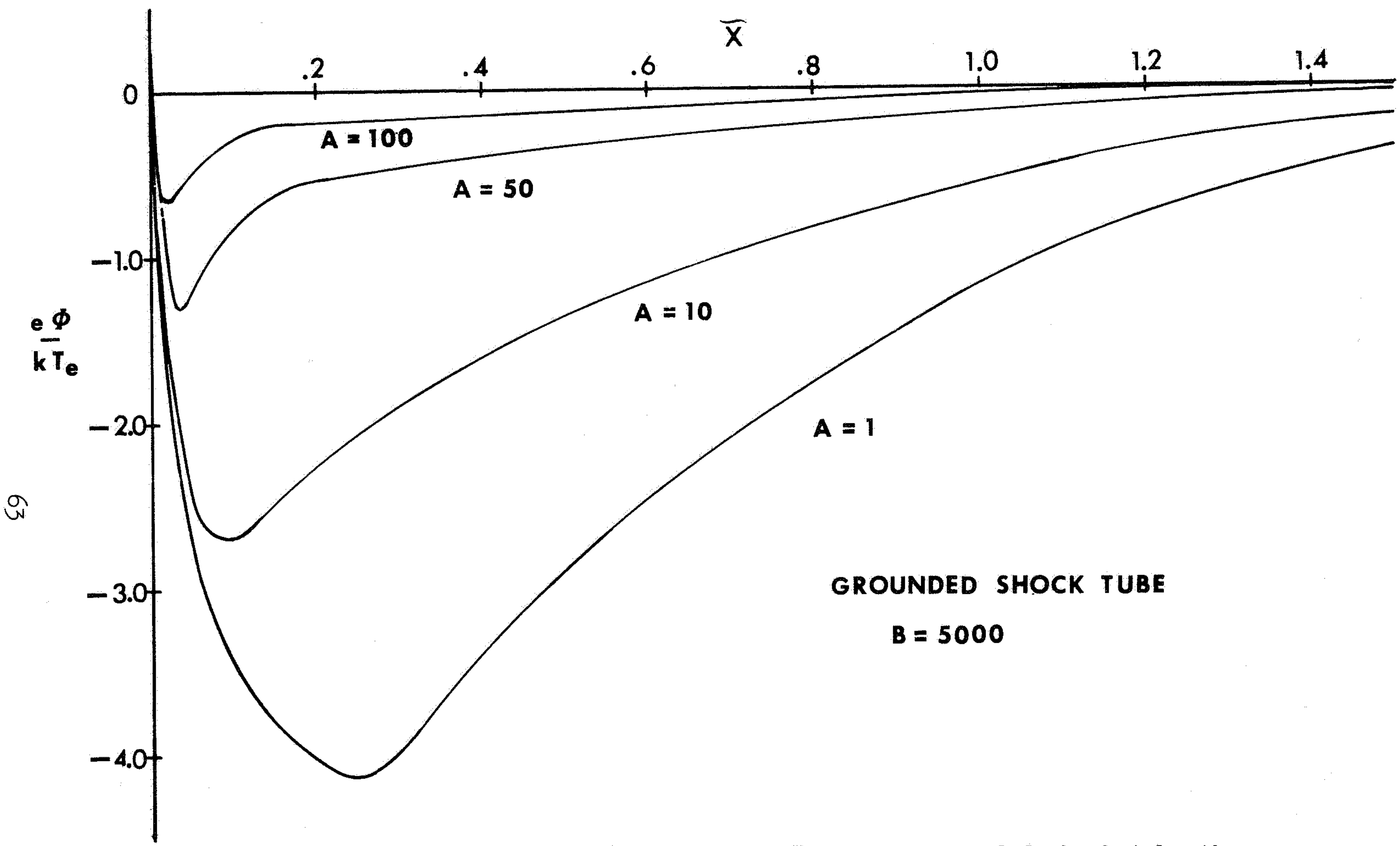

Fig. 29. Potential profiles for grounded-shock-tube theory for several values of parameter A.

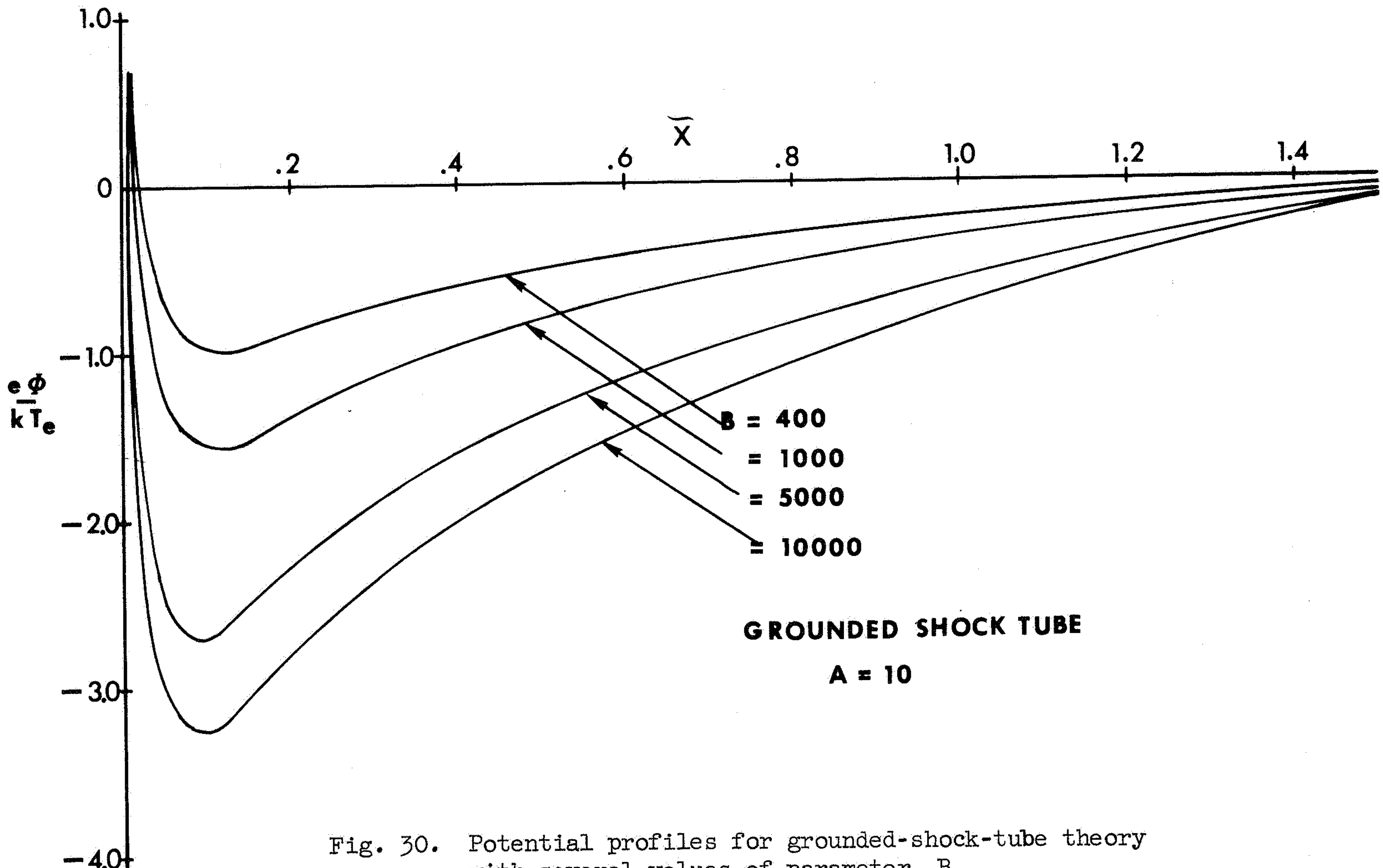

Fig. 30. Potential profiles for grounded-shock-tube theory with several values of parameter B.

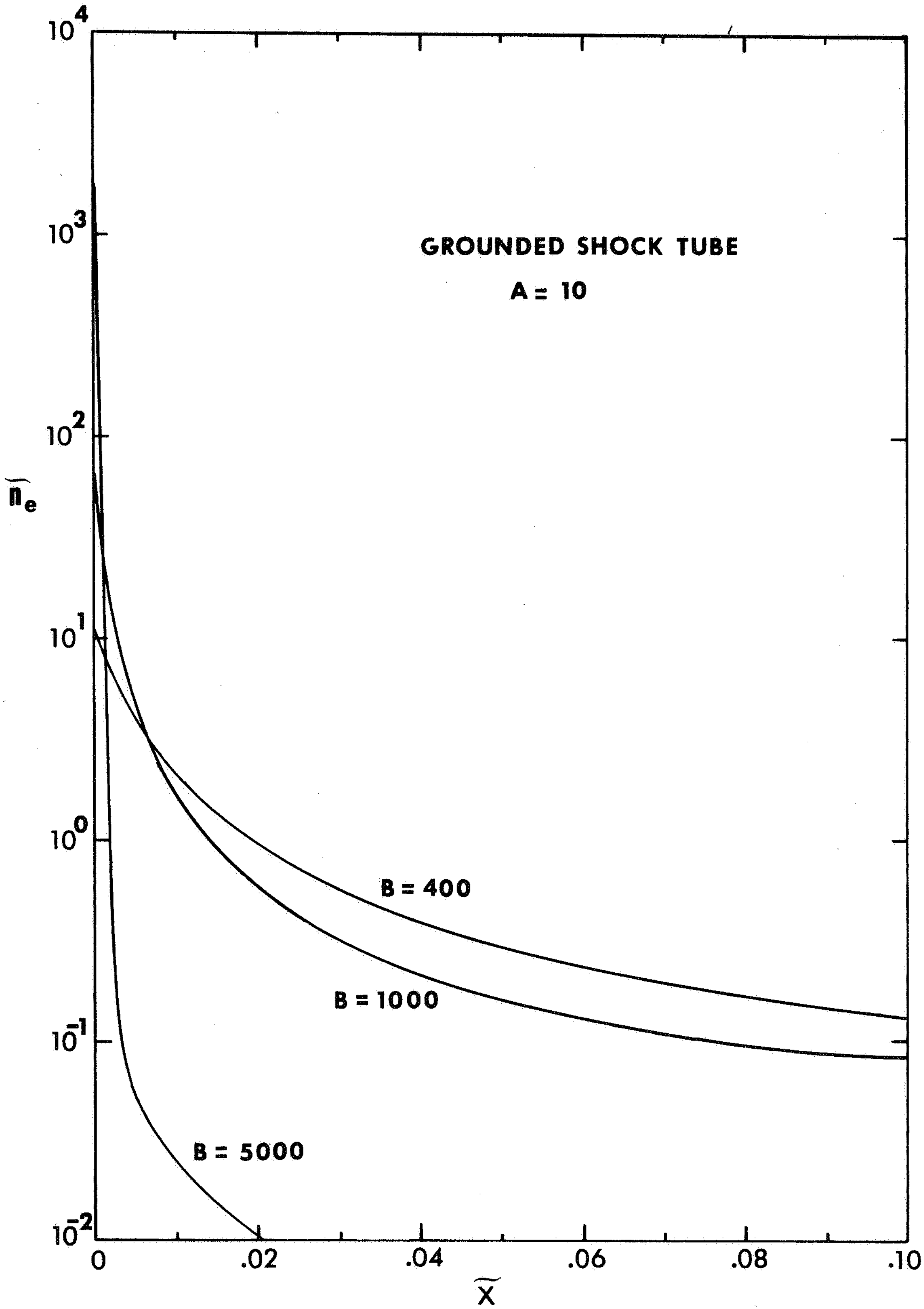

Fig. 31. Electron number density profiles corresponding to potential profiles shown in Fig. 30.

3.5. Parameters A and B.

Now that we have obtained solutions for the grounded shock tube in non-dimensional form, it is appropriate to discuss the non-dimensional parameters of the problem.

From above, the definitions of A and B are

$$A = \frac{eaD}{kT_e}$$

$$B = \frac{e^2 \, n_e^* \, a^2}{2 \sum_{m=1}^{\infty} \frac{1}{k_m a} \, \epsilon_0 \, kT_e}$$

We note that both A and B may be viewed as ratios to the electron thermal energy. A is the ratio of drag work to the electron thermal energy and B is the ratio of electrostatic energy to electron thermal energy. Parameter B may also be viewed as the ratio of the square of two lengths

$$B = \frac{1}{2 \sum_{m=1}^{\infty} \frac{1}{k_m a}} \frac{a^2}{h^2}$$

where

$$h = \sqrt{\frac{\epsilon_0 \, kT_e}{e^2 \, n_e^*}} \equiv \text{Debye length}$$

$$\sum_{m=1}^{\infty} \frac{1}{k_m a} \simeq 1.4$$

Thus

$$B = .36 \frac{a^2}{h^2}$$

We can at this point establish some rough guidelines on A and B for purposes of comparing theory and experiment. It is reasonable to expect a fairly low electron temperature particularly if the electron source at the translational shock is a collisional process. This follows from assuming that the energy involved in the collisional process does not exceed by very much the ionization energy of the atom or molecule being ionized. With this in mind we expect a large value of B due to the smallness of the Debye length with respect to the shock tube radius. Since the energy transfer between electrons and neutral particles is very small we should expect a small drag force, thus a relatively small value of the parameter A.

We can also establish upper bounds on the electron temperature and number density. We assume the electron temperature cannot exceed the frozen temperature behind the shock wave and the electron number density cannot exceed the equilibrium number density. We expect that both these quantities should not be even close to the above limits.

3.6. Comparison Between Theory and Experiment.

Our experimental data consists of the shape and magnitude of the electrostatic-potential profile ahead of the shock wave for various Mach numbers and initial pressures. The theory for the low Mach number precursor developed in the past several sections of this chapter involves an unknown electron temperature and number density. We are faced with the fact that our experimental data is not sufficient to determine all the unknowns in the problem. The best we can do with the information at hand is choose a range of parameters which fit the data and examine the physical consequences of our choice.

In Section 3.4 we presented parametric solutions for the theoretical potential profiles ahead of the shock wave. The $A = 10$ solutions have the same shape as the experimental results. Figure 32a shows a typical experiment compared to the theoretical profiles for $A = 10$ and $B = 400$, 1000, 5000, and 10,000, Note for this comparison we have matched the theoretical and experimental minimum potential points. This figure shows that $A = 10$, $B = 1000$ and $B = 5000$ results give near perfect agreement and that $A = 10$, $B = 400$ and $B = 10{,}000$ are not far off. The electron temperature corresponding to $A = 10$ and the above B values is shown in Fig. 32b. The frozen gas temperature for this experiment is shown as a dashed line in Fig. 32b. We conclude from this comparison that the choice $A = 10$ and $B = 5000$ is reasonable for this typical experiment.

We have found that the range $A = 8$ to 14 fits all the experimental data as far as the shape is concerned. Figure 33 shows the

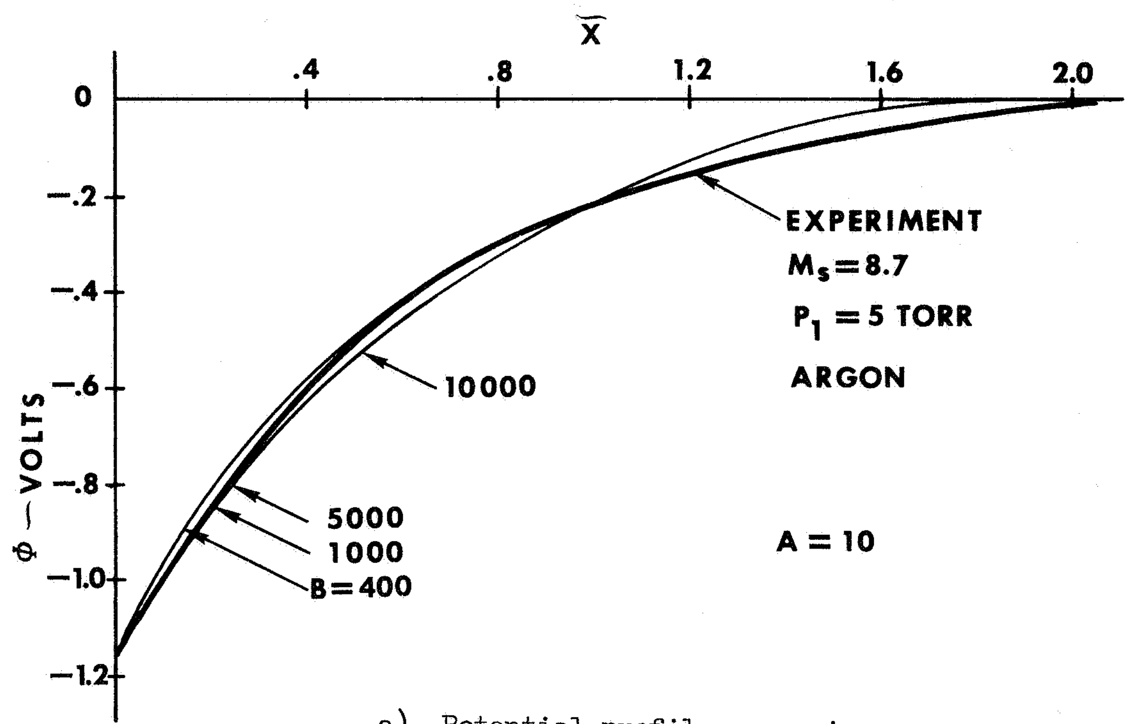

a) Potential profile comparison.

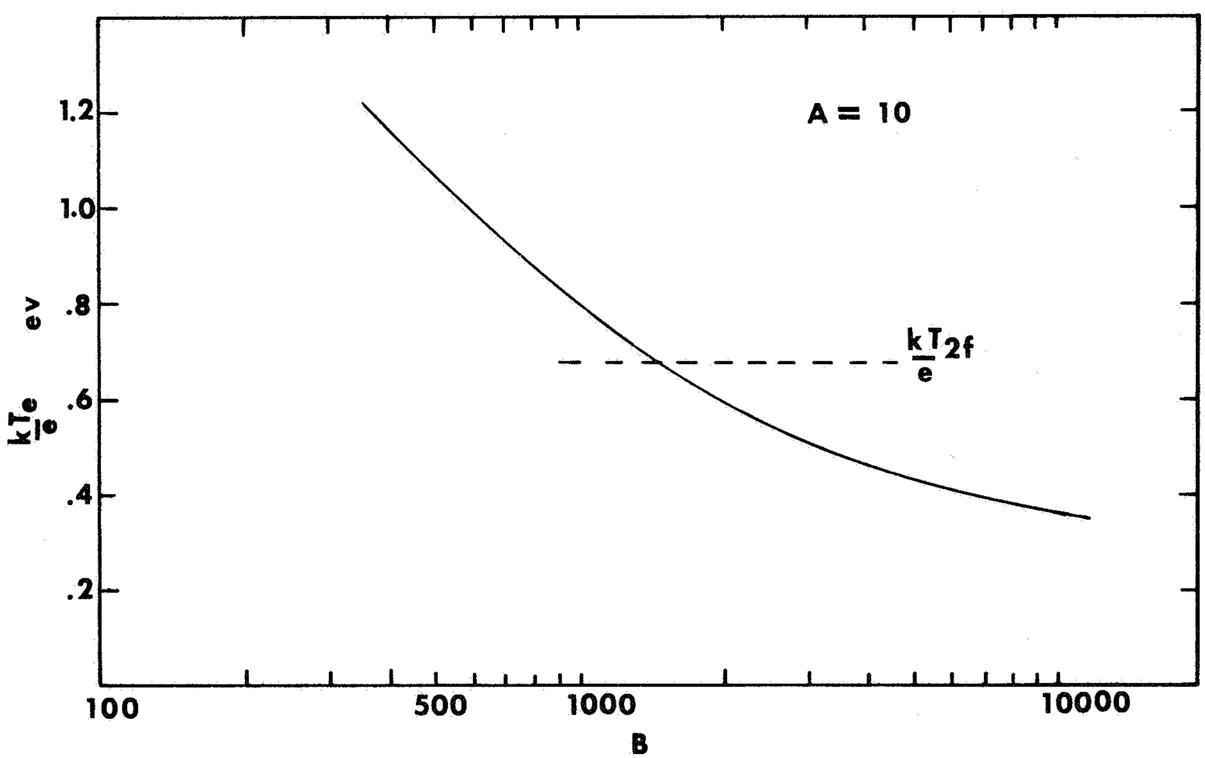

b) Resulting electron temperature.

Fig. 32. Comparison between theory and experiment.

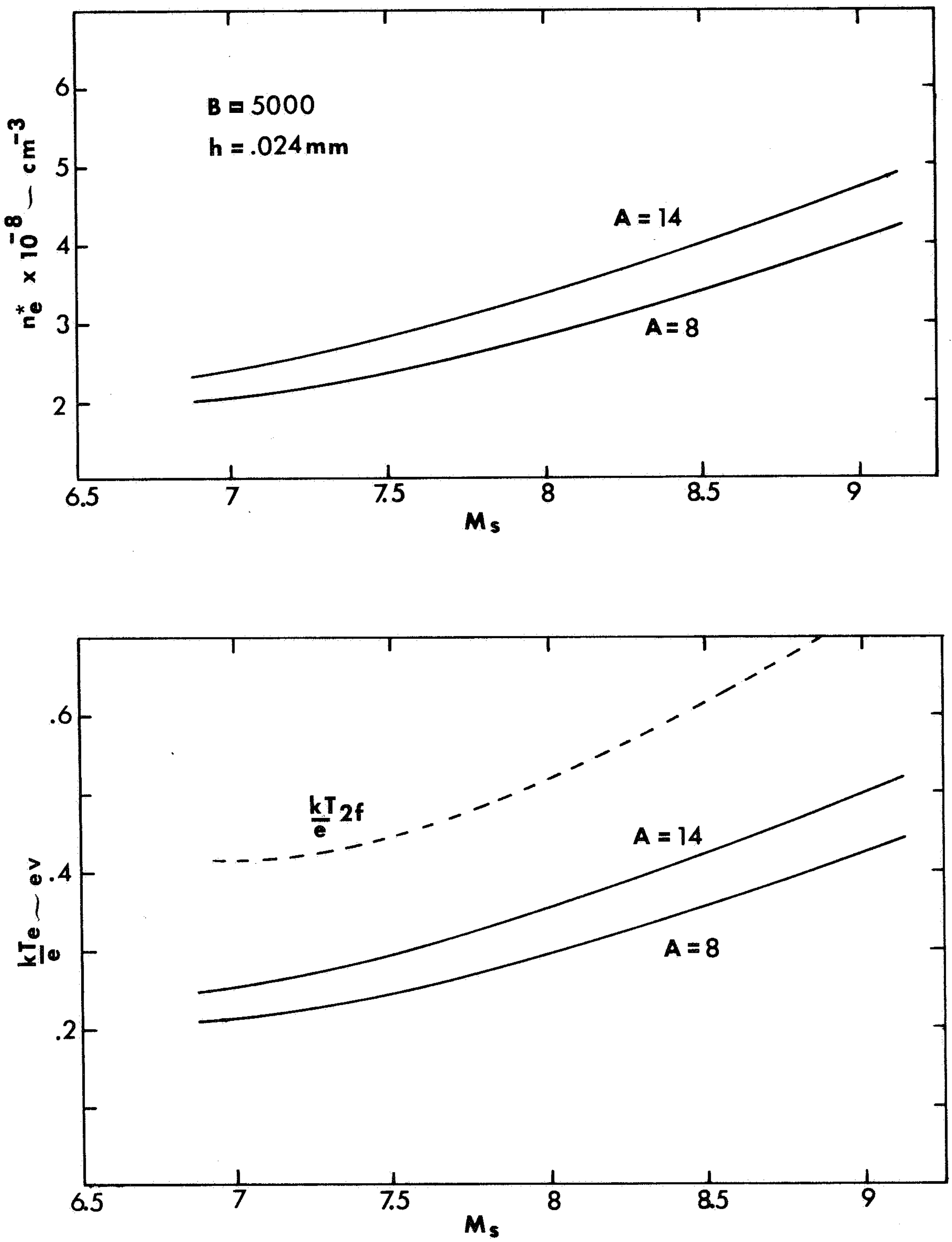

Fig. 33. Electron temperature and characteristic number density as functions of shock Mach number.

electron temperature, T_e, and the characteristic number density, n_e^*, as functions of Mach number for $B = 5000$. It should be noted that this is not a unique value for B. As in Fig. 32 this value of B is a reasonable choice.

Now that a model for the low Mach-number precursor in argon has been established, it is appropriate to examine the validity of our potential measurement. The reader should recall from Chapter 2 that the mesh-electrode data was read from the potential minimum exhibited on the "local" data traces. The data can be taken as quantitatively correct if the electron cloud ahead of the translational shock does not interfere with the mesh electrode. Note from Fig. 30 that the potential minimum for $A = 10$ and $B = 5000$ is roughly one tenth of a shock tube radius away from the origin. Figure 31 shows that for $A = 10$ and $B = 5000$ the electron cloud is concentrated within the distance 0.01 of a shock tube radius. Thus the equilibrium model presented above predicts a potential profile ahead of the shock in terms of a charge distribution which does not interfere with the experimental determination of the potential.

Recall that we assumed the positive charge was distributed radially on a conducting disk located at $x = 0$ (translational shock front) in the theory. Since the theoretical electron distribution corresponding to a low electron temperature has a very small spatial extent, we must test the assumed location of the positive charge. Calculations have been performed with the ions shifted back from the origin. We find that the potential profile ahead of the shock is insensitive to small changes in the location of the ions. However, quantities at the origin $x = 0$ are very sensitive, particularly the non-dimensional number density. For example, shifting the positive charge back .01 non-dimensional unit reduces the non-dimensional number density two orders of magnitude.

3.7. The Drag Force and Electron Energy Considerations.

Up to this point we have not postulated a detailed model of the electron-neutral collisions which produce drag on the precursor electrons. It is important to examine this mechanism since the drag force, through the parameter A, plays a significant role in matching the theory to the experiment.

Recall that the model developed in this chapter assumed a steady equilibrium electron distribution in shock fixed coordinates. In the shock fixed coordinates we view the test gas at room temperature and p_1, as a uniform flow into the shock wave at velocity $-u_s$. The quantity D in the original formulation and in parameter A is the drag force per electron charge due to collisions with the incoming neutral test-gas atoms.

The simplest possible model for the electron-neutral collisions is the hard sphere model. The average momentum transfered to a stationary electron from a neutral atom moving at the shock speed is

$$m_e u_s .$$

The quantity D for this simple picture is

$$D = \frac{m_e u_s \bar{\nu}}{e}$$

where $\bar{\nu}$ is an average collision frequency which depends on the test gas number density and temperature and the electron temperature. The parameter A then becomes

$$A = \frac{a\, m_e u_s \bar{\nu}}{kT_e}$$

Figure 34 shows the average collision frequency as a function of Mach number for A and T_e shown in Fig. 33.

The equilibrium precursor model proposed in this thesis assumes that the electrons are thermalized at a particular temperature. The model assumes that this temperature does not change significantly in the time that it takes the shock wave to travel one to two shock tube radii (i.e., the scale of precursor potential). It was not necessary in the formulation of the model to say whether the electron cloud ahead of the shock consists of the same electrons for all time or that the electrons are lost to the flow behind the shock and replenished by new ones at the proper temperature.

To gain some insight into this aspect we now examine the heating of the electrons by the drag force. This amounts to examining the energy exchange during the electron-neutral collisions. If we view the electron cloud as a closed system then the electron thermal energy change due to a collision with a neutral atom is

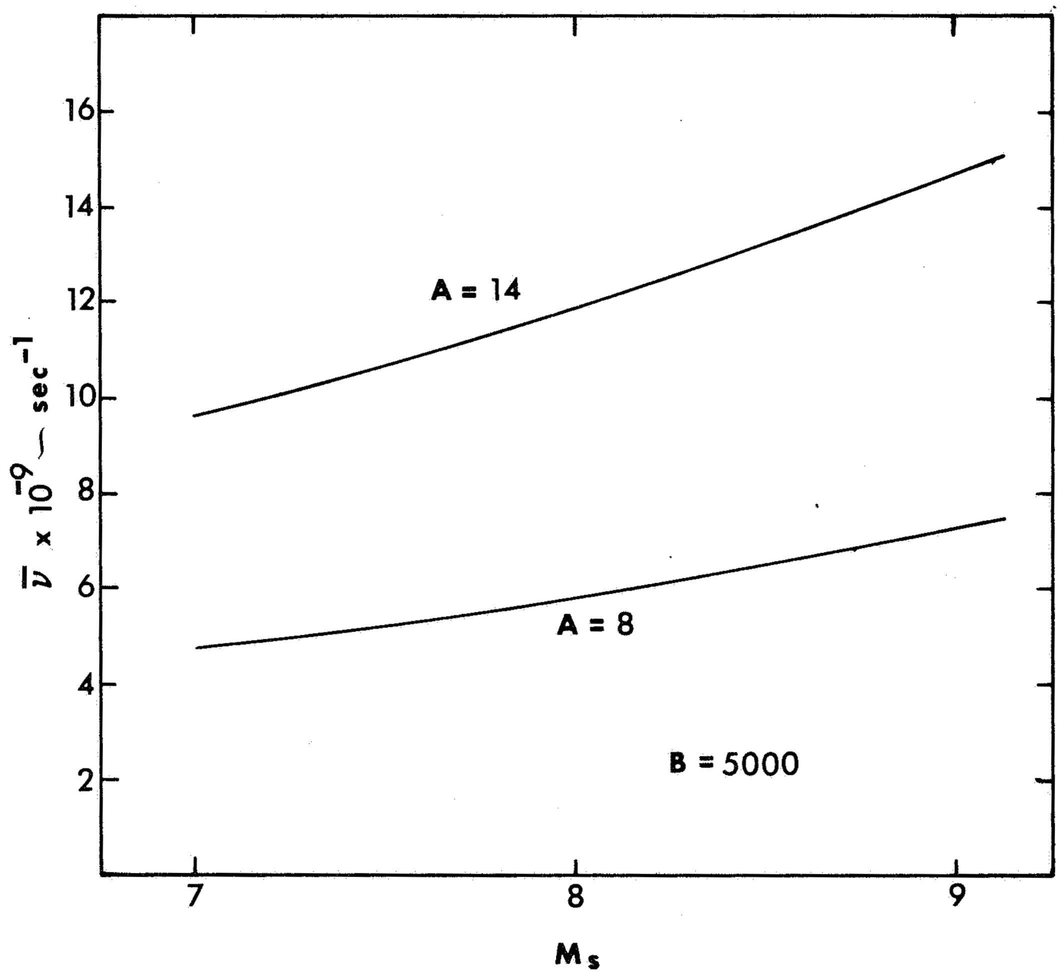

Fig. 34. Electron-neutral collision frequency as a function of shock Mach number.

$$\Delta\, kT_e = \frac{2}{3}\, m_e\, u_s^2$$

Thus the energy gained by an electron per unit time is

$$\frac{\Delta\, kT_e}{\Delta t} = \frac{2}{3}\, m_e\, u_s^2\, \bar{\nu}$$

The fractional thermal energy gained by an electron in the time the shock wave travels one shock-tube radius is given by

$$\frac{\Delta\, kT_e}{kT_e} = \frac{2}{3}\, \frac{m_e\, u_s\, \bar{\nu}\, a}{kT_e} = \frac{2}{3}\, A \approx 6$$

This heating is not tolerable in view of our assumptions unless a loss mechanism is available.

Several researchers[2,5] have observed continuum radiation at the translational shock front in monatomic gases. This radiation is usually assumed to be due to impurity components in the test gas. It seems that Bremsstrahlung radiation from the precursor electrons experiencing collisions may be a source for this radiation as well as the loss mechanism for the energy gained through collisions. Zel'dovich and Raizer[32] treat the problem of Bremsstrahlung radiation from electrons experiencing impulsive accelerations. We find that less than one percent of the energy gain indicated above can be accounted for in this manner. Thus we must assume for the present model that the heated electrons in the precursor cloud are being constantly carried downstream into the shocked-gas relaxation zone and being replenished with freshly generated low temperature ones.

3.8. Comparison Between Metal Shock Tube and Glass Shock Tube Low Mach Number Precursor Theories.

Recall that in Section 3.3 above we solved for the precursor-potential profile neglecting the presence of grounded shock tube walls. We mentioned in that section that this "unbound" solution may correspond to a glass shock tube. Now that we have determined reasonable values for parameters A and B for the grounded shock tube case it is appropriate to present a comparison between the grounded walls case and the ungrounded walls case. Figure 35 shows such a comparison for $A = 10$ and $B = 1000$. We note that the difference in shape and extent of the precursor potential agrees qualitatively with the difference observed by Hollyer (see Figure 39 in Appendix A).

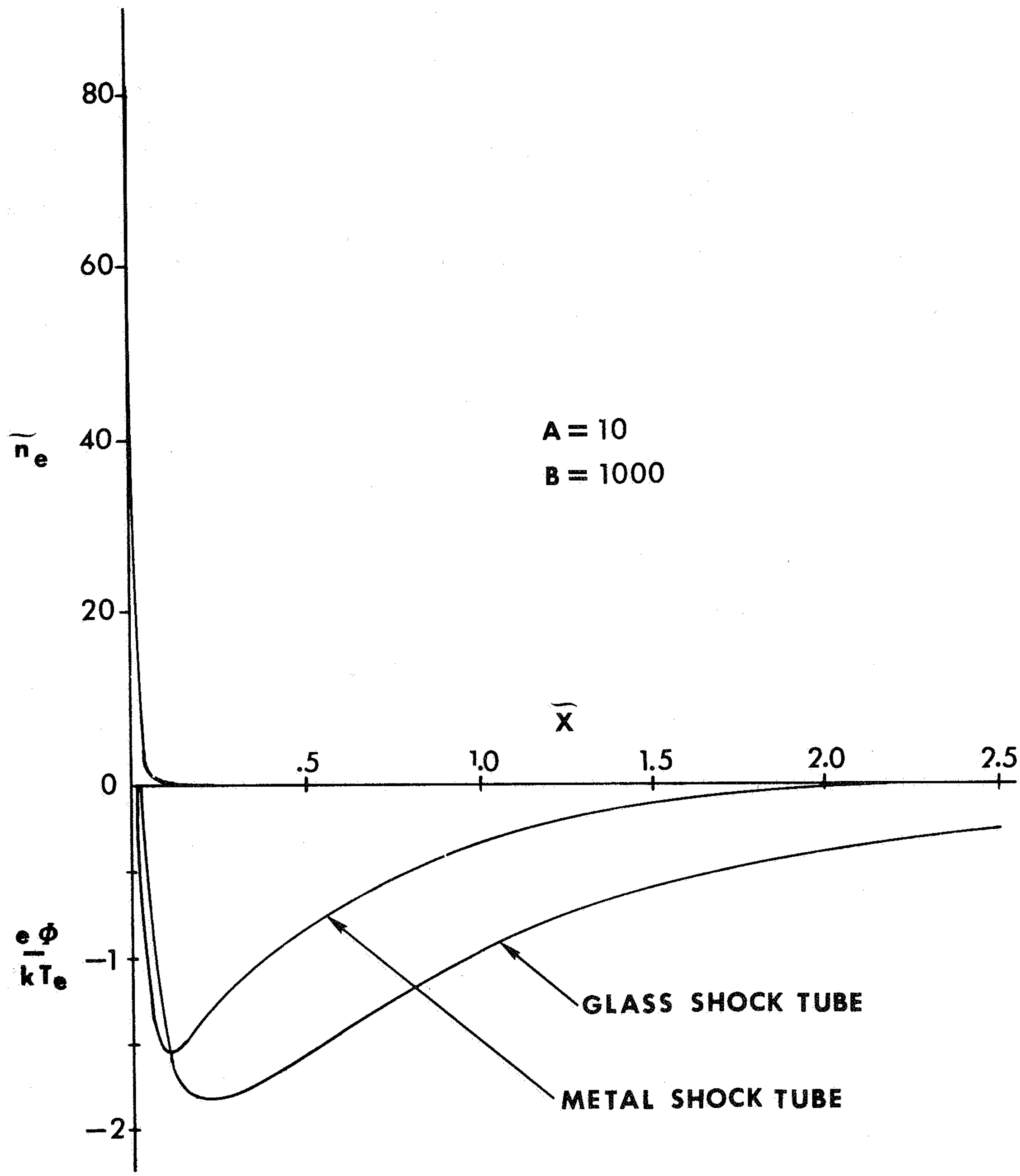

Fig. 35. Comparison between metal and glass shock shock-tube precursor potential profiles.

4. CONCLUDING REMARKS

In the first section of this chapter we summarize the low Mach number study and results. In the next section we comment on the theoretical analysis of the higher Mach number experimental results. The last section is devoted to the writer's perspective on the subject of precursors.

4.1. Argon Low Mach-Number Precursor Study, Summary and Conclusions.

We observed a negative potential profile ahead of argon shock waves in the Mach number range 6.5 to 9.0. These signals were smooth, started negative at the translational shock front, and decayed to zero approximately 1 to 2 shock tube radii ahead of the shock front. Simple electrostatic ideas were used to lend credence to the postulate that these signals are due to small scale electron diffusion resulting in a dipole-type structure at the shock front.

An elementary gas dynamic model for the electron distribution ahead of the translational shock wave was formulated. We assumed that the electron distribution and resulting electrostatic field was independent of time for the time interval required for the shock to travel 1 to 2 shock-tube radii. An axial force balance for the electrons on the centerline of the shock tube composed of the electron pressure gradient, the electrostatic forces due to charge separation, and frictional force due to electron-neutral collisions ahead of the shock wave was formulated. This formulation leads to a first order linear ordinary differential equation with two unknowns, the electron number density and the electrostatic potential. This model was coupled to an approximate three-dimensional model of the electrostatic field. The combined electrostatic-gas dynamic model evolved as a non-linear integral equation for the electron number density profile ahead of the shock wave on the centerline of the shock tube. The kernel of this integral equation depended on the choice of electrostatic boundary conditions. Two cases were treated, first the grounded walls of the shock tube were ignored. A combined analytical and numerical solution of the non-linear integral equation demonstrated that the grounded walls must be considered in order to compare the theory to the experiment. The second case included the effect of grounded shock tube walls. Parametric numerical solutions for this case were presented.

It was pointed out in the main text that the experimental potential profile is not sufficient to determine all the unknowns in the theoretical model. Thus we presented a range of theoretical results which agree with the experimental data. The range of theoretical results is not so large as to make them useless. The results are also physically reasonable. The precursor electron temperature turned out to be roughly half the frozen gas temperature behind the translational shock (which is just slightly higher than the final equilibrium temperature for these low shock Mach numbers). The characteristic number density (i.e., number density at the point where $e\varphi(\tilde{x})/kT_e = eD\tilde{x}/kT_e$)

turned out to be on the order of $10^8/cm^3$ which is three to four orders of magnitude below the final equilibrium number density. Of course the relatively low electron temperature and number density yields a very small Debye length. The drag force on the precursor electrons was found to be an important source of heated electrons in the relaxation zone behind the translational shock wave.

4.2. High Mach Number Shock-Tube Precursor Analysis.

Theoretical consideration of the high Mach number precursor data presented in Chapter 2 has not been attempted at this time. However, we present some conjectures and observations which may be useful in the future. Recall the intermediate, Type II, results where the potential profile changes shape, increases in amplitude, and decreases in spatial extent. Since photoionization was not in evidence, i.e., we found no positive ions with the biased electrode, we suggest that the Type II result is an evolution of the electrostatic precursor postulated in Chapter 3. The general behavior of the amplitude and shape of the potential profile can be attained by increasing both parameter A and parameter B. The flattening of the profile very close to the shock could be due to either photoemission from the electrode surface or the presence of a thin layer of photoionized gas.

An interesting parallel to the present work on the low Mach number diffusion aspects of the precursor, where emphasis has been placed on the three-dimensional nature of the electrostatic fields, has been pursued for photoionization precursors. Wetzel[20] has investigated a one-dimensional photoionization model which considers the shock wave as a plane radiation source. Dobbins[33] has recently refined the radiation absorption considerations and included the three-dimensional nature of the radiation field. This is a definitive step toward understanding photoionization precursors in shock tubes. We submit that this type model should be combined with the electrostatic field resulting from diffusion at the shock front. Hopefully a model of this sort would predict the decay of the electrostatic field ahead of the shock wave and the build-up of a large scale (large compared to the diffusion scale) charge distribution ahead of the shock wave.

4.3. Perspective of Shock-Tube Precursors.

In Section 2.6 above we presented a summary of our experimental results and qualitative conclusions. To reiterate these results we note that our experiments together with our low-Mach-number theoretical considerations indicate that small scale electron diffusion, photoemission from the shock tube interior, and photoionization of the test gas or impurity gases all play a role in shock-tube precursor phenomena.

Precursor experiments to date, including the one reported here, have not determined the source of electrons for diffusion in the vicinity of the shock front or the species which are photoionized ahead of the shock. Both these questions may be answered in terms of impurities and/or the test gas. Photoemission from the interior of the shock tube is clearly a "noise" phenomenon, i.e., an inadequacy of our laboratory facilities for the study of shock waves into quiescent gases.

We submit that the subject of conventional shock-tube precursors should be divided into two categories: 1) electrostatic potential precursors due to small scale electron diffusion in the vicinity of the shock wave, and 2) small scale electron diffusion coupled with photoionization ahead of the shock wave. It remains to be seen whether precursors are a feature of shock wave structure or whether they are only associated with shock-tube production of strong shock waves. The problem of photoemission we know is associated with the facility and must be dealt with or adequately accounted for in shock tube experiments.

REFERENCES

1. Hollyer, R. N., "Preliminary Studies in the APL High Temperature Shock Tube", Johns Hopkins University Applied Physics Laboratory CM-903, May 1957.

2. Petschek, H. and Byron, S., "Approach to Equilibrium Ionization Behind Strong Shock Waves in Argon", Annals of Physics, 1, 270-315, 1957.

3. Lin, S. C., Resler, E. L., and Kantrowitz, A., "Electrical Conductivity of Highly Ionized Argon Produced by Shock Waves", J. Applied Physics, 26, 1, 95-109, 1955.

4. Groenig, H., "Measurements of the Diffusion of Electrons Out of Strong Shock Waves", Institut fuer Mechanik, Technical University, Aachen, Germany (Final Report on Contract AF 61(514)-1046), June 1959.

5. Gloersen, P., "Precursor Signals from Shock Waves in Xenon", Bulletin of American Physical Soc., Ser. II, 4, 283, 1959.

6. Gloersen, P., "Some Unexpected Results of Shock-Heating Xenon", Physics of Fluids, 3, 6, 857-870, 1960.

7. Weymann, H. D., "Electron Diffusion Ahead of Shock Waves in Argon", Physics of Fluids, 3, 4, 545-548, 1960.

8. Weymann, H. D. and Troy, B., "Electron and Ion Density Profiles Ahead of Shock Waves in Argon", Bulletin of American Physical Soc., 6, 212, 1961.

9. Holmes, L. B., "Plasma Density Ahead of Pressure Driven Shock Waves", University of Rochester Technical Note No. 1, May, 1965.

10. Weymann, H. D. Holmes, L. B., "Plasma Density Ahead of Pressure-Driven Shock Waves", Bulletin American Physcial Society, 10, 1143, 1965.

11. Lederman, S. and Wilson, D. S., "Microwave Resonant Cavity Measurement of Shock Produced Electron Precursors", AIAA J., 5, 1, 70-77, 1967.

12. Wetzel, L., "Precursor Effects and Electron Diffusion from a Shock Front", Physics of Fluids, 5, 7, 824-830, 1962.

13. Pipkin, A. C., "Precursor Waves in Shock Tubes", Physics of Fluids, 6, 10, 1382-1388, 1963.

14. Appleton, J. P., "Electrical Precursors of Ionizing Shock Waves", Physics of Fluids, 9, 2, 336-342, 1966.

15. Pipkin, A. C., "Diffusion from a Slightly Ionized Region in a Uniform Flow", Physics of Fluids, 4, 10, 1298-1302, 1961.

16. Weymann, H. D., "On the Mechanism of Thermal Ionization Behind Strong Shock Waves", University of Maryland Technical Note BN-144, July 1958.

17. Ong. R. S. B. and Turcotte, D. L., "On the Struture of Ionization Fronts", American Physical Society Meeting, Nov. 1967.

18. Bond, J. W., Watson, K. M., and Welch, J. A., "Atomic Theory of Gasdynamics", Addison-Wesley, Massachusetts, 1965.

19. Ferrari, J. H. and Ferrari, C., "Gas Dynamics with Nonequilibrium Radiative and Collisional Ionization", Physics of Fluids, 8, 12, 2121-2139, 1965.

20. Wetzel, L., "Far-Flow Approximations for Precursor Ionization Profiles", AIAA J., 2, 7, 1208-1214, 1964.

21. Chapin, C. E., "Nonequilibrium Radiation and Ionization in Shock Waves", Purdue University AA & ES 67-9, June, 1967.

22. Bradley, J. N., "Shock Waves in Chemistry and Physics", John Wiley and Sons, Inc., New York, 1962.

23. Klein, A. F., "1. The Use of a Large Conventional Shock Tube as a Pre-ionizer for an Inverse Pinch Shock Tube, 2. The Application of Thin-Film Heat Transfer Gauges and Flush Electrostatic Probes to Partially Ionized Flows in Shock Tubes", Ph.D. Thesis, California Institute of Technology, 1967.

24. Baganoff, D., "Pressure Gauge Instrumentation for Studdies in Ionized Gases", Stanford University SUDARR No. 315, June, 1967.

25. Smith, J. A., "An Experimental Investigation of the Structure of Reflecting, Ionizing Shocks in Xenon", Ph.D. Thesis, California Institute of Technology, 1967.

26. Turner, E. B., "Plasma Diagnostic Techniques--Chapter 7, Optical and Ultraviolet Techniques", edited by R. H. Huddlestone and S. L. Leonard, Academic Press, New York, 1965.

27. Glass, I. I. and Hall, J. G., "Handbook of Supersonic Aerodynamics--Section 18 Shock Tubes", NAVORD Report 1488 (Vol. 6), Dec. 1959.

28. Corning Glass Works, Product Information Bulletin IC-31, July, 1961.

29. Samson, J. A. R., "Techniques of Vacuum Ultraviolet Spectroscopy", John Wiley and Sons, Inc., New York, 1967.

30. Wong, H. and Bershader, D., "Thermal Equilibration Behind an Ionizing Shock", J. Fluid Mech., 26, 459-479, 1966.

31. Jackson, J. D., "Classical Electrodynamics", John Wiley and Sons, Inc., New York, 1962.

32. Zel'dovich, Ya. B. and Raizer. Yu. P., "Physics of Shock Waves and High-Temperature Hydordynamic Phenomena", Academic Press, New York, 1966.

33. Dobbins, R. A., "Photoexcitation and Photoionization of Argon Ahead of a Strong Shock Wave", AIAA Paper No. 66-666, 1968.

34. Grosse, F. A. and Smith, W. R., "Vapor Condensation in a Shock Tube--Electrostatic Effects", Physics of Fluids, 11, 4, 835, 1968.

35. Duff, R. E., Long, J. R. and Porter, J. R., "Time Interval Multiplier for Shock Tube Studies", Rev. of Scientific Instr., 39, 7, 976, 1968.

36. Scarborough, J. B., "Numerical Mathematical Analysis", fifth edition, Johns Hopkins Press, Baltimore, 1962.

37. Langmuir, R. V., "Electromagnetic Fields and Waves", McGraw-Hill Book Company, Inc., New York, 1961.

APPENDIX A

REVIEW OF SHOCK TUBE PRECURSOR LITERATURE

The following paragraphs are devoted to a review of experimental and theoretical work on shock-tube precursors reported to date. Data, comments, and results are freely reproduced from the references to avoid any misconceived interpretations of the work. We first consider the experimental work in chronological order of publication. We then consider the theoretical work by groups which logically fit together according to the approach to the problem.

A.1. <u>Previous Shock Tube Precursor Experiments.</u>

Hollyer,[1] in the course of developing a new shock tube facility, observed charged particles ahead of shock waves in monatomic gases. The shock tube consisted of a seamless cold-drawn steel driven section. The driven section was eight feet long with a two inch inside diameter. Test sections (length not specified) were added to the driven section. Shock waves were produced with high pressure helium and hydrogen.

Figure 36 shows a sketch of the two probes used for the precursor measurements. The primary investigation was carried out at $M_s = 9$ in argon with $p_1 \leq 1$ Torr.

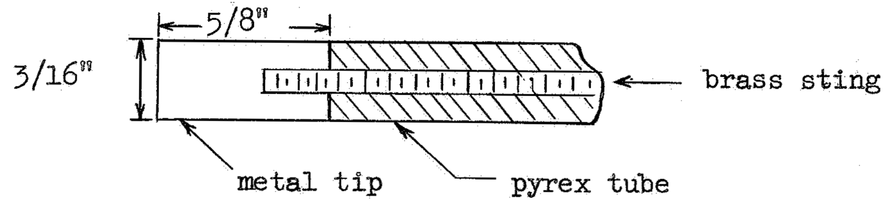

a) Blunt probe.

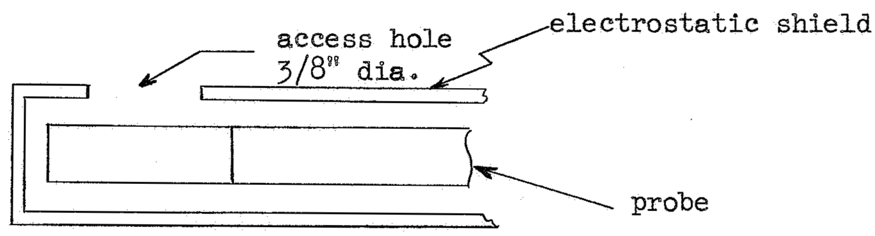

b) Electrostatic shielded probe.

Fig. 36. Sketch of Hollyer's precursor probes.

With the blunt probe, Hollyer found a negative signal ahead of the shock with a maximum on the order of -1 volt; when the shock arrived at the probe the signal rose sharply to a positive value. The potential was measured across a 1 megohm resistor connecting the probe to the grounded shock tube wall. The precursor signal was detected approximately 45 μs before the shock arrival.

To determine if the positive signal is due to induction, the probe was operated with a DC bias voltage. It was found that a bias of -3 volts was required to reduce the signal to zero just ahead of the shock. With this bias the signal was positive at the beginning of the trace. Hollyer concludes an induced signal could not be eliminated by this bias.

Using the electrostatically shielded probe, a negative signal was detected (magnitude not indicated). No signal was observed with the access hole taped; and a positive bias on the collector increased the negative signal. With a bias of -6 volts no signal was observed. This test led Hollyer to the conclusion that only electrons are present outside the access hole. He does note that the massive positive ions may not respond quickly enough to produce measureable signals.

The shielded probe was also used for a Mach 12 shot in krypton. In this test both positive and negative charges were detected; the signals were at a constant level as the shock wave approached. Hollyer interprets these results as significant photoionization of the krypton as the Mach number is increased. Unfortunately no mention is made of an argon shot at Mach 12 to be compared to the krypton result.

There are two possible sources of electrons by themselves ahead of the shock wave: a) electron diffusion from the ionized gas behind the shock, or b) photoemission electrons from the shock tube walls. Two experiments were run to indicate which of these mechanisms was operative. Hollyer reasoned that if electron diffusion is important, the distribution of electrons and the accompanying electrostatic field should be radially dependent. Repeated shots with the blunt probe displaced radially demonstrated no variation of the signal. He reasoned that if photoemission is important, a change in the work function of the walls should change the results. To obtain a significant change in the work function the probe was mounted in the last six inches of a thirty inch glass section. Figure 37 displays two of Hollyer's signals. They are signals corresponding to identical test conditions,

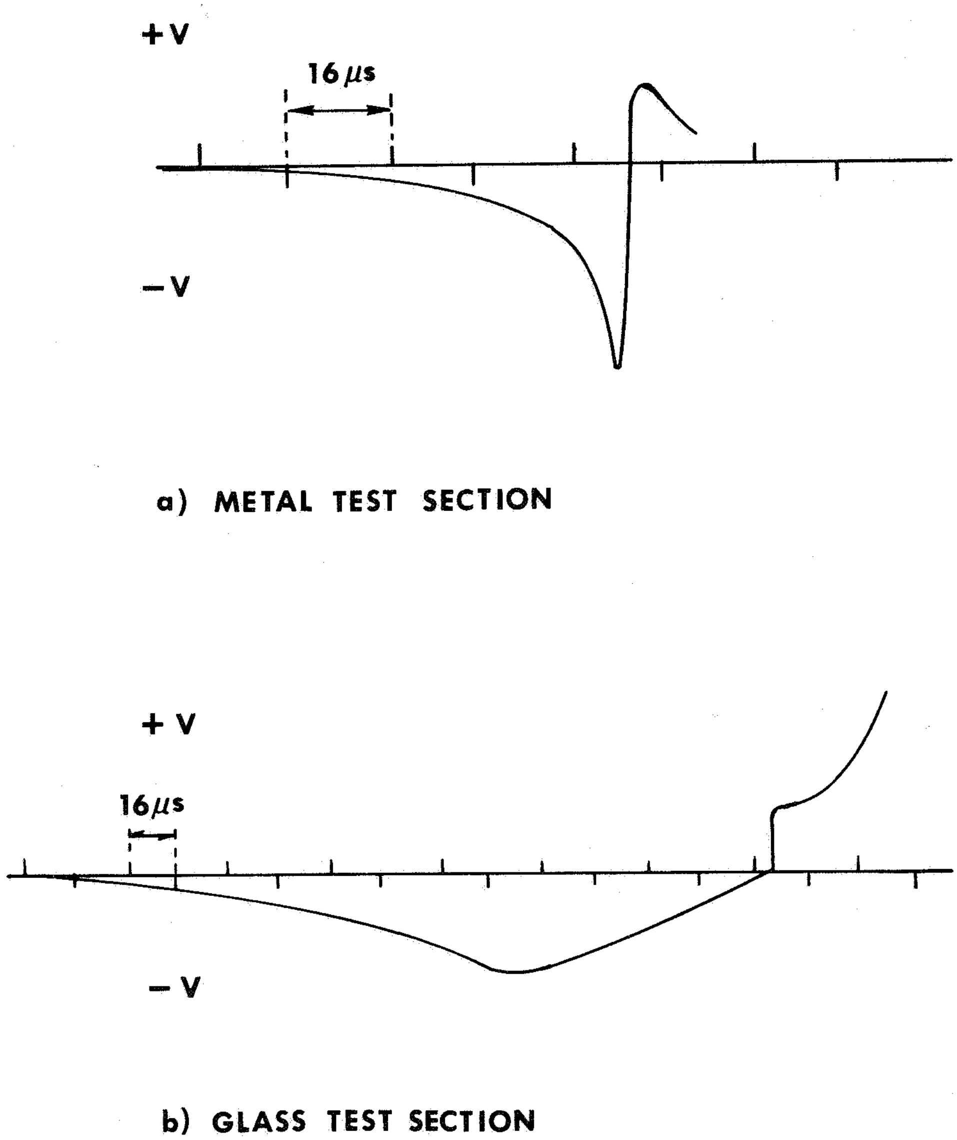

Fig. 37. Sketch of Hollyer's precursor data.

the same probe but the first in a metal test section and the second in the glass test section. Hollyer concludes from this modification that the signal is due to photoemitted electrons.

To test for the effects of photemission from the probe surface, the probe area was increased by using a flat disk of radius 7/8 of an inch. Hollyer claims photoemission from the disk occurred when the shock was some distance away. In this case the oscillogram trace started out about 1/2 volt positive but went negative when the shock approached to within a few inches of the probe. Presumably at this point the collection of photoelectrons from the walls predominates. In another test, a disk collector with only the back side exposed led to an increase in the collected current by a factor of about five.

Hollyer found his precursor signals to be very much dependent upon the gas purity. Testing at Mach 9 and with the blunt probe, Hollyer found: 1) Mechanical pumping only, a signal appeared about 8μs ahead of the shock and reached a maximum of -0.2 volts. 2) Deliberately contaminating the tube by adding air (5%), the signal amplitude decreased by a factor of four. 3) Diffusion pumping added, the precursor signal could be detected approximately 45 μs ahead of the shock and the maximum amplitude increased by a factor of five.

No quantitative analysis of the experimental data was presented. Hollyer points out that these results are probably very sensitive to Mach number and initial pressure, hence the results should not be generalized to all strong shock waves.

Petschek and Byron[2] in the course of using electrostatic probes to measure ionization relaxation times in argon observed a potential jump of approximately one volt at the translational shock front, but make no mention of a precursor signal.

In the process of measuring electrical conductivity behind shock waves in argon with electrostatic probes and magnetic search coils, Lin[3] and co-workers encountered a large electrostatic effect associated with the shock waves. A large precursor voltage signal was picked up by electrically floating probes connected directly to an oscilloscope. They did not pursue the origin of this signal, but they made the noteworthy observation that the voltage seemed to be higher for weaker shock waves. This work was done in a glass shock tube.

Groenig[4] reports on spark plug discharge probe measurements performed in a metal shock tube. The shock tube had a 1.8 inch square cross-section and was 9.8 feet long. With the discharge probe data he infers changes in conductivity as a function of time before shock arrival. The experiments were performed in argon with initial pressures 0.7 to 10 mm Hg and a Mach number range of 6 to 10. The response of the discharge probe was in the following three steps: 1) The voltage across the spark gap first drops discontinuously (10-30 cm ahead of shock) and after a transient comes to a constant value. Groening interprets this as an established discharge in the test gas ahead of the shock, it is triggered by irradiation of the probe by the radiating gas behind the shock. 2) As the shock approaches (1-5 cm ahead of the shock) the voltage decreases rapidly until arrival of the shock wave. This is explained as increased conductivity of the gas ahead of the shock. 3) As the shock passes the probe the voltage again drops due to further increase in conductivity of the shock heated gas. By changing polarity of the voltage applied over the probe electrodes, Groenig concludes the increased conductivity ahead of the shock is due to electron diffusion. Groenig presents a theory to support these conclusions, which we shall review later with other theoretical treatments.

Gloersen[5,6] has observed electrical precursor signals in xenon shock tube tests. The experiments were conducted in a helium driven glass shock tube, two inches inside diameter, with a driven section length of ten feet. High purity xenon was used; the driven section was evacuated to pressures less than 3×10^{-6} Torr. With an average leak rate of less than 0.5 μ/hr, Gloersen estimates an impurity level of less than 5×10^{-5} Torr at the time of diaphragm rupture. The potential ahead of the shock was detected by two rings (2 mm wide brass shim stock) external to the shock tube connected to the cold water pipe ground through 1 megohm resistors. A brass end plate connected to ground in the same manner was used as a third probe. The voltage developed across the 1 megohm resistors was recorded as a function of time after diaphragm rupture by oscillogram. To facilitate review of Gloersen's results, Fig. 38 presents two sketches of his experimental data. Traces A and B are from ring probes located 100 and 60 centimeters respectively from the end wall of the shock tube. Trace C is the signal from the brass end wall. The traces are terminated at the time corresponding to shock arrival at each probe. Time is measured with respect to diaphragm rupture.

The first case (a) shows a positive signal on all three probes at the same time. Comparison to a photomultiplier output shows that

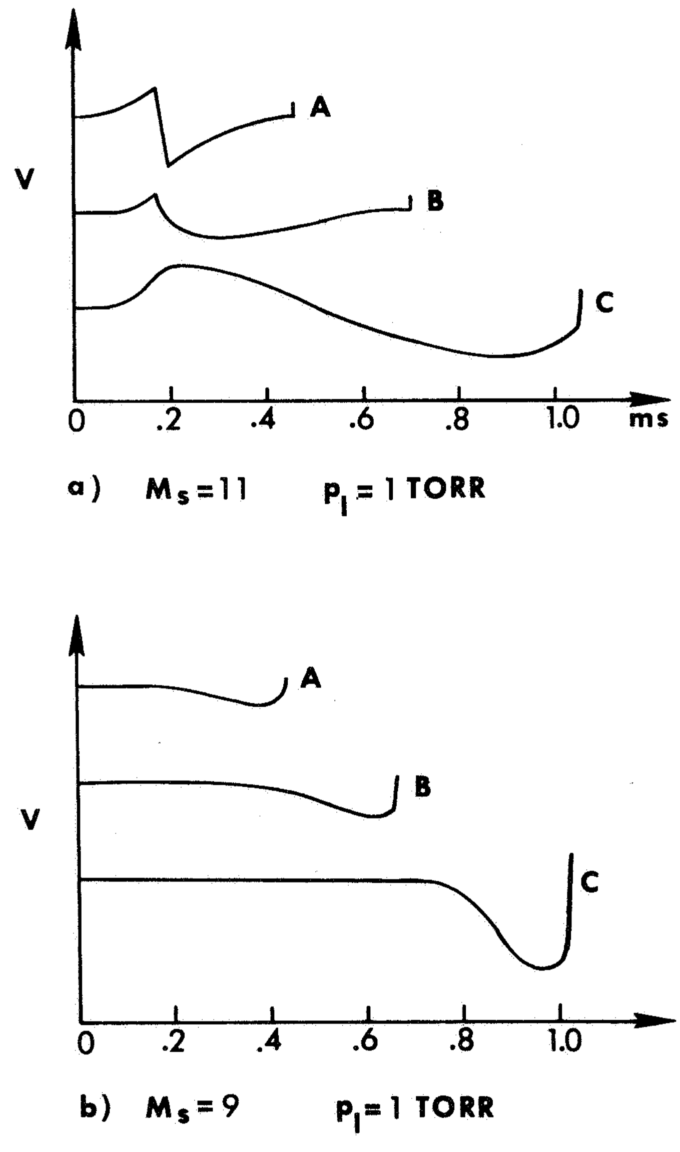

Fig. 38. Sketch of Gloersen's precursor data.

these signals appear at the same time radiation from the equilibrium region (delayed luminosity) appears behind the shock. This signal is apparently transmitted at the speed of light. The arrival of the shock is marked by a positive rise of the measured potential.

Case (b), same initial pressure but lower Mach number exhibits very different precursor signals. At this test condition the delayed luminosity did not appear until the shock was within 20 cm of the end wall. Gloersen does not mention the fact, but the data seems to indicate the precursor has not reached a steady state in the shock wave coordinates.

Gloersen postulates the positive precursor signals which appear simultaneously with the onset of delayed luminosity are the result of photoemission at the probe location; he does not indicate a clear interpretation as to why they go negative after the initial positive rise. He suggests the second type precursors may be due to short range radiation phenomena or diffusion of electrons. He notes that an impurity luminosity appears in all the above cases at the translational shock front. It was found that any impurity on the walls caused inconsistent electrical data even when the luminosity showed no effect. In all cases it was possible by sufficient cleaning to attain repeatable results. A magnetic field of 1200 gauss was placed at the location of the first ring probe. This failed to modify the results in any way.

Weymann[7] reports two experiments on precursors ahead of shock waves in argon. The experiments were performed in a pressure driven glass shock tube (dimensions not indicated; however, a length of less than ten feet can be inferred from the data), with about 5 Torr of argon initial pressure. Ring electrostatic probes external to the shock tube were used at several stations for the first experiment. The potential of these rings was monitored by Tektronix low capacity probes in conjunction with an oscilloscope. Negative precursor signals were observed with a maximum occurring at shock arrival. The maximum signal varied from -1 volt for Mach 8 to about -10 volts for Mach 12. It was found that the speed of the leading edge of the precursor varied approximately inversely with the square of the time after its first appearance. Also a delay in the appearance of the precursor was found to be a function of the diaphragm material. The second experiment used an induction coil around the shock tube. Presuming the precursor was made up of electrons resulting from large scale electron diffusion, the flowing electron gas ahead of the shock becomes a current to an observer in the laboratory. The form of the induction voltage indicates that the negative current due to electrons diffusing ahead of the shock front first increases then decreases. This arrangement failed to work below Mach 12 due to noise. At Mach 12, $p_1 = 4$ Torr, Weymann estimates the electron number density ahead of the shock to be of the order $10^7/cm^3$. Weymann concludes electron diffusion generates the signals he observed.

An abstract on work performed by Weymann and Troy(8) indicates that using a probe capable of measuring relative densities of electrons and ions, they found equal numbers of ions and electrons up to 5 cm ahead of argon shocks. They attribute this to ambipolar diffusion. For distances between 5 and 50 cm ahead of the shock they found a much higher electron density which decreases exponentially with distance from the shock. Their theoretical treatment indicated this is due to free diffusion of electrons at a temperature equal to the equilibrium temperature behind the shock. The abstract fails to say anything about the shock tube, Mach number, initial pressure, or the nature of the probe.

Holmes[9,10] reports on experiments conducted in a 13 foot glass shock tube, 1 1/2 inch inside diameter with a hydrogen driver. Welding grade argon was the test gas, the Mach number range 9-11, and initial pressures of 2.5, 5, and 10 Torr. Ring electrostatic probes and a collecting type probe were used at several stations on the shock tube. The collecting probe consisted of a grounded screen flush with the inside wall of the shock tube backed up by a biased plate. Holmes presents a theory for the operation of this probe and indicates ion and electron densities from $10^9/cm^3$ to $10^{13}/cm^3$ could be measured. The potential probes detected negative precursor signals almost simultaneously at all stations, indicating that the precursor propagates with a speed comparable to that of electromagnetic radiation. The collecting probes found equal electron and ion density profiles which increase monotonically with time as the shock wave approaches the position of the probe. Observable plasma densities were obtained up to 160 cm ahead of the shock wave. The density profiles did not become stationary with respect to the shock front at distances up to 310 cm from the diaphragm station. Holmes presents a theory of multiple step photoionization of the argon test gas to explain his results. We will discuss his theory in a later paragraph.

The most recently reported experimental investigation of precursors was conducted by Lederman and Wilson.(11) Using a metal, 0.891 inch diameter, 10 foot long shock tube, they have measured electron densities ahead of shock waves in argon with a microwave resonant cavity technique. The measurements were made for Mach 10.9 to 13.4 and initial pressure 1 to 10 Torr. With reasonably sized microwave cavities and an operating frequency of 2.7 kmc, a sensitivity range of $5 \times 10^7/cm^3$ to $1 \times 10^{10}/cm^3$ was achieved. Electron densities between $10^7/cm^3$ and $10^8/cm^3$ were detected up to 40 cm ahead of the shock. The extent of the precursor was found to be larger for higher Mach numbers. They found the precursor velocity to be the same as the shock velocity. Two experiments were conducted to see if diffusion or photoelectric effects produced the precursor. The first was to insert a teflon block with holes drilled oblique to the axis of the tube. Such a device would block radiation but permit diffusion electrons to penetrate, even if at a reduced rate. The microwave cavity detected no electrons behind this obstacle. A biased grid was also inserted to collect electrons but pass the radiation; this device biased either positive or negative had no effect on the precursor. These tests led to the conclusion that photoionization is at least the major cause of precursor ionization. To discredit the possibility of photoemission from the walls of the shock tube, ion collection probes were inserted which indicated the presence of ions in the same quantities as electrons. A preliminary theoretical calculation is mentioned for one step photoionization of O_2($3\ \mu$ Hg O_2 in 1 Torr argon) which gives good agreement with experiment.

A.2. Review of Theoretical Precursor Literature.

Qualitative conclusions drawn from the experiments reviewed above indicated three mechanisms for precursor phenomena: 1) electron diffusion, 2) photoionization of the test gas or impurities contained in the test gas, and 3) photoemission from the shock tube interior. Only the first two of these possibilities have received theoretical attention.

There are two categories of electron diffusion theories and two levels of sophistication in each category. The first category is electron diffusion from the translational shock region. Papers in this category are split into those which assume a source of charged particles and those which include the chemistry of the charged particle production. The second category is electron diffusion from the ionization front which is prominent in noble gas shock structure. This second category also splits into papers which idealize the ionization profile and those that include ionization and recombination chemistry. We will review these theories in the order outlined above.

Wetzel[12] considers electron diffusion in argon. He reasons that the electrons in the equilibrium region behind the shock wave are most likely governed by ambipolar diffusion and that free electron diffusion is needed to produce the experimentally observed precursors. Wetzel considers electrons directly behind the translational shock front. Furthermore, he postulates these usually low energy electrons may be heated by "thermionic emission" from the equilibrium region. Wetzel models the electron source as a constantly replenished reservoir directly behind the shock front. For one-dimensional considerations he collapses this reservoir to a plane electron source, with strength proportional to the shock speed, located at the translational shock. Wetzel points out that if diffusion occurs, electrostatic space charge effects should be included; however, he says that the diffusion should be examined before including these effects, thus he ignores them in this work. He first presents the equilibrium one-dimensional solution to the steady diffusion equation which is an exponential in terms of the shock speed, reservoir properties, and the electron diffusion coefficient.

Wetzel also performs a transient analysis with the plane source model, again neglecting electrostatic effects. Solving the time dependent diffusion equation he demonstrates that the equilibrium solution is recovered as time goes to infinity. This solution turns out to be a complimentary error function. Wetzel was particularly interested in explaining the results of Weymann's experiment, his success was limited to finding the same unsteady growth rate of the precursor. He was not able to predict the shape of Weymann's results and postulated this may be due to saturation or sensitivity cutoffs associated with the probes.

Pipkin[13] supposed that electrons are created by some mechanism in the vicinity of the shock and escape the positive ions in the region where they are produced. He considers the subsequent motion of the electrons in the upstream region where the positive ion density is negligible. Pipkin postulates the electron distribution in the precursor region produces an electric field which extends mainly into the surrounding space rather than along the tube axis (prompted by Weymann's experiment in a glass shock tube). The voltage to ground at a given cross-section was estimated by neglecting the axial component of the electric field. He uses the concept of distributed capacitance along a conducting wire, which yields a voltage proportional to the charge on the cross-section. He then finds the axial component of the electric field to be proportional to the electron density gradient. This field then exerts a repulsive force on the electrons which drives them from regions of higher density to regions of lower density.

Pipkin forms a set of governing equations neglecting the presence of ions and assuming the neutral upstream gas forms a medium of uniform, constant properties through which the electrons flow. In dimensionless form the equations of motion involve a single dimensionless parameter, ϵ, which Pipkin regards as the ratio of the electron thermal energy to the electrostatic energy. He points out that when ϵ goes to infinity his results reduce to Wetzel's results discussed above. Pipkin is interested in small values of ϵ and the limiting value of zero.

He finds a linear electron distribution for the steady state $\epsilon = 0$ case. This is essentially neglecting the electron pressure gradient. For small non-zero values of ϵ, the pressure gradient produces a low density distribution of electrons ahead of the $\epsilon = 0$ front, which decreases exponentially with distance upstream.

Pipkin also considers the time dependent problem. For the limiting case $\epsilon = 0$, assuming the electron density is initially zero and for time greater than zero the density near the shock is maintained constant; he considers the initial stages of the motion. He finds the electrons form a wave with a precise front, and that the distance between this front and the shock front grows as the square root of time. For small non-zero ϵ, he finds that the pressure gradient produces a very low density distribution of electrons extending from the $\epsilon = 0$ front which destroys its sharpness.

The following paper deals with electron diffusion in the vicinity of the translational shock in argon but includes an electron production mechanism. Appleton[14] makes the following assumptions: 1) the flow is one dimensional and steady when viewed in the shock-fixed frame of reference, 2) the temperature of the electrons remains constant and equal to the downstream equilibrium temperature through the region of interest, and 3) the diffusion velocity of the heavy ions is so very much smaller than that of the electrons that the ions and neutrals may be regarded as having the same mean flow velocity.

Appleton employs an electron continuity equation, a positive ion continuity equation, an equilibrium electron force balance which includes a friction term due to collisions with the neutrals, and the one-dimensional Poisson equation. A knowledge of the electron production mechanism and the neutral particle shock structure is required in this formulation. Appleton assumed the presence of electrons and ions does not influence the structure of the translational shock, thus he used the Mott-Smith theory for the variation of mean flow velocity, density, and temperature of the neutral particles as a function of position through the translational shock wave. For the electron production mechanism, Appleton employed the experimental results of Harwell and Jahn.

Appleton solved this problem numerically and found that the electrons and ions are distributed within the heavy particle shock so as to form a charge double layer with a peak in the electric field intensity where electron and ion number densities are first equal to one another. Appleton views his results as a "near" solution which should be matched to a three-dimensional free diffusion "far" solution. Appleton also makes some comments and calculations pertaining to photoionization; we will discuss these later on in this review.

We now turn to papers which deal with electron diffusion around the ionization front. Pipkin[15] deals with a model situation. He considers the ion diffusion in a stream of neutral gas in steady one-dimensional motion through a zone in which ionization takes place at the small given rate. With no shock present, and only a small degree of ionization, he regards the neutral atom stream as a uniform background in which the ion diffusion takes place.

Pipkin found that the small difference between the electron density and positive ion density due to diffusion is such that a charge double layer appears at the upstream edge of the ionization zone. The positive layer is on the downstream side, the negative layer is upstream. The electric field was small everywhere except between the two layers. He found the characteristic length for decay of the electron density is the Debye length, regardless of how large the electron free path may be.

Weymann[16] and Groenig[4] have presented formulations of a rather comprehensive model for the diffusion of electrons about a step function ion profile located at the ionization front in argon. Both analyses fall very short of the model they present. The only solution they obtained was that to the one-dimensional steady equilibrium problem. Their force balance includes only the electron pressure gradient and the electrostatic field resulting from charge separation. Both authors mention that a friction term due to relative motion between the background gas and the electrons should be included. Weymann argues that this force is small compared to the electrostatic forces. Groenig includes it in his equations but says he couldn't solve them so he quotes Weymann's solution without that term. Both authors consider the time dependent problem but they neglect electrostatic forces.

Ong and Turcotte[17] have presented some analysis on the structure of ionization fronts. They consider a non-linear ionization wave front moving into a quiescent gas. The front propagates due to ionizing collisions between electrons and neutrals. The diffusion of ions is neglected compared to the electrons and the temperatures are assumed constant. They consider the case of electron temperature much greater than the heavy particle temperature. Their electron momentum equation includes the electron pressure gradient, electrostatic forces, and frictional forces. The formulation includes electron production and loss terms and considers Poisson's equation in a self consistent manner. For one range of parameters they verify Pipkin's prediction of a charge double layer imbedded in the ionization fromt.

Bond[18] has performed a perturbation type analysis on this argon shock structure solution and has found a charge double layer due to diffusion in the ionization front.

We now briefly consider the reports which deal with photoionization precursors. Ferrari and Clarke[19] have presented an elegant analysis of radiative and collisional ionization processes in monatomic gases. Wetzel[20] has isolated the precursor photoionization aspect of Ferrari and Clarke's considerations and presents solutions for the number density profile ahead of a photon source. Ferrari and Clarke demonstrate that Wetzel's approximation agrees with their more complicated analysis. These theories deal with one-step photoionization, i.e., no intermediate excited states are considered in the precursor region. Both theories demonstrate that one-step photoionization of argon decays much too rapidly to predict the experimental results observed.

Chapin[21] in a study of argon shock structure including trapped radiation and radiation cooling also considers the precursor. He too considers only one-step photoionization in the precursor and his results predict precursors much too small in comparison to the experiments reviewed.

Holmes[9] examines Ferrari and Clarke's analysis and verifies the above statement. He goes on to argue at some length that two-step photoionization of argon may predict satisfactory precursor profiles. Holmes was unable to complete his calculations due to the lack of absorption cross-sections for the excited states of argon.

As a final item in this review we mention briefly a calculation by Appleton.[14] Appleton examines Holmes' experimental results in terms of photoionization of impurities. He finds that it is very possible to predict these results with one part per million oxygen impurity assuming the shock heated argon radiates like a black body with brightness temperature approximately equal to 11,000° K.

APPENDIX B

SHOCK-TUBE FACILITY AND PRECURSOR-EXPERIMENT INSTALLATION

Only those features of the shock tube which are pertinent to the present experiments will be discussed here. The basic shock tube consists of a stainless steel driver section, a 4 1/2 inch stainless steel transition section, two 10-foot and one 4-foot extruded aluminum sections with square interior cross-section (2 inch by 2 inch). Added to this are the test sections and a dump tank or an end wall (for reflected shock studies). The scribed aluminum (2024-0) diaphragms insert between the driver section and the transition section. A stoichiometric mixture of oxygen and hydrogen diluted in helium and ignited by spark plugs is the normal driver. The facility can also be used with high pressure helium drives.

Separate experiments were performed with 10 feet and 24 feet of the aluminum extrusion. Added to these nominal lengths were a 2 foot section with appropriate shock detector ports, the insertable probe section (see Appendix C), and an 18 inch section with the biased electrode mounted 2.75 inches from the dump tank diaphragm (see Fig. 39). Preliminary experiments were conducted with 20 feet of the extrusion plus the shock detector section with the probes mounted in an end wall.

The shock tube was diffusion pumped to 0.1 μ Hg or less prior to each run. The combined outgassing and leak rate was kept to 4 μ Hg/hour

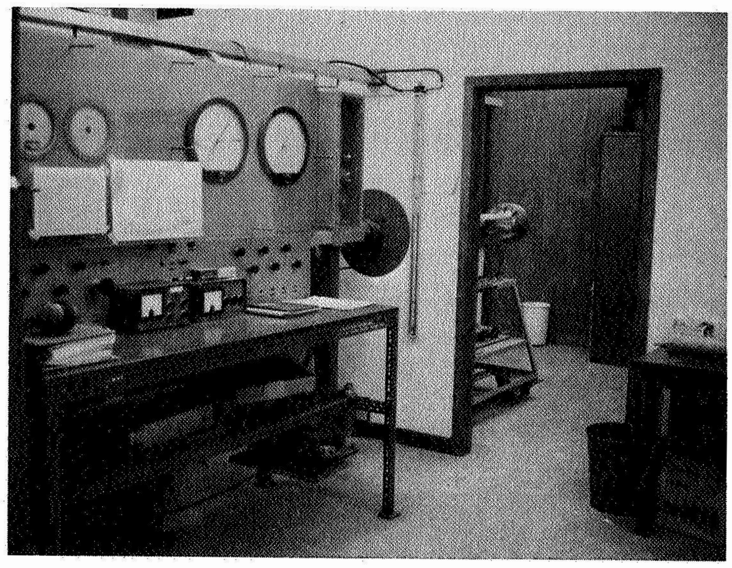

a) Control room and driver section.

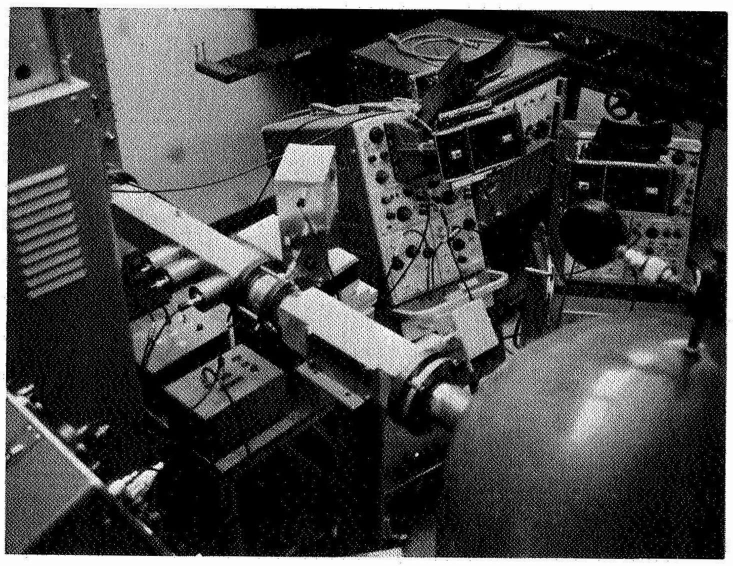

b) Test section with typical test setup.

Fig. 39. Photographs of Stanford Aerophysics Laboratory shock tube with precursor experimental setup.

or less. After each shot the shock tube was cleaned with dry cheesecloth. Cleaning with acetone, even with considerable pumping, led to inconsistent results and greatly enhanced photoionization ahead of shock waves in argon. This was attributed to a residue of acetone vapors in the connecting joints between the extruded aluminum sections. The data was very repeatable using the dry cheesecloth cleaning procedure.

Two shock detectors separated by 100 millimeters were used to determine the shock speed. Thin film gauges and barium titanate crystals were employed in the low and high Mach number regimes respectively. The shock travel time was measured with a 0.1 μs time interval counter (Beckman/Berkeley Model No. 7370R). The error in the Mach number measurement was

$$\frac{\Delta M_s}{M_s} = .022$$

The initial pressure of the working gas was measured with a 0-20 Torr Wallace and Tiernan (Model FA 160) vacuum gauge, calibrated by a McLeod gauge (CVC Type GM 100). The estimated errors in the initial pressure reading were

$$.005 < \frac{\Delta p_1}{p_1} < .02$$

for the 2.5 Torr to 10 Torr test range.

Figure 40 presents a block diagram of the instrumentation set-up used for the precursor experiments. After filling the working

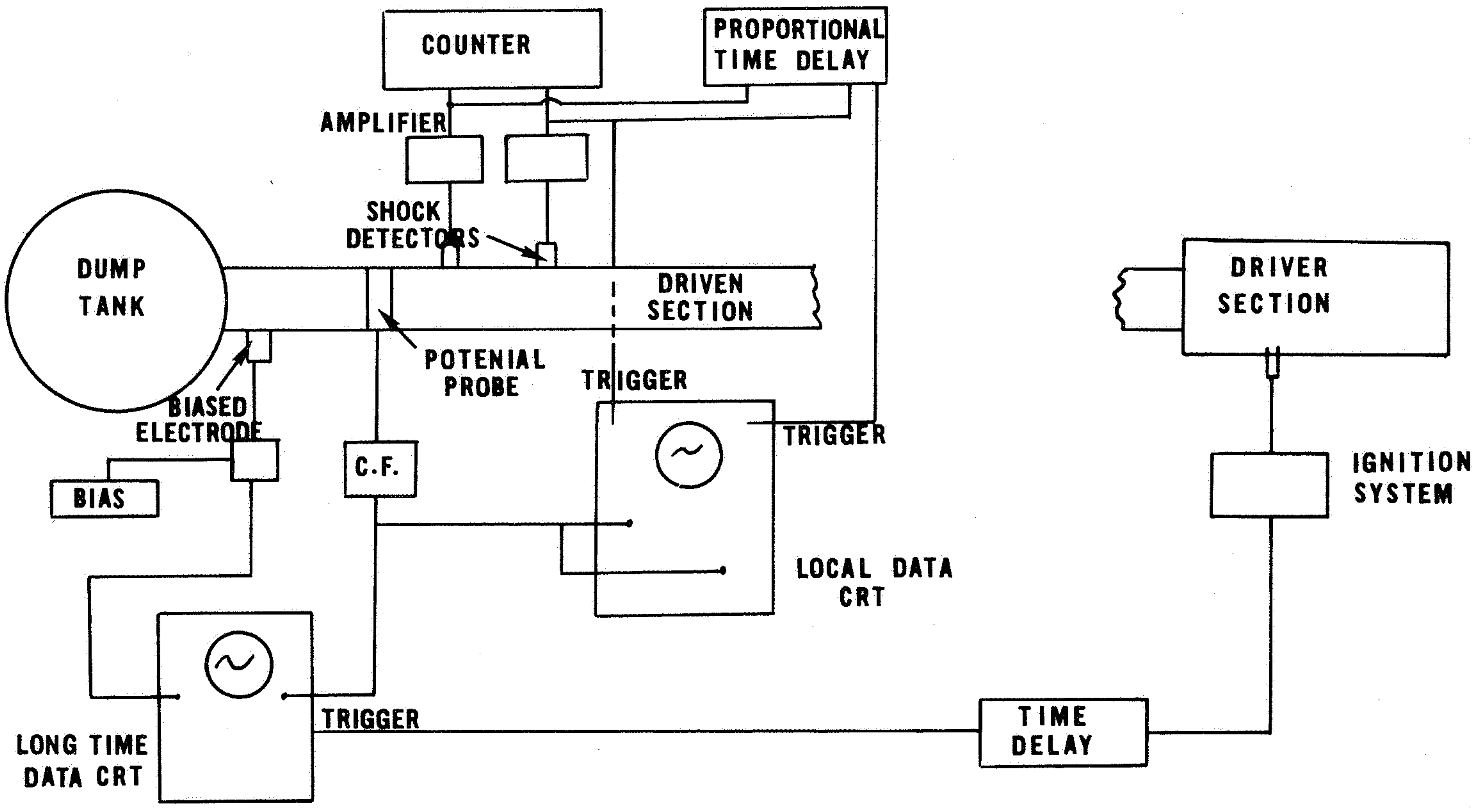

Fig. 40. Block diagram of instrumentation setup used for precursor experiments.

section of the shock tube with the appropriate test gas to the desired initial pressure, the driver was loaded with the combustible gases and helium. The sequence of events during an experiment was as follows: The ignition circuit was fired and the accompanying noise signal triggered a time delay generator (Abtronics Model 200). After a delay of 1 to 5 milliseconds, dependding on the driver loading, the dual beam oscilloscope (Tektronix 551) recording the long-time data was triggered just before diaphragm rupture. As the diaphragm opened and the shock wave traveled down the tube, long-time data from the biased electrode and the mesh electrode was collected. As the shock wave passed the shock detectors the resulting signals were amplified ($\times$ 30 for piezoelectric pressure gauges, $\times$ 300 for thin film gauges). The time between these two signals was recorded by the counter for the shock speed measurement. These signals also triggered a proportional time delay[35] and one of them (depending on the experiment) triggered the upper beam of the "local" data oscilloscope (Tektronix 555). The lower beam was triggered by the proportional time delay output (preset to put out a trigger pulse at a fraction of the time between the two input pulses). The oscilloscope data was recorded with Polaroid 4000 speed film. All time bases were calibrated with a Tektronix 180A Time Mark Generator.

Having performed experiments with three different lengths of driven section enabled us to make a rough determination of the shock wave attenuation by comparing the performance of the three tube lengths. Figure 41 shows plots of the local shock Mach number at the test section for the three tube lengths versus the ratio of the final pressure of the

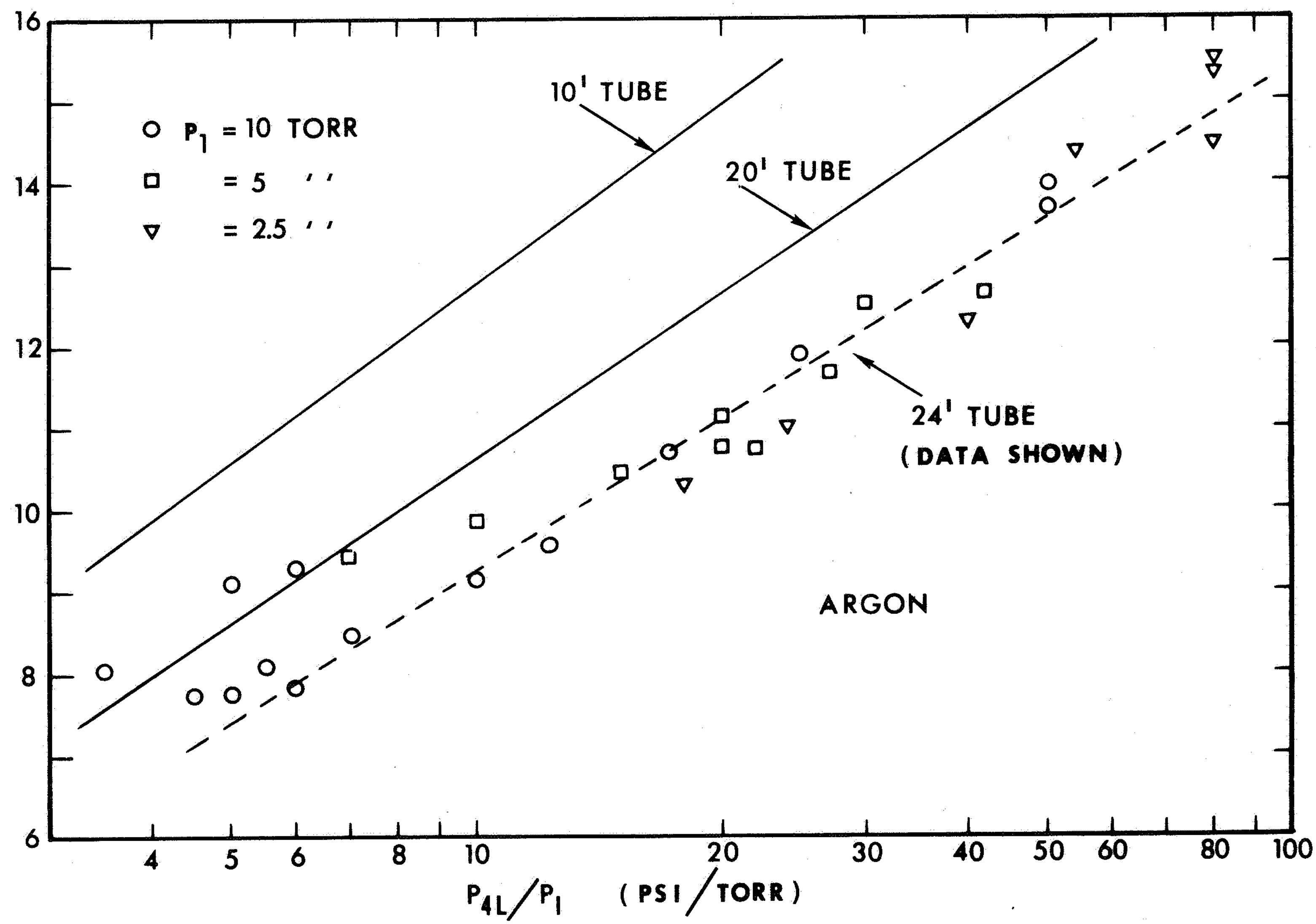

Fig. 41. Combustion driver performance curves for 10, 20, and 24 foot shock tube lengths.

combustion loading to the test gas initial pressure. As noted on the figure these results are for argon. The actual data points are shown only for the 24 foot tube to illustrate the scatter and lack of reproducibility inherent in this type facility. From these curves we deduced that there is approximately 2% per foot attenuation in the shock Mach number.

APPENDIX C

MECHANICAL AND ELECTRONIC DETAIL OF THE PRECURSOR PROBE

C.1. Mesh-Electrode Potential Probe.

The potential probe was designed to effect a measurement of the potential ahead of a shock wave with minimum distortion of the precursor phenomena. This criterion requires a probe which introduces minimal changes in the boundary conditions. A porous electrode was chosen to avoid compression of precursor charged particles between the electrode and the shock front. The electrode was a 1/2 inch diameter circular piece of bronze wire cloth (200 by 200 mesh). This electrode blocked less than 4% of the shock tube cross-sectional area. The electrode had to be isolated from the shock tube walls, thus a Lucite frame was designed to support the electrode. Two pieces of copper wire were stretched across the frame, the electrode was centered in the shock tube and soldered to the wires. The frame then formed a small section of the shock tube wall. The exposed area of the lucite and its depth were minimized to preserve as closely as possible the grounded metal wall boundary condition. The exposed Lucite in the design required the use of a dump tank to eliminate shock reflection and hence the extreme temperatures and pressures in the reflected region. The dump tank also acted as a convenient receiver for the used electrodes. The lucite frame and the mesh electrode were nested in a small section of the standard shock tube extrusion. An appropriate BNC connector was provided to make shielded connections to the electronic instrumentation. Figure 42 shows an illustrative assembly drawing of the probe design. Photographs of the probe pieces and an assembled view are shown in Fig. 43.

The high impedance required to make a reliable potential measurement was provided by a 15 megohm cathode follower shown schematically in Fig. 44. The time response of the cathode follower, cabling, oscilloscope (Tektronix 555 with Type K, Type L, and Type G plug-in preamplifiers) was checked with a Tektronix Type 107 square wave generator (3 ns risetime). The rise time of the entire system was 0.1 μs.

C.2. <u>Biased Electrode Probe</u>.

The biased electrode probe was used only as a charged particle detector and thus involved no sophisticated design. The electrode was a 1/16-inch-wide silver strip (Hanovia silver paint) on the end of a 5/8-inch-diameter Pyrex rod. The holder shown in Fig. 45 isolated the silver strip from the shock tube wall. The strip was oriented perpendicular to the direction of shock wave travel and flush with the inside wall. The simple circuit used to bias the probe and measure the voltage resulting from the attraction of charged particles is also shown in Fig. 45.

C.3. End Wall Potential Probe and Pressure Gauge.

It was mentioned in the text that several preliminary precursor experiments were performed. All these experiments employed probes mounted in the end wall of the shock tube. This section briefly describes a representative sample of the apparatus employed in these experiments. A cross-sectional illustration of the end wall probes and housing is shown in Fig. 46. The potential probe was a 1/2 inch diameter silver electrode on the end of a 5/8 inch diameter Pyrex rod. The pressure gauge (used only to detect the translational shock wave) is a minature version of the type described in reference (3). Further detail on the pressure gauge construction is shown in Fig. 47. Considerable discoloration of the Lucite end wall was observed after exposure to the severe conditions behind the reflected shock wave. A photograph of the components of the end wall apparatus is shown in Fig. 48.

The electronic circuitry for the end-wall probe is identical to that used with the mesh-electrode probe. A schematic for the pressure gauge electronics is shown in Fig. 49.

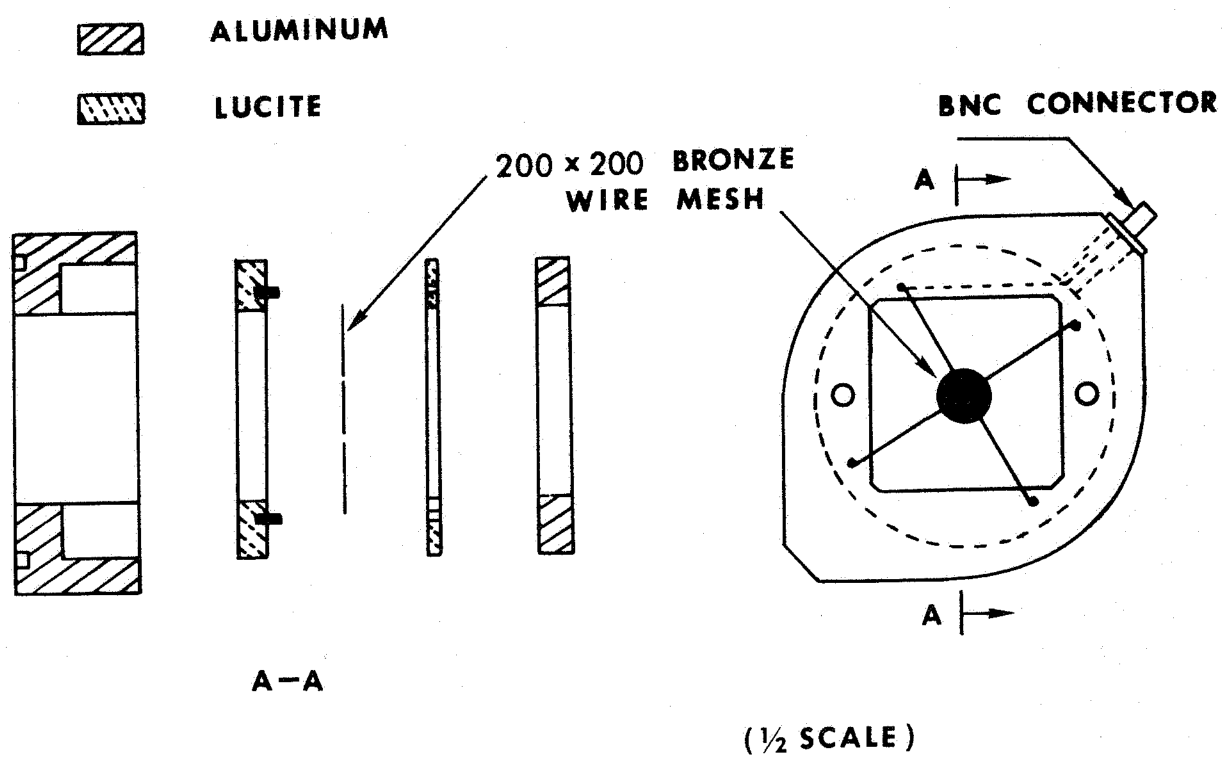

Fig. 42. Sketch of mechanical aspects of mesh electrode potential probe.

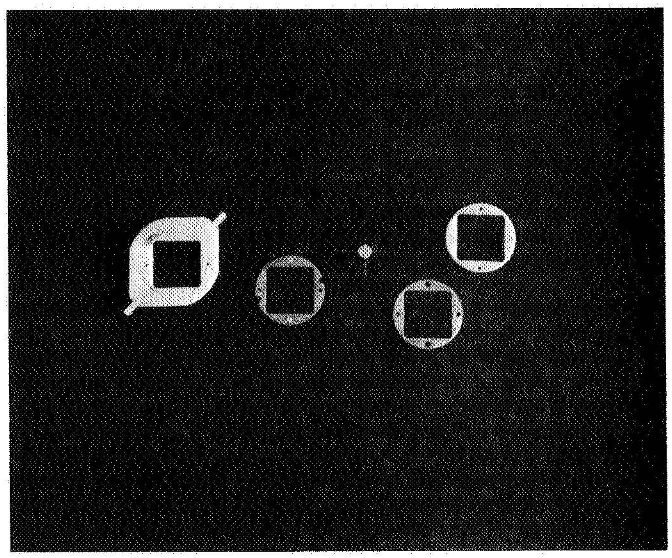

a) Probe pieces before assembly.

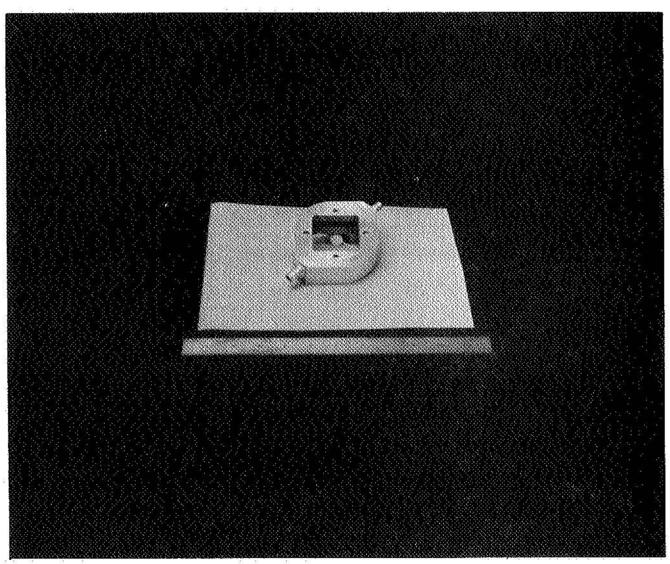

b) Assembled mesh-electrode-potential probe.

Fig. 43. Photographs of mesh-electrode-potential probe.

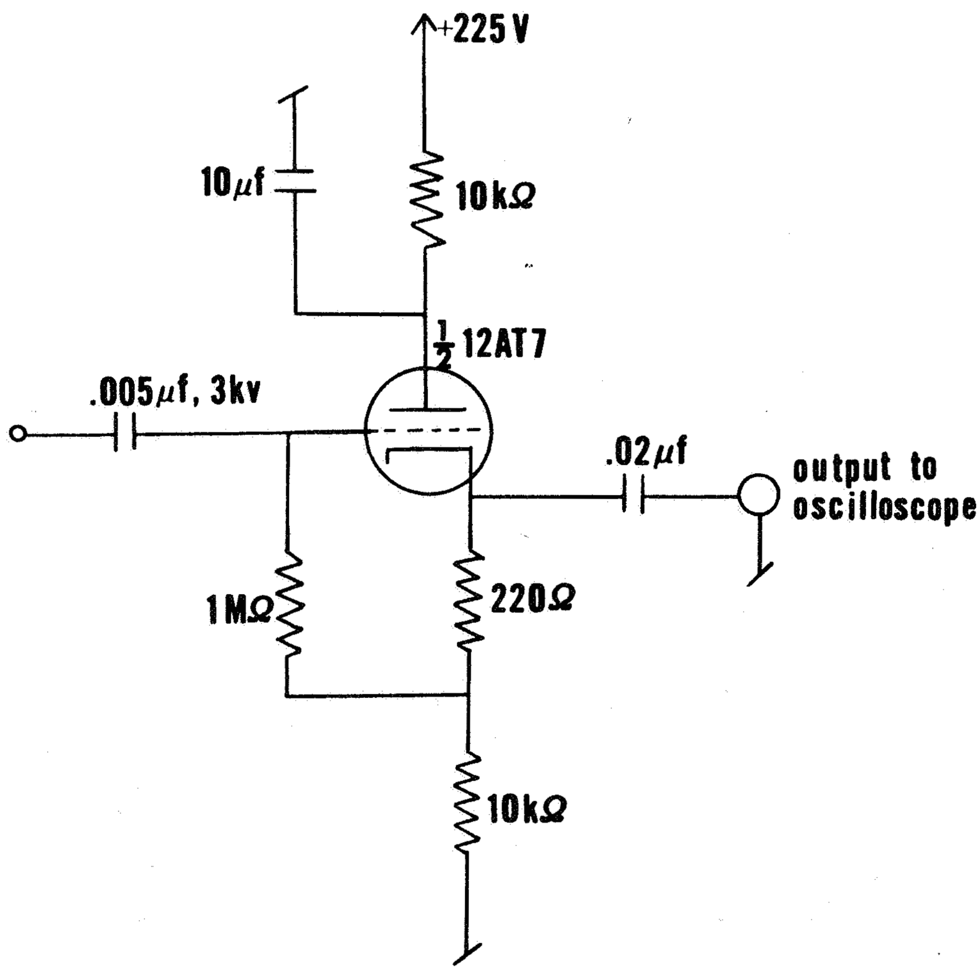

Fig. 44. Cathode follower with 15 megohm input impedance.

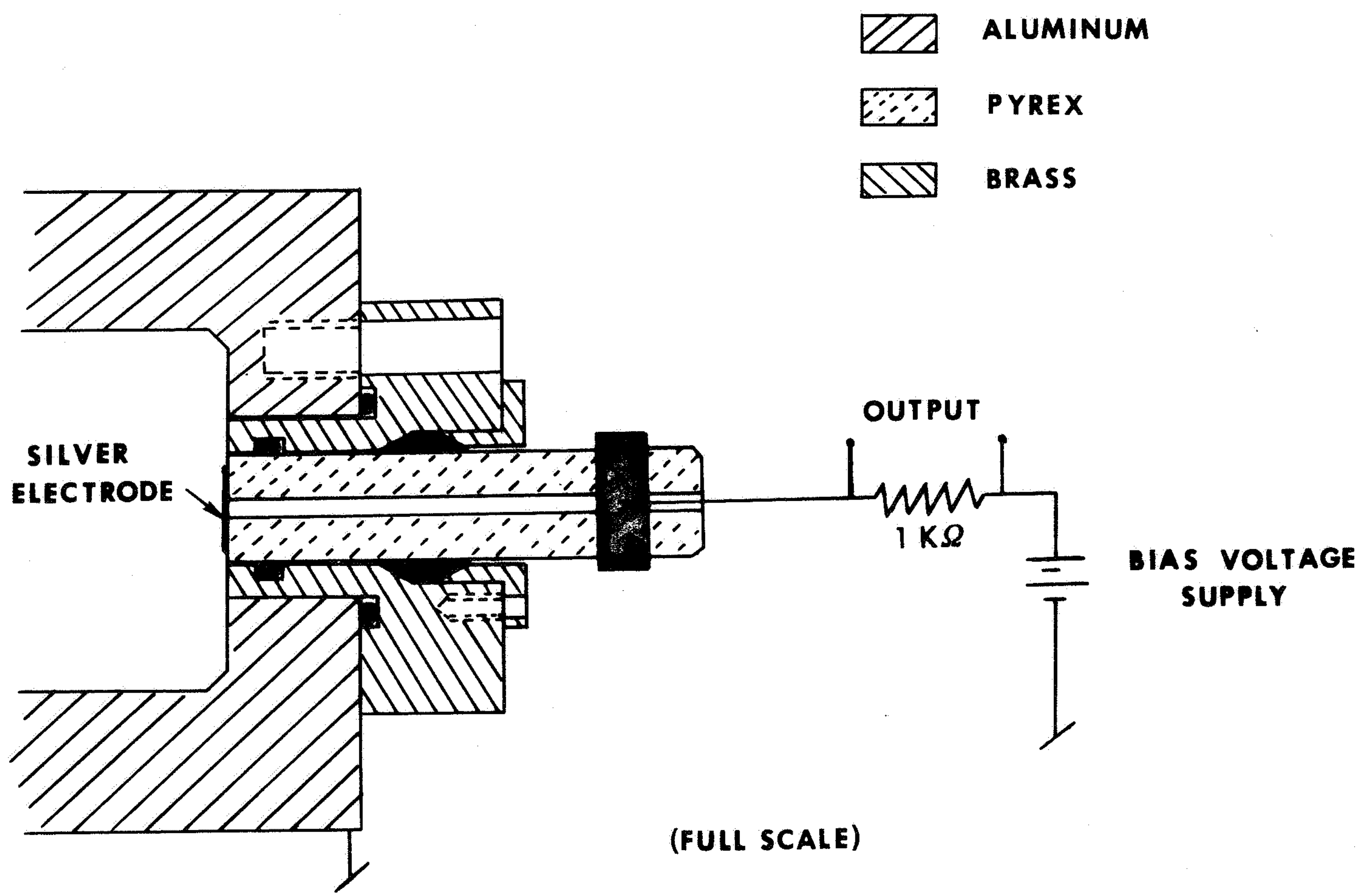

Fig. 45. Sketch of mechancial and electronic detail of the side wall biased electrode.

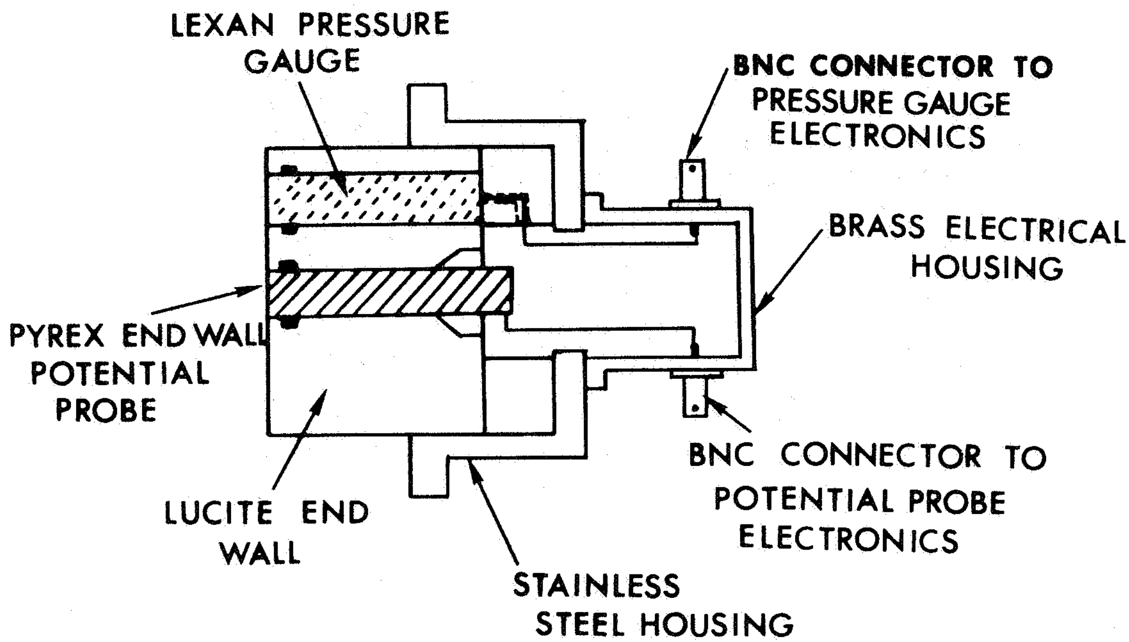

Fig. 46. Sketch of end-wall potential probe and pressure gauge assembly.

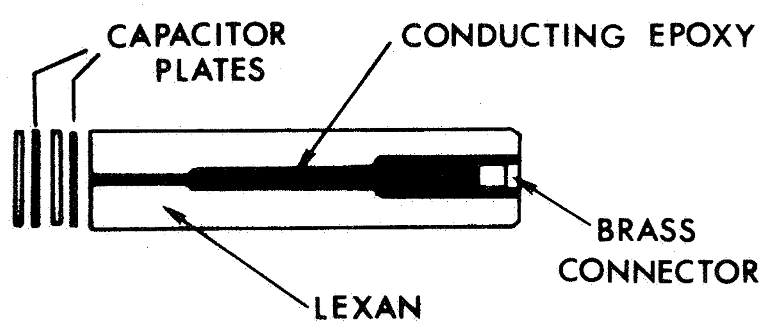

Fig. 47. Sketch of end-wall pressure gauge.

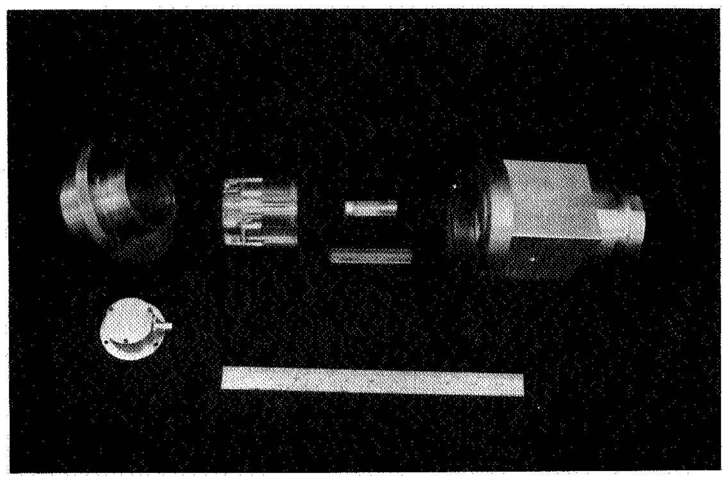

Fig. 48. Photograph of end-wall instrumentation.

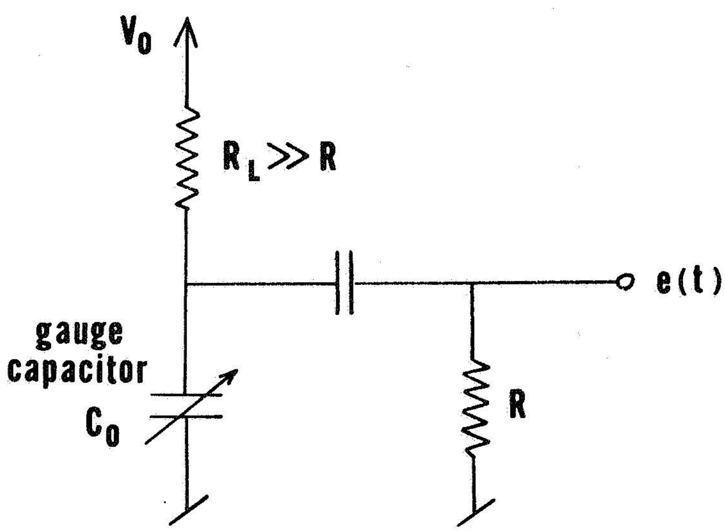

Fig. 49. Schematic of capacitive end-wall pressure gauge circuit. V_o is kilovolt voltage supply. Resistance R is the schematic equivalent of a 15 megohm cathode follower.

APPENDIX D

NUMERICAL SOLUTION OF THE PRECURSOR INTEGRAL EQUATION

The following non-linear integral equation arises in the low Mach-number precursor analysis:

$$\ln \tilde{n}_e(\tilde{x}) = B \int_0^\infty \tilde{n}_e(\tilde{\xi})\ k(\tilde{x},\tilde{\xi})\ d\tilde{\xi} - A\tilde{x} \tag{1}$$

The kernel of this equation is a function of the following form

$$k(\tilde{x},\tilde{\xi}) = f(\tilde{x}) - f(|\tilde{x}-\tilde{\xi}|) \tag{2}$$

where $f(\tilde{x})$ is non-zero at the origin and decreases monotonically away from the origin.

The first step in the numerical analysis of this equation is to expand the integral into a finite sum. We choose to use the trapezoidal rule; for n steps of size h we have

$$\int_a^b f(\tilde{x})\ d\tilde{x} = h\left(\frac{f_0}{2} + f_1 + f_2 + \cdots + \frac{f_n}{2}\right)$$

where

$$f_0 = f(a)$$

$$f_1 = f(a+h)$$

$$f_2 = f(a+2h)$$

$$f_n = f(a+nh)$$

In the text we indicated the expected behavior of the solution to equation (1) in the $(\ln \tilde{n}_e(\tilde{x}))/A$ vs. $\tilde{x}$ plane, where $(\ln \tilde{n}_e(\tilde{x}))/A = \tilde{x}$ is the asymptotic solution. For numerical purposes this provides a convenient means to determine the integration interval of interest. We must carry the integration out to $\tilde{x}$ values such that

$$\frac{\ln \tilde{n}_e(\tilde{x})}{A} + \tilde{x} < 1$$

The solutions of interest will have electrons concentrated at the origin. Thus the unknown function will be a rapidly varying function close to the origin. A very small step size is appropriate close to the origin but is not necessary away from the origin. In order to keep the computation time at a minimum but still retain a high degree of accuracy, the integration interval was broken into three parts. The step size and number of steps in each part is controlled by the input.

We can now expand the non-linear integral equation into a system of non-linear algebraic equations as follows:

$$\ln \tilde{n}_e(\tilde{x}_1) = \tilde{n}_e(\tilde{\xi}_1)\, k(\tilde{x}_1,\tilde{\xi}_1) + \tilde{n}_e(\tilde{\xi}_2)\, k(\tilde{x}_1,\tilde{\xi}_2) + \cdots + \tilde{n}_e(\tilde{\xi}_j)\, k(\tilde{x}_1,\tilde{\xi}_j) - A\tilde{x}_1$$

$$\ln \tilde{n}_e(\tilde{x}_2) = \tilde{n}_e(\tilde{\xi}_1)\, k(\tilde{x}_2,\tilde{\xi}_1) + \tilde{n}_e(\tilde{\xi}_2)\, k(\tilde{x}_2,\tilde{\xi}_2) + \cdots + \tilde{n}_e(\tilde{\xi}_j)\, k(\tilde{x}_2,\tilde{\xi}_j) - A\tilde{x}_2$$

$$\vdots$$

$$\ln \tilde{n}_e(\tilde{x}_j) = \tilde{n}_e(\tilde{\xi}_1)\, k(\tilde{x}_j,\tilde{\xi}_1) + \tilde{n}_e(\tilde{\xi}_2)\, k(\tilde{x}_j,\tilde{\xi}_2) + \cdots + \tilde{n}_e(\tilde{\xi}_j)\, k(\tilde{x}_j,\tilde{\xi}_j) - A\tilde{x}_j$$

where

j = total number of steps in the three integration intervals

$\tilde{x}_i = \tilde{\xi}_i$

Factors of 1/2 and coefficient B have been absorbed into the definition of $k(\tilde{x},\tilde{\xi})$. This system of equations may be expressed in matrix form as follows:

$$\begin{bmatrix} \ln \tilde{n}_e(\tilde{x}_1) \\ \ln \tilde{n}_e(\tilde{x}_2) \\ \vdots \\ \ln \tilde{n}_e(\tilde{x}_j) \end{bmatrix} = \begin{bmatrix} k(\tilde{x}_1,\tilde{\xi}_1) & k(\tilde{x}_1,\tilde{\xi}_2) & \cdots & k(\tilde{x}_1,\tilde{\xi}_j) \\ & & & \\ \vdots & \vdots & & \vdots \\ k(\tilde{x}_j,\tilde{\xi}_1) & k(\tilde{x}_j,\tilde{\xi}_2) & \cdots & k(\tilde{x}_j,\tilde{\xi}_j) \end{bmatrix} \begin{bmatrix} \tilde{n}_e(\tilde{x}_1) \\ \tilde{n}_e(\tilde{x}_2) \\ \vdots \\ \tilde{n}_e(\tilde{x}_j) \end{bmatrix} - A \begin{bmatrix} \tilde{x}_1 \\ \tilde{x}_2 \\ \vdots \\ \tilde{x}_j \end{bmatrix}$$

An investigation of the elements of the $k(\tilde{x}_i,\tilde{\xi}_i)$ matrix yields the following properties when $k(\tilde{x},\tilde{\xi})$ has the form given in equation (2):

1) $\tilde{\xi} = 0,\ k(\tilde{x},\tilde{\xi}) = 0$ for all $\tilde{x}$

2) $\tilde{x} = 0,\ k(\tilde{x},\tilde{\xi}) > 0$ for all $\tilde{\xi} > 0$

3) $\tilde{x} = \tilde{\xi},\ k(\tilde{x},\tilde{x}) \leq 0$

4) $\tilde{x} \neq 0,\ \tilde{\xi} < \tilde{x},\ k(\tilde{x},\tilde{\xi}) > 0$

$\tilde{x} \neq 0,\ \tilde{\xi} > \tilde{x},\ k(\tilde{x},\tilde{\xi}) > 0$

The first property reduces the system of equations by one by eliminating the first equation. The $k(\tilde{x}_i,\tilde{\xi}_i)$ matrix with the first row and first column deleted has negative diagonal elements which increase in magnitude from the upper left to the lower right. The elements in each row increase positively to the right of the diagonal and decrease to the left of the diagonal. All off diagonal elements are positive.

The reduced non-linear system of algebraic equations may be written:

$$\varphi_2(\tilde{n}_e(\tilde{x}_i)) = \tilde{n}_e(x_2)\, k(\tilde{x}_2,\tilde{\xi}_2) + \cdots + \tilde{n}_e(\tilde{x}_j)\, k(\tilde{x}_2,\tilde{\xi}_j) - A\tilde{x}_2 - \ln \tilde{n}_e(\tilde{x}_2) = 0$$

$$\varphi_3(\tilde{n}_e(\tilde{x}_i)) = \tilde{n}_e(x_2)\, k(\tilde{x}_3,\tilde{\xi}_2) + \cdots + \tilde{n}_e(\tilde{x}_j)\, k(\tilde{x}_3,\tilde{\xi}_j) - A\tilde{x}_3 - \ln \tilde{n}_e(\tilde{x}_3) = 0$$

$$\vdots$$

$$\varphi_j(\tilde{n}_e(\tilde{x}_i)) = \tilde{n}_e(x_2)\, k(\tilde{x}_j,\tilde{\xi}_2) + \cdots + \tilde{n}_e(\tilde{x}_j)\, k(\tilde{x}_j,\tilde{\xi}_j) - A\tilde{x}_j - \ln \tilde{n}_e(\tilde{x}_j) = 0$$

This system of equations may be solved by an iteration scheme. We chose the Newton-Raphson iteration procedure.[36] Let $\tilde{n}_e^{(0)}(\tilde{x}_i)$ be an approximate solution or initial guess at the solution. The Newton-Raphson procedure assumes the next approximation $\tilde{n}_e^{(1)}(\tilde{x}_1)$ is given by

$$\tilde{n}_e^{(1)}(\tilde{x}_i) = \tilde{n}_e^{(0)}(\tilde{x}_i) + h_i$$

where h_i are corrections to $\tilde{n}_e^{(0)}(\tilde{x}_i)$.

Now by Taylor's theorem we have

$$\varphi_i(\tilde{n}_e^{(0)}(\tilde{x}_i) + h_i) = \varphi_i(\tilde{n}_e^{(0)}(\tilde{x}_i) + h_2 \left.\frac{\partial\varphi_i}{\partial\tilde{n}_e(\tilde{x}_2)}\right|_{\tilde{n}_e^{(0)}(\tilde{x}_i)}$$

$$+ h_3 \left.\frac{\partial\varphi_i}{\partial\tilde{n}_e(\tilde{x}_3)}\right|_{\tilde{n}_e^{(0)}(\tilde{x}_i)} + \cdots + h_j \left.\frac{\partial\varphi_i}{\partial n_w(\tilde{x}_j)}\right|_{\tilde{n}_e^{(0)}(\tilde{x}_i)} = 0$$

This expansion yields the following system of algebraic equations for the unknown corrections, h_i:

$$\begin{bmatrix} k(x_2,\xi_2) - \dfrac{1}{n_e^{(0)}(x_2)} & k(x_3,\xi_2) & & k(x_j,\xi_2) \\ k(x_2,\xi_3) & k(x_3,\xi_3) - \dfrac{1}{n_e^{(0)}(x_3)} & \cdots & \\ k(x_2,\xi_4) & & & \vdots \\ \vdots & & & \\ k(x_2,\xi_j) & \cdots & & k(x_j,\xi_j) - \dfrac{1}{n_e^{(0)}(x_j)} \end{bmatrix} \begin{bmatrix} h_2 \\ h_3 \\ h_4 \\ \vdots \\ h_j \end{bmatrix}$$

$$= \begin{bmatrix} -\varphi_2(n_e^{(0)}(x_i)) \\ -\varphi_3(n_e^{(0)}(x_i)) \\ \vdots \\ -\varphi_j(n_e^{(0)}(x_i)) \end{bmatrix}$$

The above equations are linear algebraic equations which may be solved exactly. The Crout version of the Gauss elimination method[36] was employed here. With values for the corrections added to the initial guess, the above linear system is solved again for new corrections. This process is repeated until the corrections are negligibly small.

The initial guess required to start the above method can be obtained in at least two ways. The first is to input a known solution for values of the parameters close to those desired. This is not convenient. The second method involves obtaining a function which generates an initial guess compatible with the iteration scheme. Reference (36) discusses criteria for convergence by iteration. We found that the following expression provided a good starting solution

$$\tilde{n}_e^{(0)}(\tilde{x}_i) = \left| \frac{ci\ \Delta\tilde{x}}{k(\tilde{x}_i, \tilde{x}_i)} \right|$$

where c is an input constant which is made smaller until the first correction are all positive or less than the initial guess.

The above method was coded in Fortran IV Level H language for an IBM 360/67 system. Four decimal place accuracy was obtainable in less than fifteen iterations. With a total of 40 steps in the three integration intervals, fifteen iterations plus extraneous calculations with the resulting solution used approximately 0.4 minutes of IBM 360/67 central processing time.

APPENDIX E

SOLUTION FOR THE GROUNDED-SHOCK-TUBE KERNEL

Consider a grounded cylinder of radius a with a conducting disk located at $x = 0$ as shown in the sketch below. Since the disk

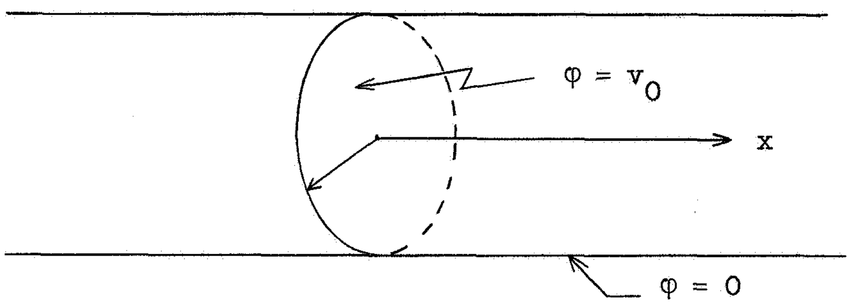

is a conductor it must have uniform potential, say $\varphi = v_0$. The potential distribution inside the cylinder is given in terms of v_0 as follows[37]

$$\varphi(x,r) = \sum_{\ell} \frac{2v_0 \, e^{-k_\ell x} \, J_0(k_\ell r)}{k_\ell a \, J_1(k_\ell a)}$$

where the k's are defined

$$J_0(k_\ell a) = 0 \ .$$

Gauss' law permits us to relate the charge distribution on the disk to v_0. Gauss' law may be written

$$\sigma = \epsilon_0 E$$

or in terms of the potential

$$\sigma = - \epsilon_0 \left.\frac{\partial \varphi}{\partial x}\right|_{x=0} .$$

We find the surface charge density on the disk is given by

$$\sigma(r) = \sum_{\ell} \frac{2v_0 \epsilon_0}{a} \frac{J_0(k_\ell r)}{J_1(k_\ell a)}$$

To find the total charge q we must integrate over the surface of the disk as follows

$$q = \int_0^a 2\pi \sigma r \, dr$$

thus we have

$$q = \frac{4\pi v_0 \epsilon_0}{a} \int_0^a \sum_{\ell} \frac{r J_0(k_\ell r) \, dr}{J_1(k_\ell a)}$$

we find

$$q = 4\pi \epsilon_0 a v_0 \sum_{\ell} \frac{1}{k_\ell a}$$

thus we have

$$v_0 = \frac{q}{4\pi\ \epsilon_0 \sum_{\ell} \frac{1}{k_{\ell} a}}$$

Now we can write the potential inside the cylinder due to charge q on the conducting disk as follows

$$\varphi(r,x) = \sum_{\ell} \frac{q\ e^{-k_{\ell} x}\ J_0(k_{\ell} r)}{2\pi\ \epsilon_0\ a^2\ k_{\ell}\ J_1(k_{\ell} a) \sum_{n} \frac{1}{k_{\ell} a}}$$

Figure 50 shows a plot of intermediate sums for the first few terms of the above solution specialized to the axis of symmetry of the cylinder. This demonstrates that five terms should be retained for a good representation of the solution for $\tilde{x} \geq .25$.

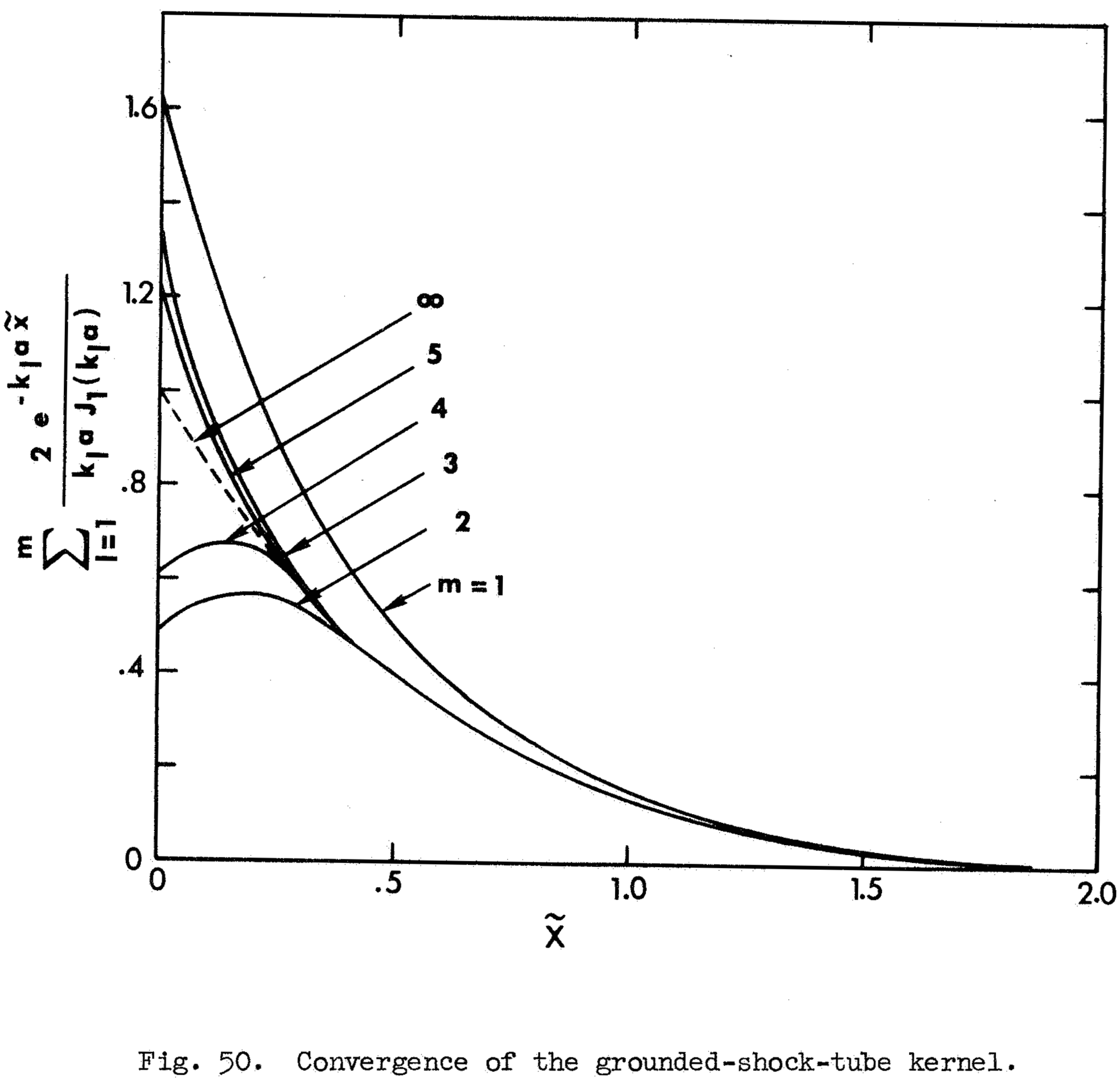

Fig. 50. Convergence of the grounded-shock-tube kernel.